Natural Resources Canada | Ressources naturelles Canada

GEOLOGICAL SURVEY OF CANADA
OPEN FILE 8964

Minimizing the effects of electromagnetic noise and auroral disturbance in the 2017 Kaskattama magnetotelluric data set, Manitoba

I.J. Ferguson, J. McLeod, N. Clark, J.A. Craven, B. Roberts,
T. Hodder, and M. Nicolas

2023

Canada

GEOLOGICAL SURVEY OF CANADA
OPEN FILE 8964

Minimizing the effects of electromagnetic noise and auroral disturbance in the 2017 Kaskattama magnetotelluric data set, Manitoba

I.J. Ferguson[1], J. McLeod[1], N. Clark[1], J.A. Craven[2], B. Roberts[2], T. Hodder[3], and M. Nicolas[3]

[1]Department of Earth Sciences, University of Manitoba, 240 Wallace Building, 125 Dysart Road, Winnipeg, Manitoba
[2]Geological Survey of Canada, 601 Booth Street, Ottawa, Ontario
[3]Manitoba Geological Survey, 360–1395 Ellice Avenue, Winnipeg, Manitoba

2023

Permanent link: https://doi.org/10.4095/331646

This publication is available for free download through GEOSCAN (https://geoscan.nrcan.gc.ca/).

Recommended citation
Ferguson, I.J., McLeod, J., Clark, N., Craven, J.A., Roberts, B., Hodder, T., and Nicolas, M., 2023. Minimizing the effects of electromagnetic noise and auroral disturbance in the 2017 Kaskattama magnetotelluric data set, Manitoba; Geological Survey of Canada, Open File 8964, 1 .zip file. https://doi.org/10.4095/331646

Publications in this series have not been edited; they are released as submitted by the author.

ISSN 2816-7155
ISBN 978-0-660-48048-0
Catalogue No. M183-2/8964E-PDF

Executive summary

The 2017 Kaskattama (KSK) Highland magnetotelluric (MT) dataset was collected in northeastern Manitoba in a quiet geomagnetic period (with geomagnetic disturbance index Kp values of mostly <4), during which only one minor storm occurred. The high geomagnetic latitude of the survey, 65º N, resulted in the recorded MT data containing strong Pc1 micropulsation signals and auroral signals with a potential impact on the quality of MT responses derived from the data. The survey area is within 250 km of hydroelectric facilities in the Gillam area and associated strong sources of electromagnetic noise. Initial computation of MT responses using standard processing methods, such as magnetic field remote-references, yielded MT responses of only moderate quality. Poor long-period responses (periods >30–100 s, frequencies <0.01-0.03 Hz) were attributed to the effects of auroral electrojet signals. This report examines the signals and noise in the KSK MT data, describes the reprocessing of the MT responses, and makes the MT responses publicly-available in Society of Exploration Geophysicist electrical data interchange (EDI) format.

The relatively complicated mix of signal and noise in the KSK dataset was examined using the MT data and geomagnetic recordings from the Geospace Observatory Canada CARISMA stations at Gillam and Churchill, Manitoba and Rabbit Lake, Saskatchewan. Methods used for defining the spatial, temporal, and frequency distribution of the signal and noise included examination of time-series, spectra, and spectrograms; examination of MT responses for different remote-reference recordings including magnetic and electric field recordings; examination of MT responses as a function of recording time; and examination of MT responses for different robust processing parameters.

There were several types of noise identified in the KSK and CARISMA recordings. At Gillam, two main forms of electromagnetic noise were observed:

1. Time-varying broad-band noise present over several time intervals on all three magnetic components.
2. Narrow band noise centred on 4.8 s period (0.21 Hz frequency) and observed most strongly on the magnetic north and vertical (B_x and B_z) components.

The first form of noise was also recorded in the KSK horizontal magnetic field data at locations 240 km away from Gillam. It contributes to significant bias of MT and tipper responses at periods of 0.1–20 s (frequencies of 0.05-10 Hz) calculated using local fields only, and to weaker bias of responses calculated using a magnetic-field remote reference from the Kaskattama area. Spike-like events occurring sporadically in individual magnetic field recordings caused spatially-localized broad-band noise. The spike-like noise did not cause any bias in remote-reference MT responses. Pc1 micropulsation signals did not appear to cause significant bias and the higher signal levels during their occurrence improved the signal to noise ratio.

The MT responses for KSK data set were recomputed using the full length of recording available at each site and with remote-reference electric fields. The reprocessing removed local biases at intermediate periods caused by spatially-corrected magnetic field noise, such as the broad-band noise noted at Gillam, and added at least one-half a decade of improved responses at the longest periods (lowest frequencies).

Table of contents

List of figures

List of tables

1. Introduction

The Kaskattama Highland region is being explored as part of the Geological Survey of Canada's second phase of the Geo-mapping for Energy and Minerals (GEM-2) program's Hudson-Ungava Project (Lavoie et al., 2016, 2017; Nicolas and Armstrong, 2017). A 22 site magnetotelluric (MT) survey, the KSK survey, was conducted in the Kaskattama Highlands in July 2017 (Craven et al., 2017). An 80 km long profile is centred on the Foran Mining Kimberlite No. 1 (KK1) drill-hole and oriented perpendicular to local Paleozoic geological trends (Figure 1). Seven additional MT sites were installed to provide 2-D grid coverage. The survey used Phoenix Geophysics Ltd. MTU instrumentation (Phoenix Geophysics, 2004). This report describes the signals and noise in the KSK MT dataset, describes the reprocessing of the MT responses, and makes the MT responses publicly-available in the Society of Exploration Geophysicist (SEG) Electrical Data Interchange (EDI) format (Wight, 1988).

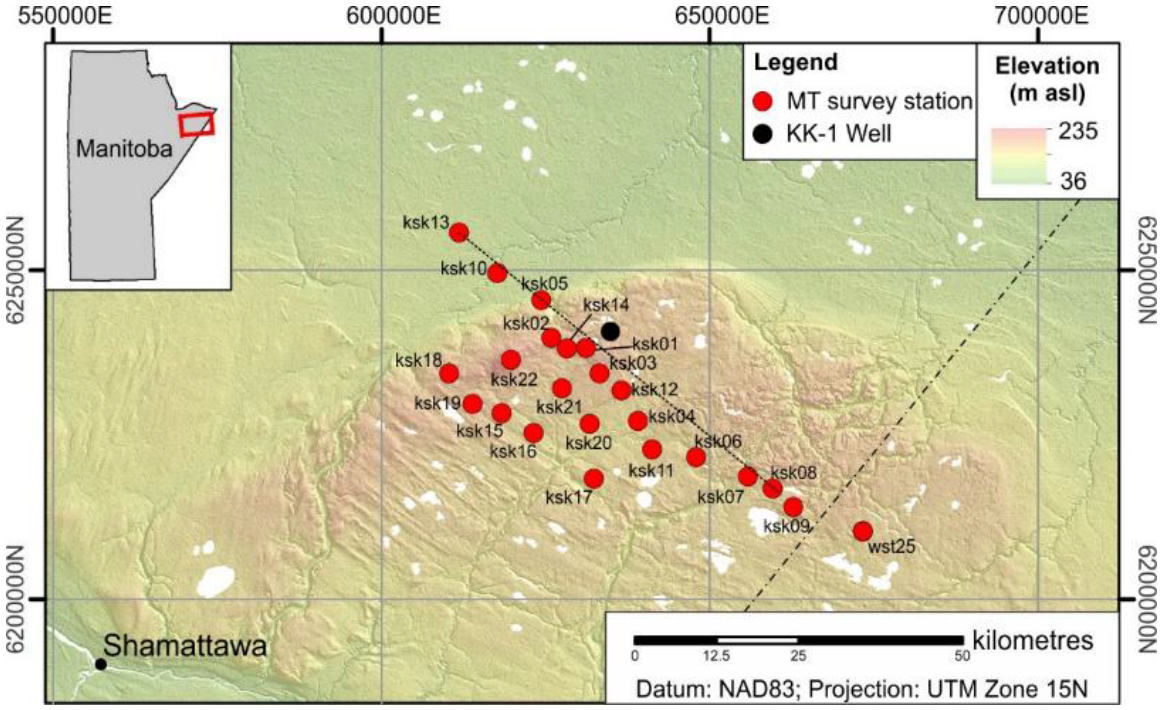

Figure 1. Map of the 2017 Kaskattama MT survey. Black circle shows the location of the KK1 drill-hole and red circles show MT site locations. Site wst25 was acquired in an earlier LITHOPROBE survey (Ferguson et al., 2005).

In MT data processing, time series recordings of the vector components of the horizontal electric field, **E**, and of the magnetic induction, **B** or of the equivalent magnetic field strength **H** (where $\mathbf{B}=\mu_0\mathbf{H}$ and μ_0 is the magnetic permeability of free space) are analyzed in order to provide estimates of the frequency-domain impedance tensor, **Z,** relating the horizontal components of the electric field and horizontal components of the magnetic field and of the tipper transfer function, **T**, relating the vertical component of the magnetic field to the two horizontal components (e.g., Vozoff, 1991; Simpson and Bahr, 2005; Weidelt & Chave, 2012). The transfer functions are defined:

$$\mathbf{E}=\mathbf{Z}\mathbf{H} \quad \text{or} \quad \begin{bmatrix} E_x(\omega) \\ E_y(\omega) \end{bmatrix} = \begin{bmatrix} Z_{xx}(\omega) & Z_{xy}(\omega) \\ Z_{yx}(\omega) & Z_{yy}(\omega) \end{bmatrix} \cdot \begin{bmatrix} H_x(\omega) \\ H_y(\omega) \end{bmatrix} \qquad \text{Eq. 1}$$

and

$$H_z(\omega)=\mathbf{T}^{\mathrm{T}}\mathbf{H} \quad \text{or} \quad H_z(\omega)=\begin{bmatrix} T_{zx}(\omega) & T_{zy}(\omega) \end{bmatrix} \cdot \begin{bmatrix} H_x(\omega) \\ H_y(\omega) \end{bmatrix} \qquad \text{Eq. 2}$$

where ω denotes the angular frequency. As part of their estimation process it is common for instrumental calibrations (e.g., for frequency-dependent responses of the magnetic coil sensors and/or the lengths of

telluric dipoles) to be applied to the frequency-domain quantities and for coordinate system rotations to be applied so the transfer functions correspond to a geographic north-east-vertical-down coordinate system. Uncertainty (e.g., the variance) on the resulting transfer functions is also estimated.

MT transfer function estimation is usually based on the assumption that the magnetic source-fields are spatially uniform (Mareschal, 1986; Vozoff, 1991; Simpson and Bahr, 2005; Weidelt & Chave, 2012). This assumption is usually more accurate for signals associated with higher-elevation magnetospheric current systems than those involving closer lower-elevation ionospheric currents. It is also usually more accurate at middle geomagnetic latitudes, during periods of low to moderate geomagnetic activity, and for more conductive Earth responses (e.g., Mareschal, 1986).

The basic form of MT transfer function estimation, local processing, is a spectral approach using the electric field and magnetic recorded at a single site (Vozoff, 1991; Simpson and Bahr, 2005; Chave, 2012). The magnitude of the resulting impedance estimates may be biased by the presence of noise. The most common local-processing approach provides a least-squares estimate of the impedance assuming that noise is present on only the electric field recordings (herein called *local-B processing*). For the local-B estimate, noise on the magnetic field will bias the magnitude of the impedance estimate downwards. It is possible, although less common, to make an estimate of the impedance assuming the noise is present on the magnetic field (*local-E processing*) (Sims et al., 1971). For the local-E estimate, noise on the electric field will bias the magnitude of the impedance estimate upwards. The local-B and local-E estimates will typically bracket the true value of the impedance magnitude. In the remote-reference approach, recordings from a remote site are used to correct for the effects of the noise at the local site (Gamble et al., 1979a, 1979b). For correct performance of the method, it is necessary for the signal at the remote-reference site to be coherent with the signal at the main MT site, but for the noise to be incoherent. It is most common to use magnetic recordings as the remote-reference (*remote-B processing*) but electric recordings can also be used (*remote-E processing*).

In robust transfer function estimation, methods are applied to address effects of non-stationarity and non-ergodicity of the signal and noise on the impedance and tipper estimates. The robust methods may be relatively simple, for example selection of time segments in which coherence between the electromagnetic components lies within prescribed limits (e.g., Stodt 1983, 1986; Egbert & Livelibrooks 1996) or they may involving weighting of responses estimated from different time segments based on the coherence or variance (e.g., Jones et al., 1983). More advanced methods combine responses from segments in an iterative fashion so as to minimize the variance of the estimates (Jones et al., 1989, Method 6). This approach is incorporated into the Phoenix Geophysics Limited processing code. Alternatively, the responses from segments can be iteratively weighted so that the response conforms to the expected statistical distribution (Egbert & Booker, 1986; Chave et al., 1987; Chave & Thompson, 1989). More recent bounded influence methods minimize the effect of outliers to a greater degree (Chave & Thompson, 2003, 2004; Sutarno, 2005a, 2005b). Robust methods also require more sophisticated methods of error estimation including jack-knife methods (Thomson & Chave, 1991; Chave, 2012). Advanced parametric function-fitting methods are also applied in transfer function estimation (e.g., Larsen, 1989; Larsen et al., 1996). Singular value decomposition of spectral matrices containing all of the MT components recorded at a site also enables the separation of signal from noise, and hence estimation of unbiased impedances (e.g., Park & Chave, 1984) and this approach has been extended to a combined spectral matrix from an array of sites (Egbert & Booker, 1989; Egbert, 2002).

Noise in geomagnetic and MT recordings can be defined as recorded electromagnetic variations that are not due to geomagnetic sources. Numerous studies have investigated source of noise in MT recordings (e.g., Szarka, 1988; Junge, 1996; Ferguson, 2012; and references therein). Noise may be investigated in terms of its temporal variation, spatial variation, polarization and its effect on the transfer functions (e.g., Weckmann, 2005; Escalas et al., 2013).

MT responses for each KSK survey site were initially calculated using standard Phoenix Geophysics Limited processing procedures. Processing of the data from each site was performed each

evening after returning to the survey base in Gillam and the responses were recalculated following the survey (Clark, 2017). The data processing procedures followed the methods outlined by the Phoenix Geophysics Data Processing User Guide (Phoenix Geophysics, 2005). Impedance calculations were based on a robust remote-reference approach (Jones et al., 1989, Method 6) using a remotely recorded magnetic field (remote-B processing). Responses were calculated for subsets of the time series. These responses were then edited on a segment-by-segment and period-by-period basis using the Phoenix **MTEDITOR** before being averaged to yield the final estimates (Phoenix Geophysics, 2005). The editing used an automatic approach to mute responses deviating significantly from mean values as well as a manual approach in which the user turned off selected time-windows.

The initial KSK MT processing produced good quality impedance estimates at periods of less than 10 to 30 s. In the period range <1 s, the response editing was straightforward and included the muting of time-windows with impedance estimates affected by helicopter arrivals or departures. In the period range of 1 to 30 s, it was necessary to mute a larger number of time windows from either the local day or night time but there were sufficient consistent impedance estimates to allow this editing to be done objectively. At longer periods it was necessary to delete a large proportion of the time windows to obtain reasonable impedance estimates. The approach was more subjective and the resulting averaged impedance estimates were considerably noisier than at shorter periods. At periods longer than 300 s, it was impossible to produce reasonable impedance estimates. Figure 2 shows examples of edited responses. The main limitation on the long-period responses was interpreted to be non-uniform geomagnetic sources occurring at the auroral latitude of the survey, rather than artificial electromagnetic noise.

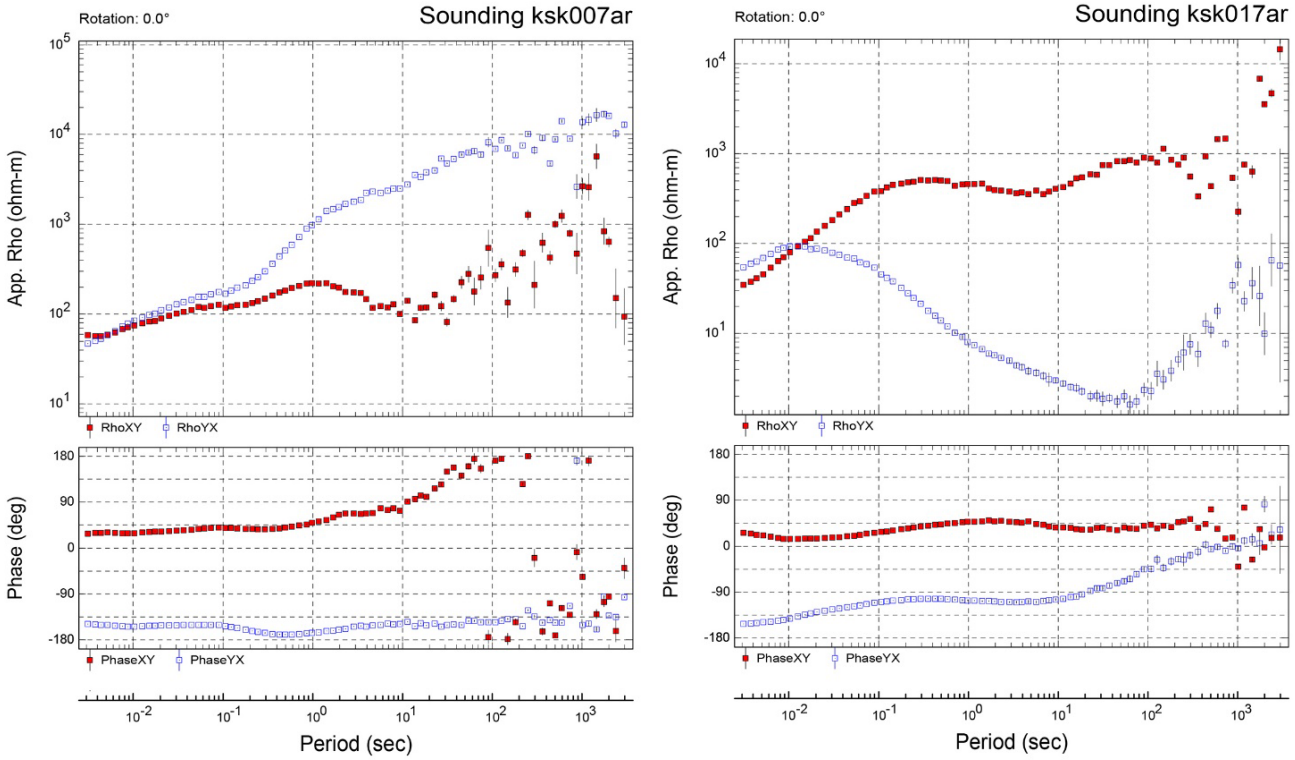

Figure 2. Examples of the B-remote MT response at ksk07 and ksk17 following initial processing. Increased noise levels are evident at periods longer than 10 s at ksk07 and longer than 30 s at ksk17.

There was also evidence for electromagnetic noise affecting the MT responses in the survey. Several coil calibrations conducted on the first day of the survey, July 7th, at site ksk01 produced unsatisfactory results and the magnetic recordings made during the following night at site ksk02 were also very noisy. The calibration issues were attributed to electromagnetic noise from distant

hydroelectric operations and the noisy recordings to physical movement of magnetic sensor coils installed in swampy settings.

The objective of the research described in this report is to:

1) Investigate the sources of signals and noise in the recorded MT data to better understand the limitations on the impedance estimates.
2) Reprocess the raw MT data to improve the impedance estimates, particularly at periods >30 s. This analysis is restricted to reprocessing options available in the Phoenix software **SSMT** and **MTEDITOR**.
3) Make the final MT responses publicly-available in edi format in an electronic appendix to the report.

A component of the calculations described in this report was done by J. McLeod and I.J. Ferguson after initial MT processing by N. Clark (Clark, 2017). Funding support for this work came from the GEM 2 project through a contract between Natural Resources Canada and the University of Manitoba.

2. Survey Overview

This section describes the configuration of the Kaskattama MT survey and the methods used for the initial data processing.

2.1 Recording configuration

The Kaskattama MT data were recorded at each site using two horizontal Phoenix Geophysical MTC-50 magnetic sensor coils, a single vertical AMTC-30 magnetic sensor coil, four non-polarizing electrodes, and an MTU data acquisition unit (Phoenix Geophysics, 2004). At ksk01 additional recordings were made with AMTC-30 horizontal coils. Each MTU data acquisition unit was calibrated in the town of Gillam, Manitoba before the survey and the sensor coils were calibrated at several sites in the survey location (Clark, 2017). The north, east and vertically downwards magnetic components are referred to as B_x, B_y, and B_z. The north and east electric field components are denoted E_x and E_y.

The main recordings were made over a single night at each site (the "a" run). At some sites a second night of recordings was made (the "b" run). At ksk01, AMT data was collected on a third night of recording (the "c" run). Most of the data were acquired using the Phoenix Geophysics MT acquisition setting where continuous records are made using a 15 Hz sampling interval (Band 5) and shorter discontinuous records are made using a 150 Hz (Band 4) and a 2400 Hz sampling frequency (Band 3) (Phoenix Geophysics, 2004). The electric field coupling was set to DC, the electric field gain was set to high, and the VLF filter was set to weak. Most sites were programmed to start recording at 20:00 UT (15:00 CDST) and finish recording at 14:00 UT (09:00 CDST) for both the continuous and discontinuous acquisition bands yielding 18 hours of MT recordings.

The data acquisition parameters produced time series files corresponding to each recording band. The files are named with the first four digits corresponding to the MTU serial number, the next digit is the month in octal format, the next two digits are the date the recording started, and the final digit is the run (e.g., **1561711A.TS3**). The typical volume of data recorded for each site for each run was between 200 and 400 Mb.

2.2 Processing of MT data collected with Phoenix Geophysics instrumentation

The first stage of KSK MT data processing involved entering site details and defining the processing mode for each site (local, local electric field with imported magnetic field data, or remote-reference). The Phoenix Geophysics **SSMT2000** program was used to update declination, electrode spacing, and magnetic coil identification information in the table file for each site and to correct for site layout errors at ksk19 (Phoenix Geophysics, 2005). At all sites except for ksk08, and the AMT run at ksk01, remote-reference processing with a remote magnetic field was adopted. The optimal site for the

remote reference was chosen during the initial in-field processing from the set of other sites recording during the same day as the main site. For ksk02 and ksk19, which had poor or incorrect magnetic field recordings, the magnetic field recordings from another site over the same time frame were imported and used to represent the local magnetic field. Following the specification in **SSMT** of the electric field, the local magnetic field, and the remote-reference magnetic field, the location of the corresponding calibration files, and the time interval for the analysis, the time series were Fourier-transformed using an output data format of four frequencies per octave. The **SSMT** program provided output files for a number of frequency ranges with the corresponding file extensions: **fc3–fc7**.

The second stage of processing involves the robust combination of Fourier transform data to yield impedance estimates in individual time windows (defaulting to 20 equal length segments for each run) from the time series (Phoenix Geophysics, 2005). The basic robust processing parameters control the weighting of the auto and crosspowers used to form the initial impedance estimates. This weighting may be based on coherence (a selection from various multiple and partial coherence combinations between field components at the local and remote site) and/or apparent resistivity variance (Jones et al., 1989). The calculations used a minimum level of coherency and variance, which when reached, causes the processing to cease for that frequency. The user can also place a limit on the maximum fraction of estimates that may be rejected based on the coherence criterion or the variance criterion. The final robust processing parameters define how the results from the initial estimates are weighted in order to form the final averaged estimates. This weighting may again be on coherence, which gives more weighting to results with higher levels of ordinary coherence between electric and magnetic fields, or on apparent resistivity variance, which gives more weighting to estimates with smaller error bars (Phoenix Geophysics, 2005). The robust processing creates files containing the high and low frequency range MT responses with file extensions **MTH** and **MTL** respectively.

In-field processing of the Kaskattama data used the default values for all of the processing parameters which are:

1. Initial weighting based on both coherence and rho variance.
2. Coherence type=7: Combines multiple coherency of B_x with the total remote magnetic field and multiple coherence of B_y with the total remote magnetic field: $\gamma^2(B_x:R_x,R_y)\gamma^2(B_y:R_x,R_y)$.
3. Minimum coherence level is 0.85 and up to 35% of estimates can be rejected on the basis of coherence.
4. Minimum rho variance is 0.75 and up to 25% of estimates can be rejected on the basis of rho variance.
5. Final values are obtained used rho variance weighting.

The final stage of the Phoenix MT data processing involves manual and/or automated editing of the estimates from the individual time segments using the **MTEDITOR**. The input files are the **MTH** and **MTL** files from individual or multiple runs. The output files include an mpk file that records the muting of particular time segments for particular periods, and subsequently an MT edi file. The in-field processing of the Kaskattama data used an initial **AutoEdit** followed by manual editing (as discussed in Section 1). The manual editing focused primarily on the impedance phase response but also incorporated the remote reference apparent resistivity response as a secondary parameter.

The Kaskattama edi files were imported into either the **WinGLink** MT software platforms for further inspection and processing. After the initial import, additional editing of the apparent resistivity and phase responses was completed.

3. Source fields and auroral signals

This section describes the geomagnetic setting of the Kaskattama survey and background information on methods and indices used to characterize the geomagnetic data. It also provides a brief review of geomagnetic signals in auroral zones and their impact on magnetotelluric responses.

3.1 Geomagnetic setting of Kaskattama survey

The geographic location of the reference point on the main KSK MT profile is 56.27° N, 90.88° W. Corresponding geomagnetic coordinates were calculated using the interactive program at World Data Center for Geomagnetism, Kyoto (http://wdc.kugi.kyoto-u.ac.jp/index.html, accessed December 2017). For 2017, the geomagnetic coordinates are: 65.04º N, 24.17º W. This location places the MT survey in the northern auroral zone, which extends over geomagnetic latitude range 63º–77º N (http://www.spaceweather.gc.ca/info-gen/glossa-en.php, accessed December 2017). Individual magnetic field components for the reference point are shown in Table 1. Values were calculated using the program at the GSC Geomagnetic Laboratory web page (http://geomag.nrcan.gc.ca/calc/mfcal-en.php, accessed December 2017) for 07 July 2017 (using the IGRF 2015 model).

Table 1. Geomagnetic field components for Kaskattama Highland area (56.27º N, 90.88º W) for July 2017

D (º)	I (º)	*H* (nT)	B_z (nT)	*F* (nT)	B_X (nT)	B_Y (nT)
-4.678	79.060	11,058	57,209	58,268	11,021	-902

3.2 Reference information

In the examination of signals recorded during the KSK survey we compare MT observations with geomagnetic recordings at nearby magnetic observatories. We use of three stations from the Canadian CARISMA (Canadian Array for Realtime Investigations of Magnetic Activity array (e.g., Mann et al., 2008) (Figure 3):

- Gillam (GILL) 66.03º N, 26.95º W (geomagnetic)
- Churchill (FCHU), 68.32º N, 26.46º W (geomagnetic)
- Rabbit Lake (RABB) 66.85º N, 40.89º W (geomagnetic)

(http://www.carisma.ca/station-information, accessed December 2017). Each CARISMA site has multi-component geomagnetic data sampled at 1 s intervals available for most of the duration of the KSK MT survey. We also make use of 1-minute sampled data from the Geomagnetism Canada observatory at Churchill (FCC). In addition, we make use of several derived geomagnetic products.

1. *Kp indices*. The Kp index is a pseudo-logarithmic measure of the level of the global geomagnetic disturbance over 3 hour intervals. It is based on recordings from 13 global observatories, which lie between 46º and 63º north and south geomagnetic latitude. Data were obtained from NOAA Space Weather (www.ngdc.noaa.gov/stp/GEOMAG/kp_ap.html, accessed December 2017) and were in turn taken from the GFZ German Research Centre for Geosciences (www.gfz-potsdam.de/en/kp-index, accessed December 2017).
2. *Auroral indices*. The Auroral Electrojet Index, AE, is designed to provide a global, quantitative measure of auroral zone magnetic activity produced by enhanced ionospheric currents flowing below and within the auroral oval (Davis & Sugiura, 1965; Parkinson, 1983; Nakamura et al., 2015). It is obtained from a number (usually greater than 10) of stations distributed in local time in the latitude region typical of the northern hemisphere auroral zone. The data from these stations are collated and the lower bound or maximum negative excursion (referenced to a level determined for each observatory from quiet intervals) is called the AL index and the upper bound of maximum positive excursion is called the AH index. AU and AL thus represent the upper and lower envelopes of the superposed plots of all data from these stations as functions of universal time (UT) (Davis & Sugiura, 1965; Nakamura et al., 2015). The two indices are interpreted as defining the maximum strength of eastward and westward electrojet currents in the auroral latitude ionosphere, respectively The AE index is the difference between the corresponding AH and AL values and provides a measure of the overall horizontal current strength. It represents the sum of the maximum current strength of the two oppositely directed currents at two different points in local time (Nakamura et

al., 2015). In this study, we use corresponding Canadian auroral indices CL, CU and CE calculated using the CARSIMA sites indicated in Figure 3. The data were taken from the CARISMA web site www.carisma.ca/carisma-data/fgm-auroral-indices. The indices are calculated for only the 00:00 to 12:00 UT period corresponding to 19:00 to 07:00 CDST time zone in northeastern Manitoba.

3. *Spectrograms*. The time-frequency variations of geomagnetic signals can be displayed as spectrograms. Here we use spectrograms for CARISMA sites covering the Pc1 range (0.01–2 Hz) available at www.carisma.ca/carisma-data/fgm-pc1-power-spectra and the Pc5 range (0.001–0.01 Hz) available at www.carisma.ca/carisma-data/fgm-pc5-power-spectra.

Figure 3. Observatories included within CARISMA (www.carisma.ca/carisma-data/fgm-auroral-indices, accessed January 2018). Red star shows location of the KSK MT survey. Sites with dark blue symbols are used to calculate auroral indices, and those with light blue symbols are used to calculate polar indices. The Gillam station is denoted GILL, the Churchill station FCHU, and the Fort Simpson Station FSIM.

3.3 Geomagnetic signals in the auroral zone

Geomagnetic signals in the auroral zone can differ from those at lower and higher geomagnetic latitude. The signals are typically stronger than at lower latitude and less spatially uniform. Figure 4 displays the typical variation of geomagnetic signals with latitude. Note the very strong summer-time maximum at geomagnetic latitude 65º N, the latitude of the Kaskattama MT survey.

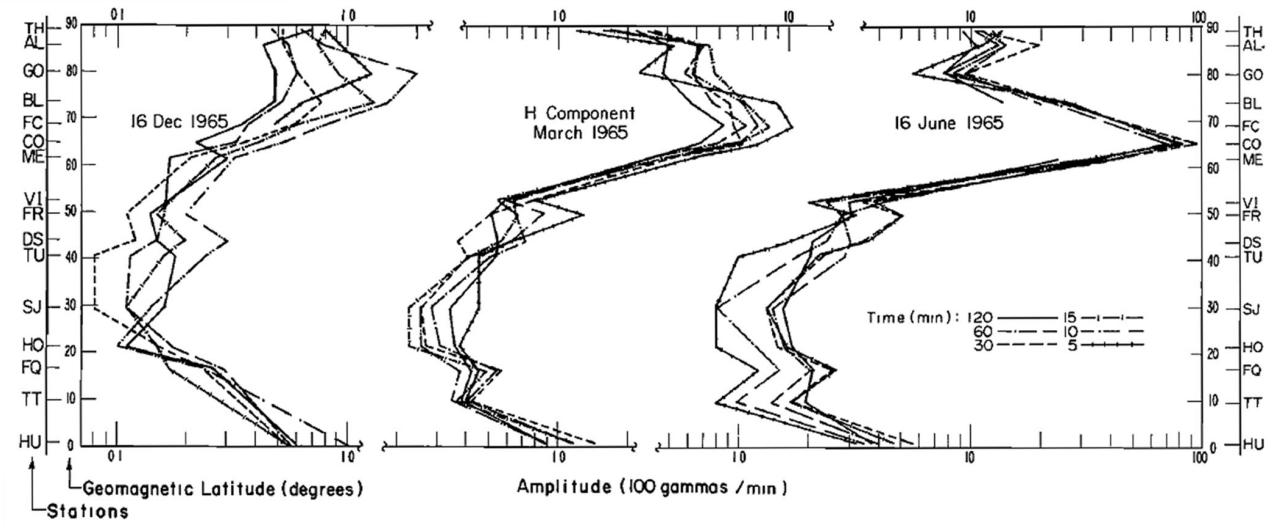

Figure 4. Spectral amplitude versus latitude for 5, 10, 15, 30, 60 and 120 minute periods for three days in 1965 (Campbell, 1976). The 16th June was a geomagnetically active summer day. The amplitude scale is 100 times the amplitude in nT divided by the period in minutes. The two letter codes indicate the magnetic observatory providing data. Note the auroral and equatorial enhancement.

3.3.1 Micropulsations Micropulsations are interpreted to be caused by magnetospheric hydrodynamic (Alfven) waves produced when one magnetospheric plasma streams over another (Campbell, 2003). They can be pictured as resonances of geomagnetic lines of force (Parkinson, 1983; McPherron, 2005). The signals are filtered by their passage through the ionosphere, with a short period cut-off that depends on the ion density and creates additional latitudinal dependence on the response (Parkinson, 1983). Micropulsations are divided into groups based on their period and regularity (e.g., Figure 5) and associated signals have some geomagnetic latitudinal dependencies:

- At high latitudes Pc1 pulsations (including pearls) tend to occur in the afternoon and are of order 0.1 nT in amplitude and in the period range 3–8 s. They are sometimes absent for intervals of more than a week.
- Pc2–Pc4 pulsations have higher amplitudes at auroral latitudes from 0.1 nT for Pc2 to 5 nT for Pc4. These pulsations have similar properties but pulsations with periods less than 18 s are rare in daylight hours and those with periods of 18 – 40 s are rare at night. The period decreases with increasing disturbance levels so Pc4 typically occurs for Kp of 0–1, Pc3 at Kp of 2–3, and Pc2 during disturbed periods.
- Pc5 pulsations are predominantly high latitude pulsations with a sharp maximum of amplitude near the auroral zone Parkinson (1983). Amplitudes of 100 nT are common near the auroral zone.
- The amplitude of Pi2 has a maximum at 65º N (Parkinson, 1983, Mareschal, 1986). The period again decreases with increasing disturbance level. Pi2 pulsations will often accompany the onset of a polar magnetic substorm.
- Ps6 pulsations have a period of 600 to 2400 s are ultra-low frequency pulsations associated with the modulation of the auroral electrojet. They tend to occur at high latitude at post-midnight local time during the recovery phase of substorms and affect mainly the east component of the magnetic field (McPherron, 2005).

The source region for pulsations may be relatively localized (e.g., Mareschal, 1986). The decrease in the quality of the initial Kaskattama MT responses at long periods corresponds to the period range of Pc4, Pc5, Pi2, and Ps6 pulsations.

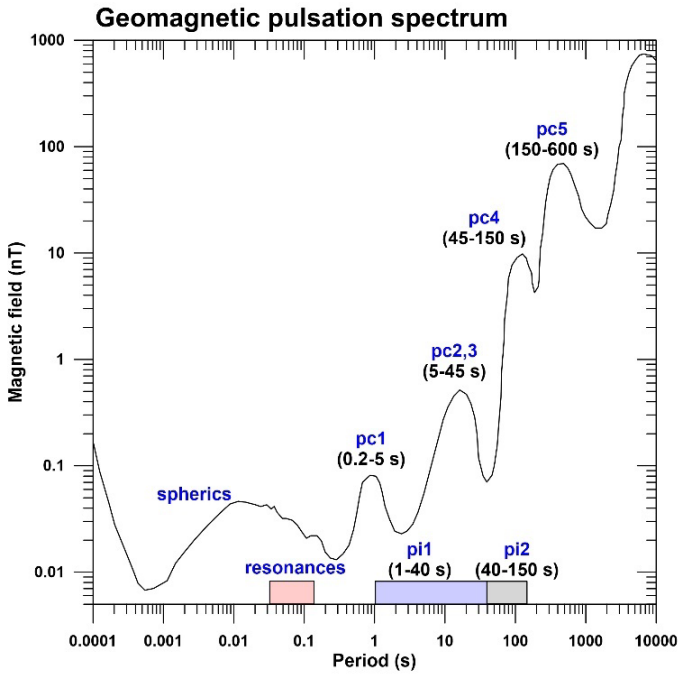

Figure 5. Period ranges of pulsation types (modified from Campbell, 2003).

3.3.2 Polar magnetic substorms Longer period signals in the auroral zone arise through the coupling of ionospheric and magnetospheric currents in the auroral electrojet and field-aligned current system (Figure 6). Corresponding disturbances are referred to as polar magnetic substorms. The auroral electrojet is a complex, low altitude (100–120 km) ionospheric current system whose position is strongly time dependent, depending on local time of day (Figure 7). During daylight hours the electrojet weakens and is located at higher geomagnetic latitudes whereas at night it strengthens and moves south to 65º N or beyond (Kamide, 1982; Garcia et al., 1997). The electrojet flows in an eastward direction in the earlier part of the night (with field-aligned currents flowing into the ionosphere south of field-aligned currents flowing out). This pattern reverses after midnight. The most complex ionospheric current systems occur just prior to midnight during the collision of the evening eastward electrojet and the early morning westward electrojet (Garcia et al., 1997). This location is known as the Harang discontinuity.

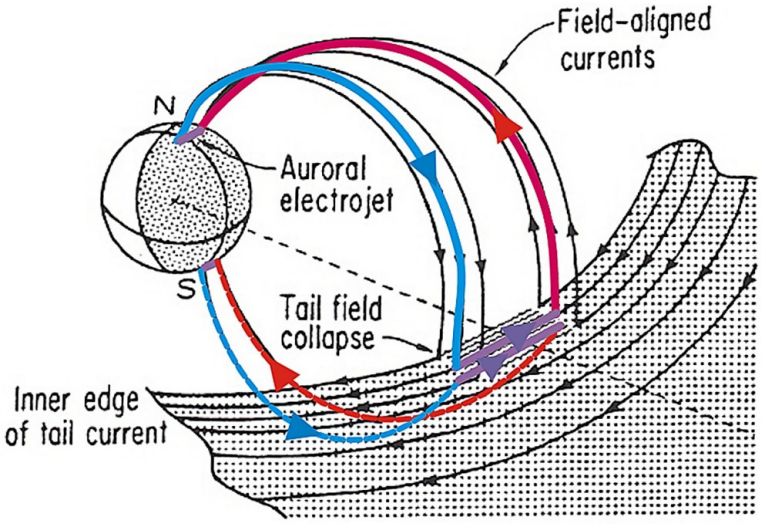

Figure 6. Simplified model of polar magnetic substorm (Ritter and Lühr, 1982). Magnetospheric current systems are coupled to the ionospheric auroral electrojet through field-aligned currents.

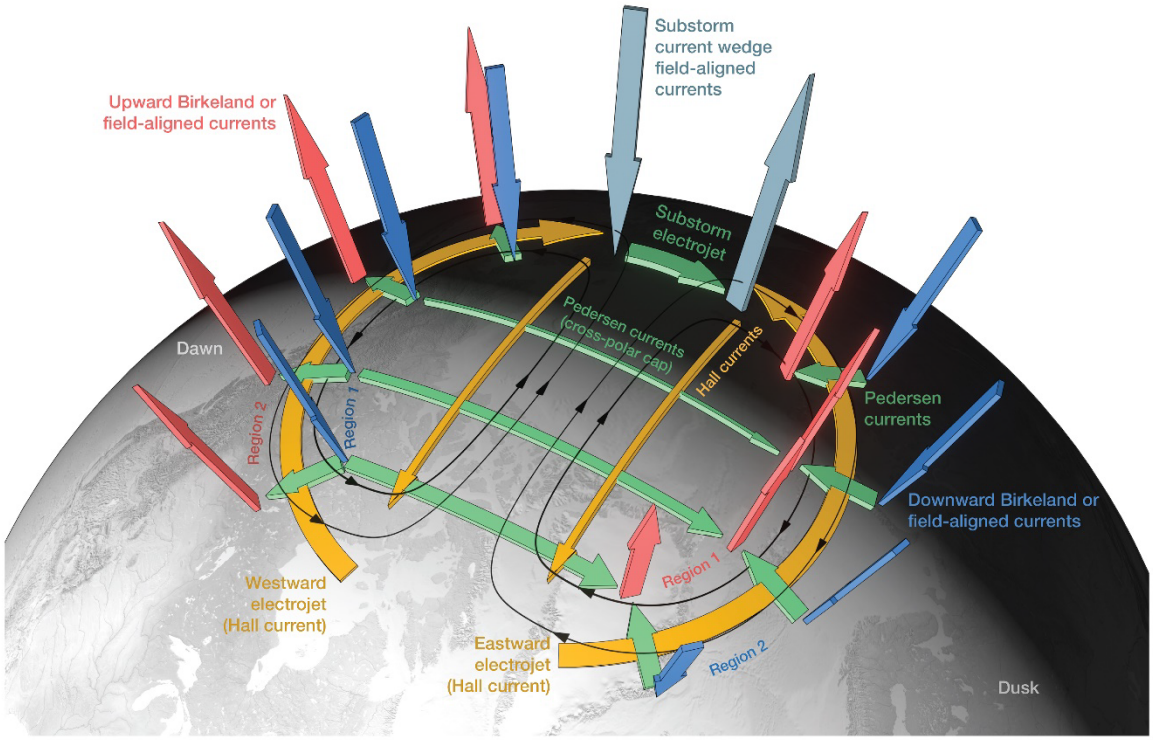

Figure 7. Ionospheric current system (Palmroth et al., 2021). Arrows indicate direction of current flow and the current between adjacent contour lines is 104 kA.

Because of its low altitude, the auroral electrojet produces short-wavelength, non-plane-wave source fields that affect the MT method which assume a plane-wave source. The localized nature of the source is indicated by the presence of a significant vertical component in ground magnetic field recordings (e.g., Mareschal, 1986; Boteler and Pirjola, 1998; Figure 8). During the day normal processes in the magnetosphere dominate the geomagnetic field (Garcia et al., 1997) so smaller vertical fields are expected.

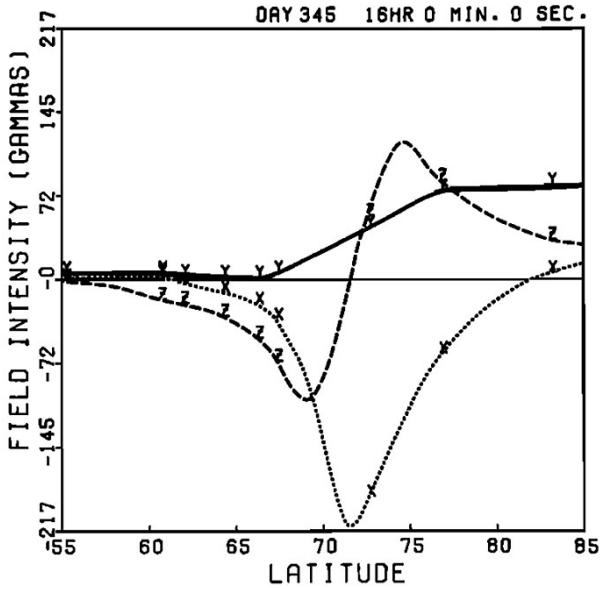

Figure 8. Spatial variation of hourly averaged ground magnetic field recordings near local dawn (Hughes and Rostoker, 1977). Note the strong vertical magnetic field component. The negative north (X) response is indicative of the west flowing electrojet at this time.

3.3.3 Magnetic storms A magnetic storm is an event of several days' duration during which there is a large decrease in the horizontal component of the geomagnetic field at the Earth's surface due to an enhancement of the ring current (McPherron, 2005). There are no pulsations specifically tied to the ring current. A magnetic storm will typically produce stronger signals at auroral latitudes. It may involve some feeding of the field-aligned current system and creation of ionospheric currents (Campbell, 2003). The ionospheric disturbances may also be associated with aurora.

3.4 Auroral signals in MT responses

3.4.1 Effects of source-fields on the MT response The low altitude and localized ionospheric current systems occurring during magnetic polar substorms, and at some times during magnetic storms, create magnetic fields that violate the plane-wave assumption on which most MT studies are based, causing biasing of impedance estimates (e.g., Jones, 1980; Mareschal, 1986; Lezeata et al., 2007). Typically, the responses affected by these signals will exhibit an underestimated apparent resistivity (impedance magnitude), and an overestimated impedance phase (Jones, 1980; Mareschal, 1986; Garcia et al. 1997, and references therein). In addition, the strong vertical magnetic field associated with these current systems will bias the vertical magnetic field transfer functions leading to directional and phase bias in the tipper and indication arrow responses.

The consequences of the short wavelength components will depend on the relative size of the term k^2, where k is the measure of the spatial frequency of the signal, and the term $\omega\mu_0\sigma$, where σ is the effective conductivity. The effects of the non-spatially uniform sources will therefore increase with increasing period (decreasing ω) and will become more significant in more resistive environments (decreasing σ).

3.4.2 Mitigation of the effects of auroral signals There are several approaches that have been considered for removal or minimization of the effects of non-uniform auroral signals in MT processing.

1. Robust spectral processing Robust spectral processing based on one or more of several different approaches can reduce the effects of auroral signals (Jones et al., 1989; Garcia et al., 1997). Coherence thresholding will reduce the effects of noisy segments of the data. It is most applicable to electric field noise and will have less affect when the biasing of responses is caused by anomalous magnetic field values or correlated signals on multiple electric field and magnetic field components. Iterative re-weighting of the least squares solution from small time windows will downweight segments in which the response deviates statistically from the distribution of responses expected for Gaussian data. Finally, there are methods for controlling the leverage of the response caused by anomalous magnetic field values. Garcia et al. (1997) show that robust procedures require a reasonably low ratio of contaminated/uncontaminated data (typically 40–50% or less) to yield reliable results but can still be useful in worse cases.
2. Basic spectral processing At a more basic level, it is possible exclude particular time-windows in the time series from the computation of the impedance responses. For example, the processing may be based on only local day time data (06:00–18:00) with exclusion of local nighttime (18:00–06:00) responses. This approach can be combined with robust spectral processing. However, Garcia et al. (1997) show that MT responses estimated from late afternoon (15:00–18:00) and early morning (06:00–09:00) recordings may also be affected by auroral signals to a varying degree.
3. Windowing by magnetic field index or vertical magnetic field Windowing of the data set can also be done using other criteria. One approach is to choose data segments at times of lower values of global or auroral magnetic index. Jones and Spratt (2002) show that a method based on exclusion of periods with high levels of vertical magnetic fields can lead to a significant improvement in the responses. In their study, the authors excluded data for which the vertical magnetic field lay more than two standard deviations from the mean of the distribution. This method will be less applicable

in strongly 2-D and 3-D resistivity environments in which there is a strong vertical magnetic field produced by inductive processes.

4. Full spatio-spectral approaches Finally, if the survey involves the operation of many stations at one time it is possible to apply array techniques in which the effective structure of the source is resolved along with the geomagnetic responses (e.g., Egbert, 2002).

4. Geomagnetic signals during Kaskattama MT survey

This section provides an examination of the geomagnetic signals that occurred during the KSK MT survey in terms of their time-domain and frequency-domain form and also the time-frequency variations.

4.1 Magnetic activity levels

The magnetic field variations during the KSK survey are shown in Figure 9. The signals are dominated by polar magnetic substorms. A minor magnetic storm (Kp<5.3) occurred on July 9–11 UT with this classification of activity level being based on the Kp index (https://www.spaceweatherlive.com/en/help/the-kp-index). The storm occurred during the recordings made at ksk01–ksk07. During the initial and main phase of the storm, magnetic field variations ranged over about 500 nT. Outside the period of the storm the magnetic field was quiet (Kp<2). A moderate magnetic storm (Kp<6) occurred just after the end of the survey.

The auroral indices (Figure 9) clearly show the occurrence of both eastward and westward electrojets on most days during the survey. The eastward electrojet is indicated by the positive CU indices typically occurring over the local evening period 00:00–06:00 UT (19:00–01:00 CDST) and the westward electrojet is indicated by the negative CL indices typically occurring over the local morning period 0800–1200 UT (03:00–07:00 CDST). On the quiet magnetic days, the CE index was typically <200 nT with CU magnitudes less than 150 nT and CL magnitudes less than 250 nT. The pattern of auroral electrojet activity was amplified strongly during the magnetic storm indicating the occurrence of significant ionospheric current flow. At this time the CE index reached a value of 1200 nT, the magnitude of CU index reached a value of nearly 500 nT and the magnitude of the CL index reaches a value of nearly 1000 nT.

The results in Figure 9 point to strong ionospheric current activity dominating the magnetic field variations during the KSK MT survey. At quiet times, the polar magnetic substorms dominate the signal and during the magnetic storm on July 9–11th the auroral indices and strong vertical magnetic field responses suggest the occurrence of localized current systems. The Canadian auroral indices show stronger effects in the CL index than the CH index suggesting that there may be stronger ionospheric currents associated with the westward electrojet.

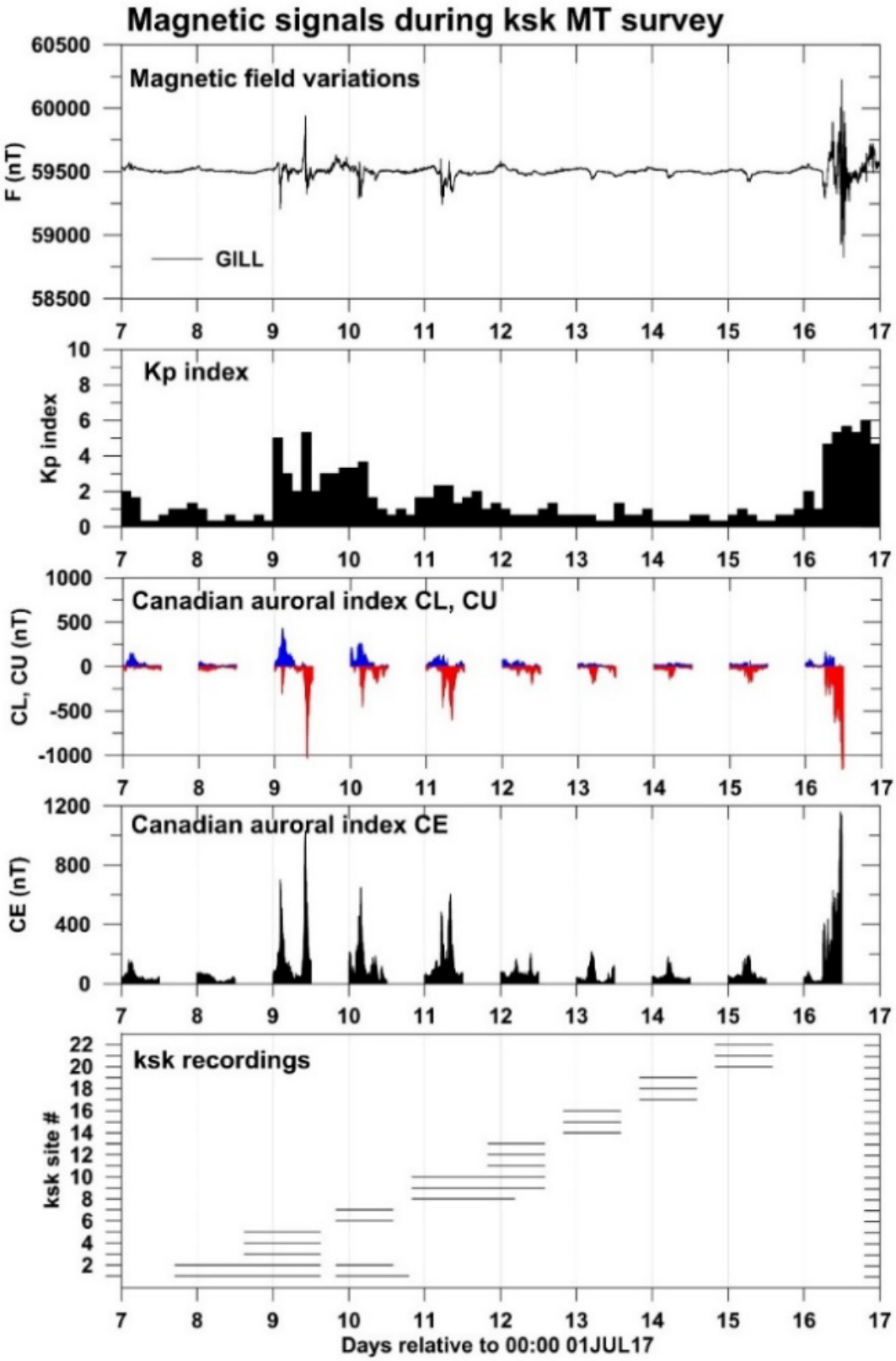

Figure 9. Measures of the magnetic field activity during the KSK survey. Upper panel shows the total field variations at CARISMA station GILL. Second panel shows the preliminary global Kp index. Third and fourth panels show the Canadian auroral indices from CARISMA sites. Final panel shows the duration of recording at each KSK site.

4.2 Geomagnetic signals at different time-scales

Figure 10 shows the magnetic field time series for individual field components during the KSK survey. The polar magnetic substorm and magnetic storm activity can be seen in both the horizontal and vertical components of the magnetic field variations as well as in the total field variations. The magnetic time-series at Gillam (240 km geographically west of the KSK survey area), Churchill (340 km geographically northwest of the KSK survey area) and Rabbit Lake (800 km WNW of the KSK survey area) are similar, but close inspection reveals significant differences. For example, on both horizontal magnetic field components, negative excursions associated with the westward electrojet are more prominent in the FCHU time series than the GILL and RABB time series. As the horizontal field components are only weakly affected by internal electromagnetic induction effects, these differences can be attributed to variations in the source field between the locations. The vertical magnetic field component also exhibits differences between the sites. For example, the sharp positive excursion on 09JUL17 is larger in the GILL and RABB data than at FCHU and there are differences in the form of the magnetic substorm (auroral electrojet) signals on 15JUL17. These differences may be due to both source-field effects and inductive effects associated with lateral variations in Earth resistivity at the two sites. However, the similarity of the GILL and RABB responses for sites at a similar geomagnetic latitude (66.03º N and 66.85º N) versus the different fields at FCHU (68.32º N) suggests the differences are due mainly to source effects. Spatial differences between the horizontal and vertical magnetic field at the three sites, and particularly those in the much larger vertical component, are mapped into differences in the total magnetic field variations.

Figure 11 shows the magnetic variations for 09JUL17 at an expanded time-scale. There are strong spatial differences in the substorm signals at 02:00–04:00 UT in the horizontal components of the field in both the north-south (GILL to FCHU) and east-west directions (RABB to GILL). Variations in the east-west direction are more complex than explained by the shift in local time (9.04º of geographic longitude or 0.6 hours) indicating spatio-temporal variations in the ionospheric current system. The vertical magnetic field has a more spatially-consistent form, but significant differences between the responses at the three sites can be observed. The storm commencement that occurs soon after 1000 UT has a similar form and magnitude in the B_x component at all three sites. This relatively uniform response can be attributed to the larger-scale effects of the ring current reducing the north component of the field. The B_y and B_z components show significant latitudinal and longitudinal differences over the same period suggesting the presence of significant ionospheric signals.

Figure 12 shows higher frequency signals occurring during the interval 11:00–12:00 UT 09JUL17 at GILL, FCHU and RABB. Intermediate period signals visible on the time-series, with a period of approximately 10 minutes or 600 s, are interpreted to be Pc5 pulsations. These signals are quite similar in the B_x component at the three sites, but exhibit large spatial variations in the B_y and B_z components. These non-uniform signals will have a biasing effect on the estimation of the MT impedance and tipper response.

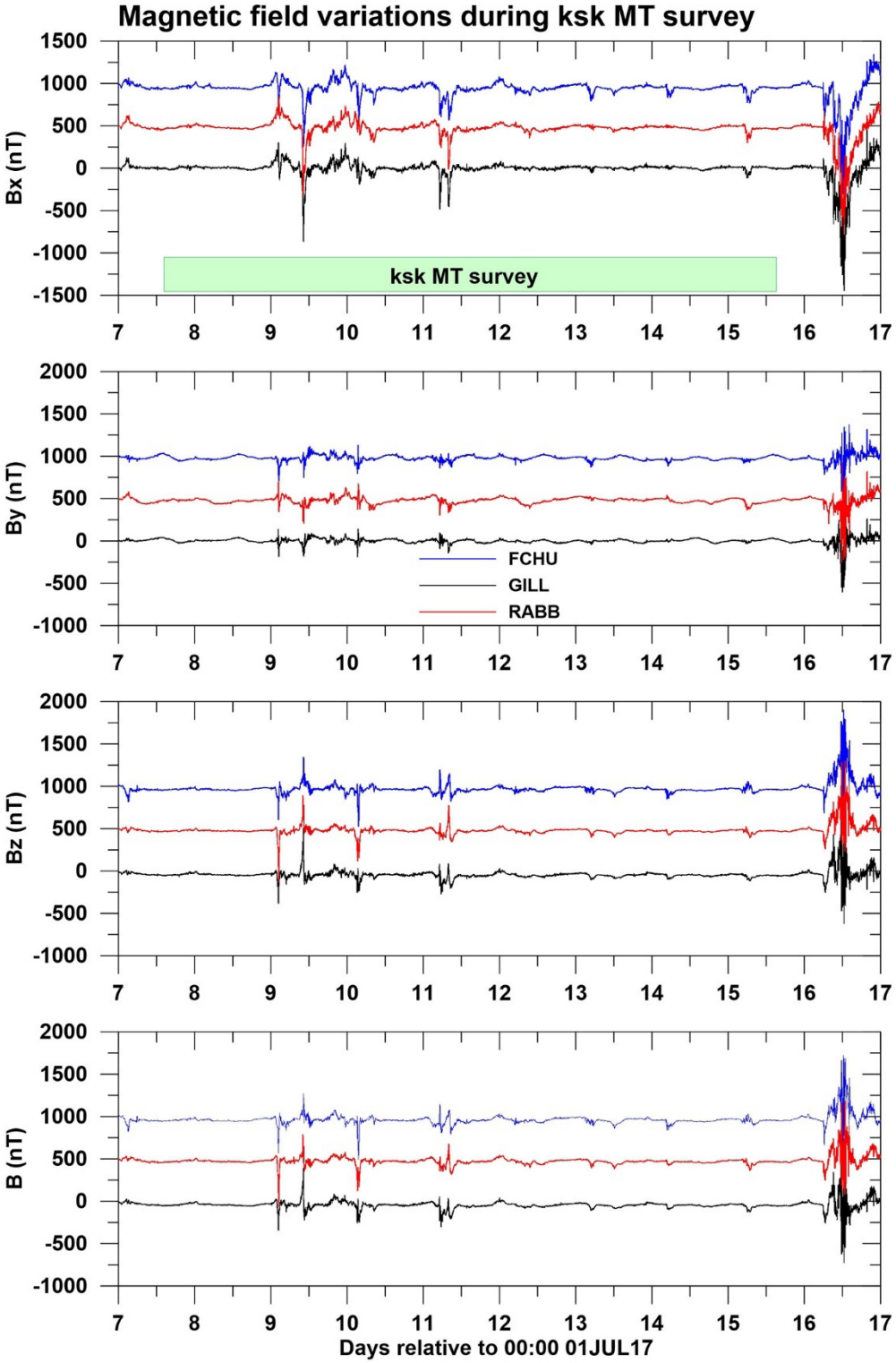

Figure 10. Magnetic field component variations over the duration of the Kaskattama MT recordings for CARISMA sites GILL, RABB, and FCHU. To enhance clarity, a baseline value has been removed from each component and the RABB and FCHU data have been offset by 500 nT and 1000 nT respectively.

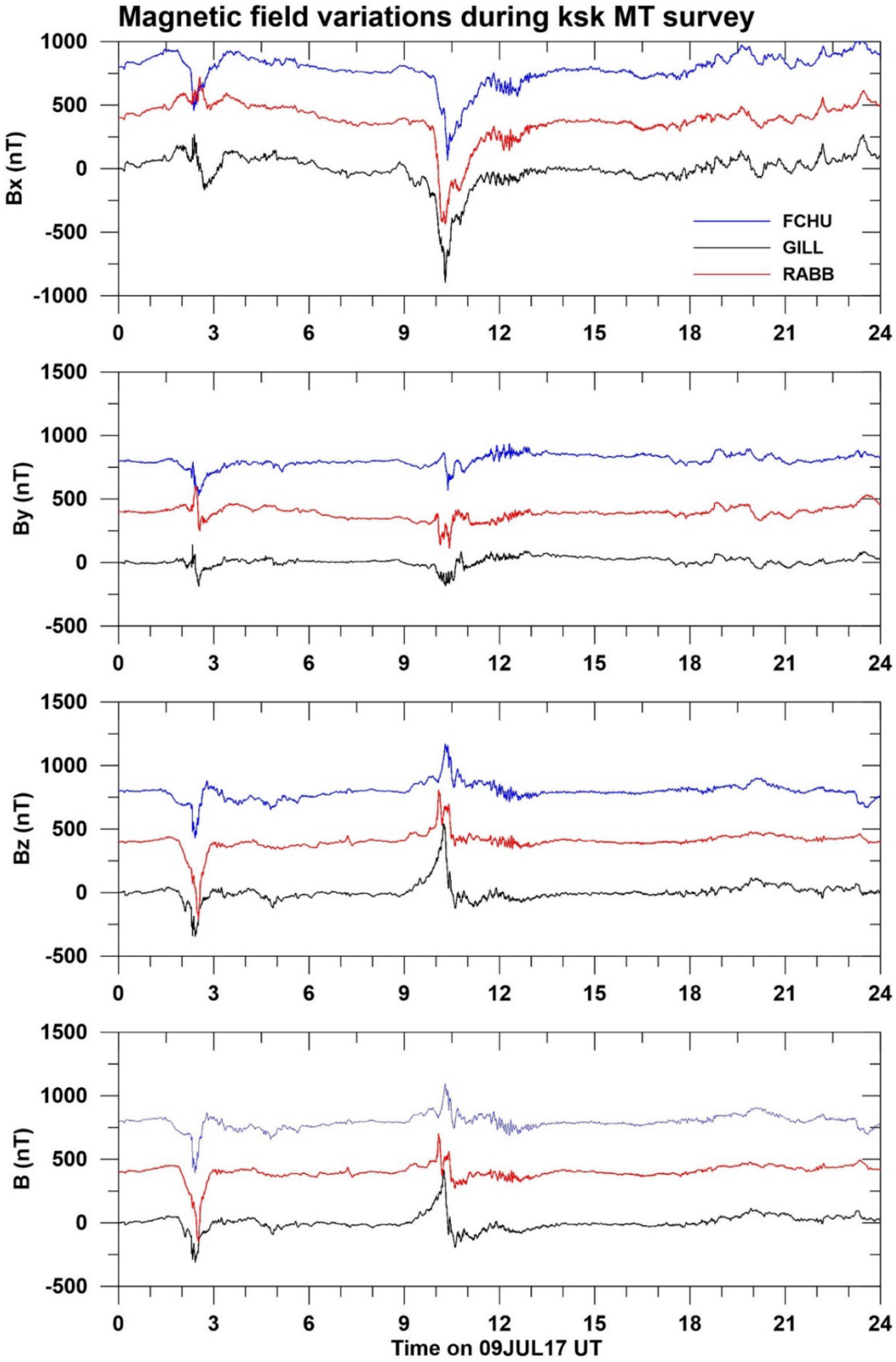

Figure 11. Magnetic field component variations for 09JUL17 for CARISMA sites GILL, RABB, and FCHU. To enhance clarity, a baseline value has been removed from each component and the RABB and FCHU data have been offset by 400 nT and 800 nT respectively.

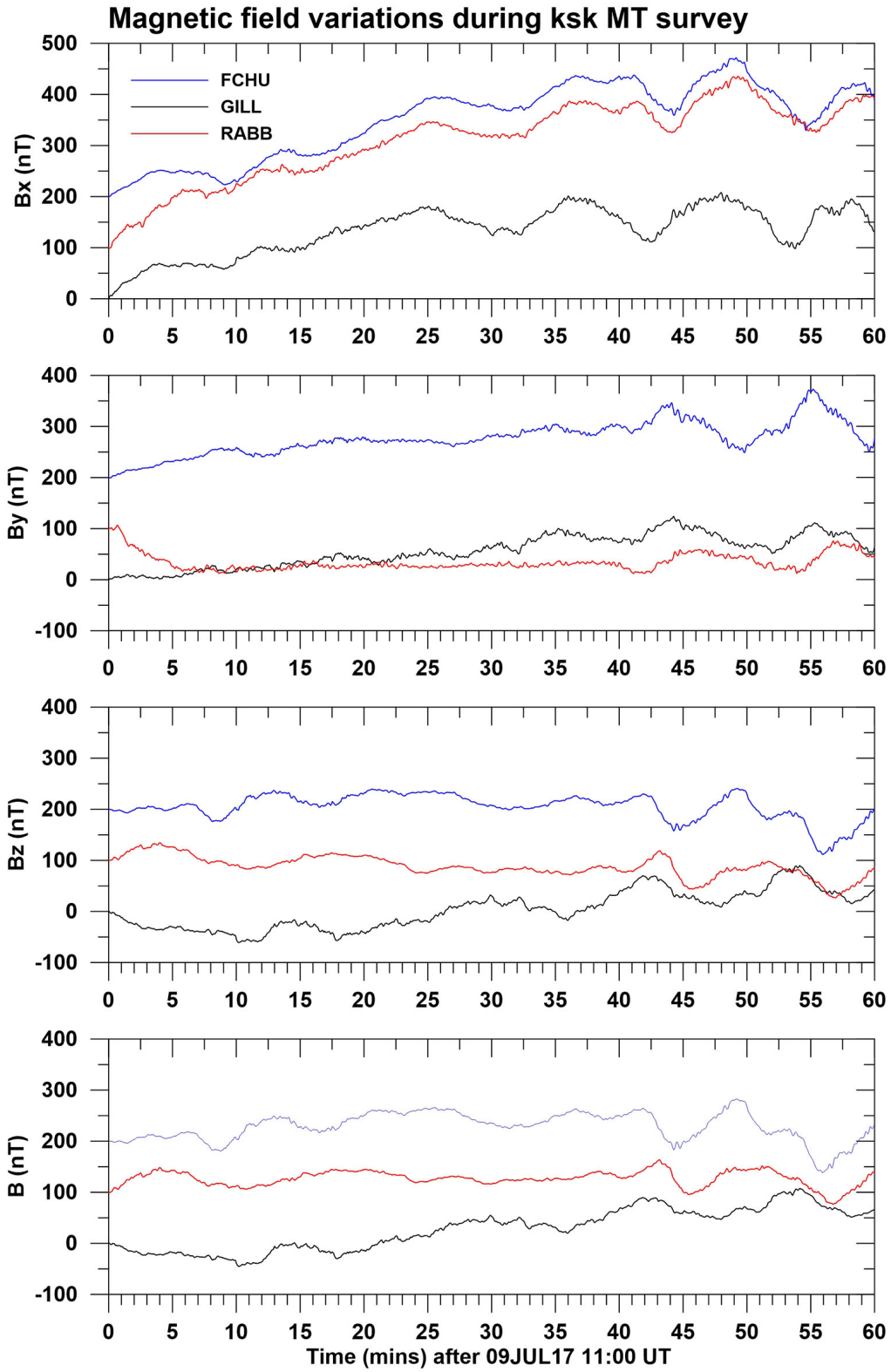

Figure 12. Magnetic field component variations for CARISMA sites GILL, RABB, and FCHU for 09JUL17 between 11:00 and 12:00 UT. Note the strong spatial variations in the signals. A baseline value has been removed from each component and the RABB and FCHU data have been offset by 100 nT and 200 nT respectively.

Figure 13 shows examples of shorter time series showing shorter period pulsation signals. Figure 13a shows the signals just prior to the event shown in Figure 12. There are clear spatial differences between the three sites. The RABB B_x and B_y components show relative strong 5–10 nT pulsations with

a period of ~24 s that are likely Pc2 signals occurring during the disturbed interval. The corresponding 3-hour k-index is 5.33. The corresponding pulsation signals at GILL and FCHU are extremely weak (<1–2 nT). The result suggests a fairly localized source, closer to RABB than two the other sites. Figure 13b shows a 1-minute time segment from 21:30 on the same day. This segment exhibits 4.5 s period pulsations with a ~1 nT magnitude on all magnetic field components at GILL and FCHU. The signal is not in-phase at the two sites. The period of the signal allows it to be interpreted as Pc1 pulsations. There is no indication of the signals occurring at the same time at RABB, suggesting the signal is due to localized sources near the longitude of GILL and FCHU.

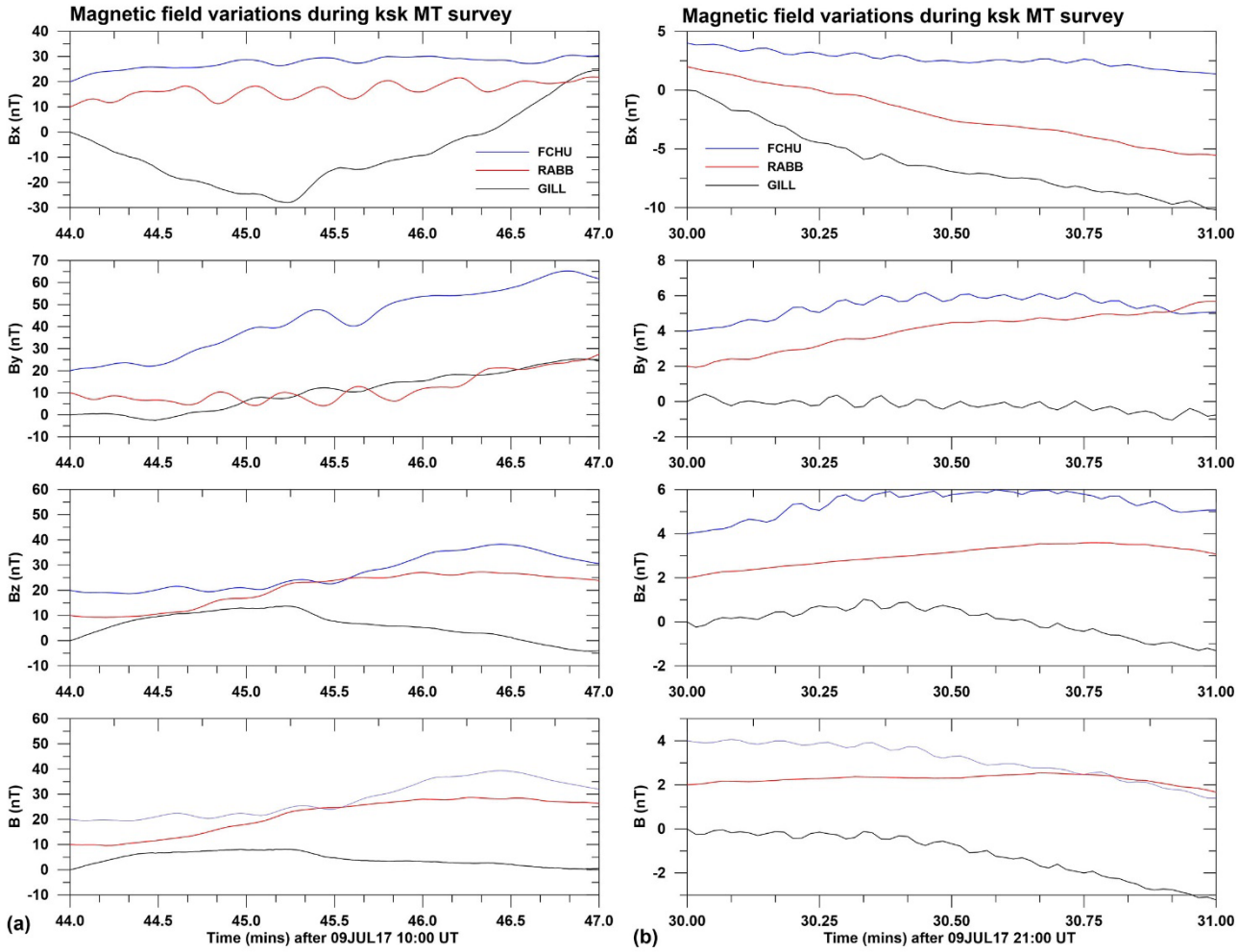

Figure 13. Magnetic field component variations for CARISMA sites GILL, RABB, and FCHU for short intervals on 09JUL17 UT. (a) Three-minute segment between 10:44 and 10:47 UT. A baseline value has been removed from each component and the RABB and FCHU data have been offset by 10 nT and 20 nT respectively. (b) One-minute segment between 21:30 and 21:31 UT. A baseline value has been removed from each component and the RABB and FCHU data have been offset by 2 nT and 4 nT respectively.

4.3 Spectra and spectrograms of longer-period (>1 s) geomagnetic signals

The frequency content of the geomagnetic signals can be observed in frequency spectra derived from the time-series, and the time-frequency variations can be observed in spectrograms. These show how the spectra vary with time. Figure 14 shows spectra of the magnetic field variations at selected CARISMA sites for 08JUL17 and 09JUL17. Spectra were calculated using the maximum taper method (MTM) implemented in **MATLAB**. The overall power is about a factor of 100 higher on the 09JUL17 corresponding to signals that are a factor of 10 larger. The spectra show a significant variation between

the two days, in all three components, at frequencies of >0.05 Hz (periods of <20 s). These differences relate to both signal levels and noise levels, and the noise is discussed in more detail below.

The B_x and B_y data for FCHU for the 08JUL17 show peaks at frequencies of 0.35 Hz and 0.25 Hz (periods of 3 s and 4 s) corresponding to Pc1 pulsations. The responses form two peaks in the B_z component and a broadened peak in the B_x and B_y components. The magnitude of the peaks is ~$3 \cdot 10^{-3}$ nT^2/Hz in the B_x component and $1 \cdot 10^{-3}$ nT^2/Hz in the B_y and B_z components. The RABB responses show only a single spectral peak at a frequency of 3.0 Hz (period of 3.3 s) mid-way between the two peaks at FCHU suggesting that the Pc1 pulsations are not spatially uniform. The RABB response has a magnitude of $1 \cdot 10^{-2}$ nT^2/Hz in the B_x and B_y components which is larger than at FCHU but no peak is not discernable in the B_z component. Corresponding spectral peaks are not discernable in the GILL spectra because of the high noise level.

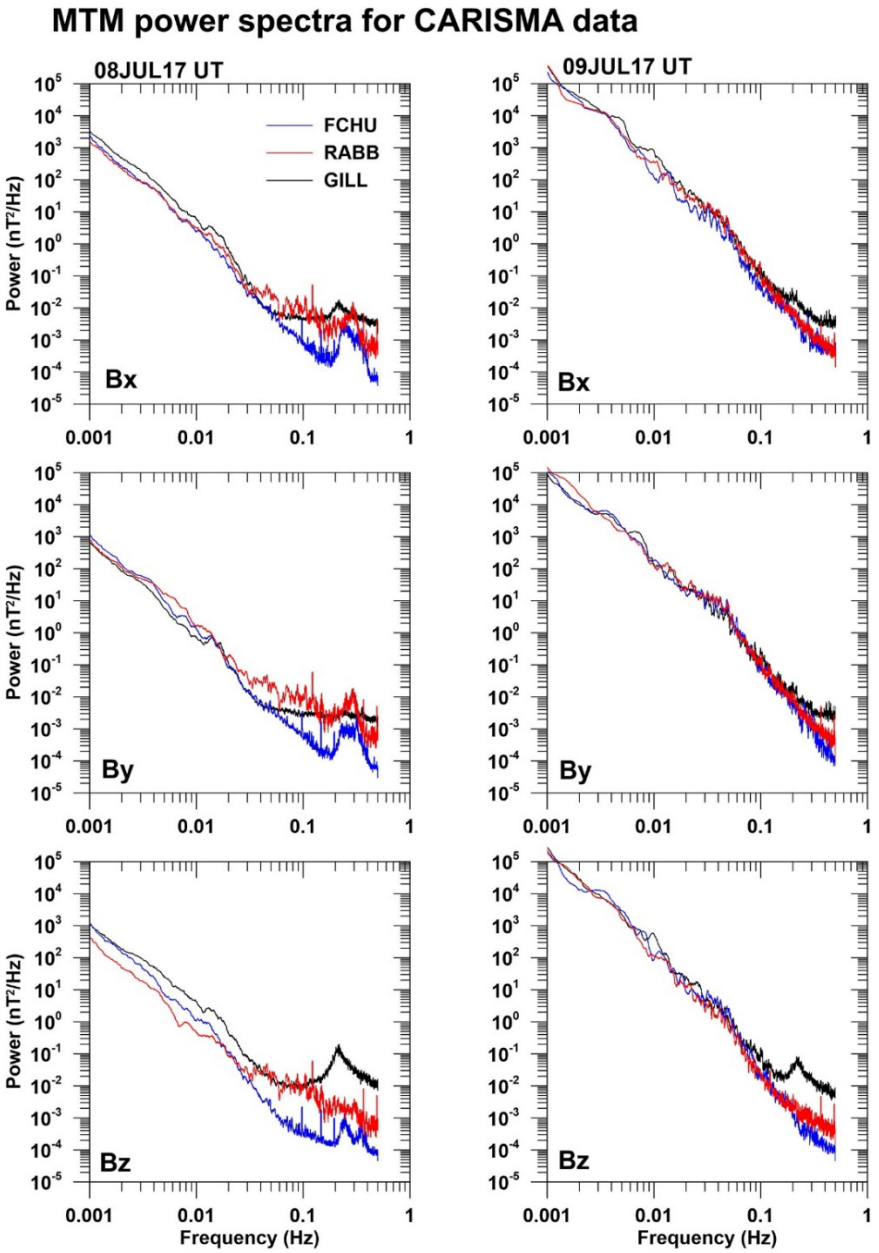

Figure 14. Maximum taper method (MTM) power spectra for 08JUL17 and 09JUL17 at CARISMA sites. The spectra are calculated using a band-width of p=64.

Figure 15 shows the spectra for two KSK sites for 08JUL17 and 09JUL17. The time series on which the spectra are based were obtained by converting the TS5 files for the corresponding recordings to ASCII format using the Phoenix utility **tstoasc**. The resulting data are ordered in columns corresponding to 15 Hz–sampled E_x, E_y, B_x, B_y, and B_z time series but these time series are uncorrected for the recording instrument and coil calibrations. The time series were resampled to 1 Hz sampling by taking every 15th point and then truncated so as to start at 0000 UT on the specified date, providing 15 hours of data for that day. Spectra were again calculated using the MTM approach and a band-width of p=64. B_z data were recorded using AMT coils and the flat spectra at the frequencies of <0.5 Hz (periods > 2 s) indicate the B_z time series contain only random signals in this range. The remaining field components confirm that the geomagnetic signals levels are a factor of 10 higher on the 09JUL17 than on 08JUL17 and the low signal levels on 08JUL17 allow other signals and noise to be observed.

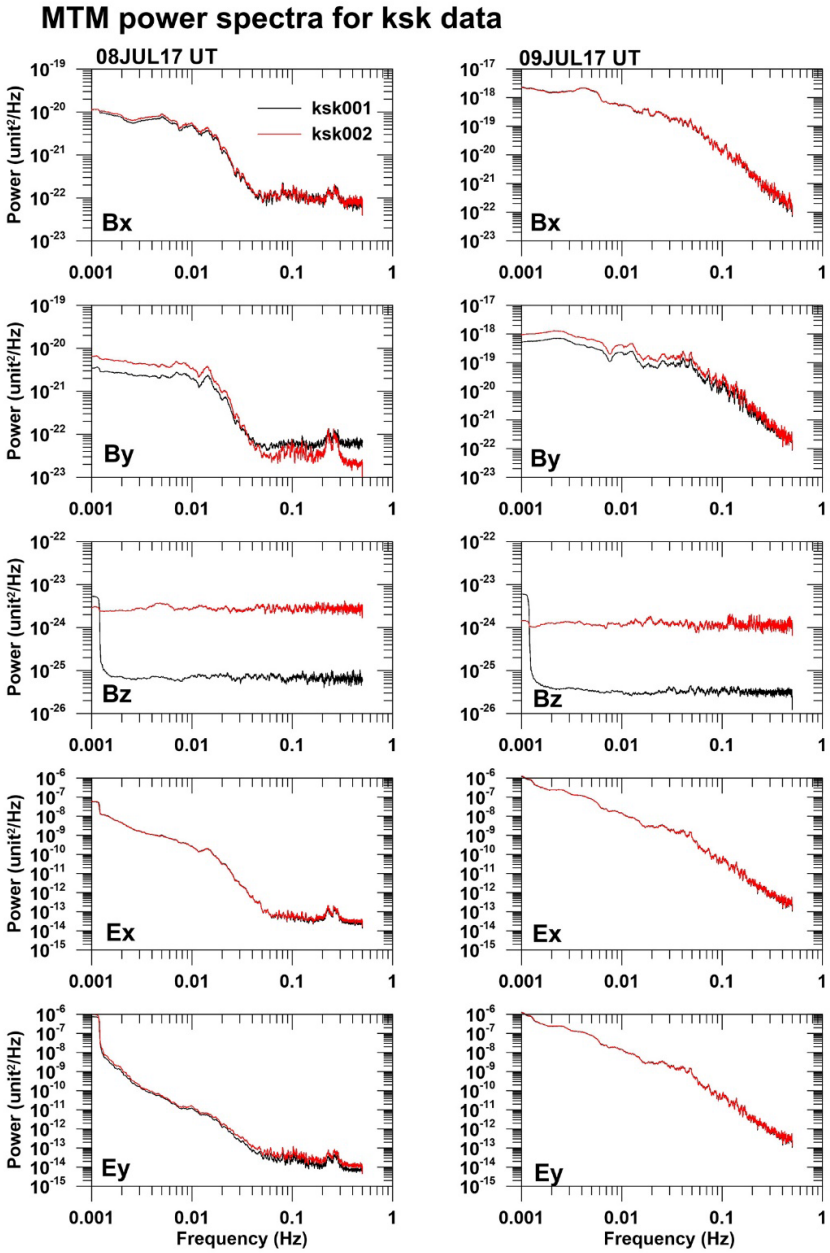

Figure 15. Maximum taper method (MTM) power spectra for 08JUL17 and 09JUL17 at sites ksk01 and ksk02. The spectra are calculated from 1 Hz time series using a band-width of p=64. Note that instrument calibrations have not been applied.

Pc1 pulsations can be observed at frequencies between 0.2 and 0.3 Hz (5 s and 3 s period). As observed at FCHU, the pulsations form two spectral peaks at the KSK sites. However, for KSK sites, the two peaks are closer in frequency than at FCHU again demonstrating the presence of spatial variations in the pulsation signals.

Figure 16 shows CARISMA spectrograms for GILL for the longer period (lower frequency) Pc5 channel and the shorter period (higher frequency) Pc1 channel. The increased disturbance level on 09JUL17, visible on Figures 9–13, is evident in both the long and short period channels on both magnetic field components. The Pc1 pulsations shown in Figure 13b can also be seen on both the B_x and B_y components.

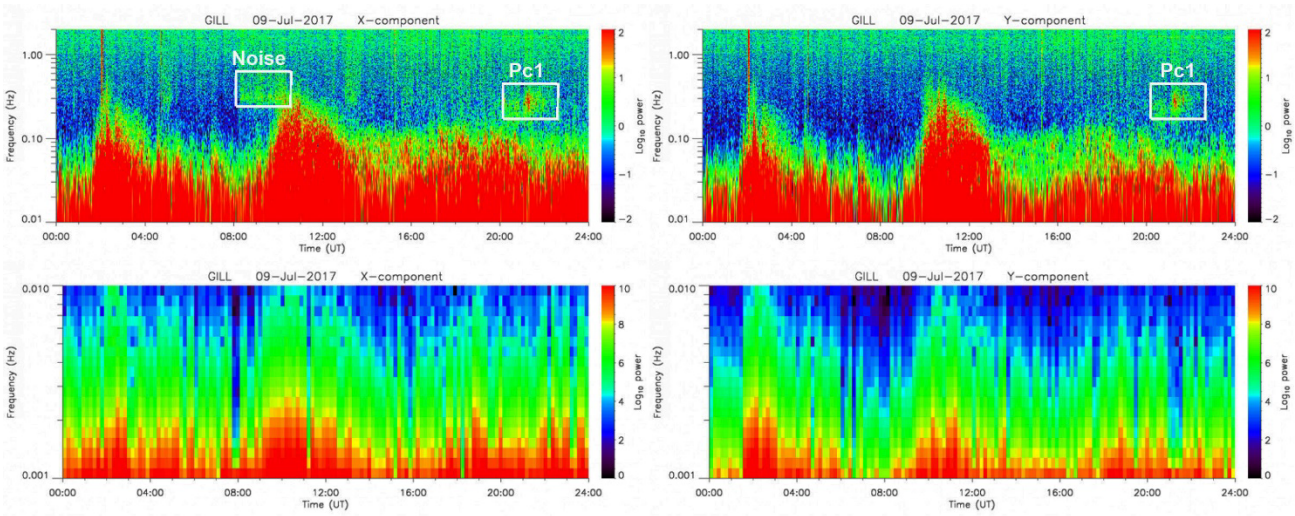

Figure 16. Spectrograms from GILL obtained from CARISMA for 09JUL17 UT. Lower panels show the low frequency (short period) Pc5 channel and upper panels show the high frequency (short period Pc1 channel). Left panels show B_x component and right panels show B_y component. A pulse of Pc1 signals is marked. A period of intense electromagnetic noise on the B_x component of the field is also marked.

Figure 17 and 18 compare the short-period spectrograms for GILL with those for FCHU and RABB for 08JUL17 and 09JUL17 UT. Figures 19 and 20 show corresponding spectrograms for 15 hours of data at ksk01 and ksk02. The spectrograms were calculated using the same time series data used to prepare the power spectra but in this case the data were left at the original 15 Hz sampling rate. Spectra were calculated for 1 minute (900 point) intervals using the MTM approach and a band-width of p=2. The result for B_z is a poor representation of the underlying signals, because this component was measured using AMT coils, providing limited sensitivity at frequencies of less than 1 Hz.

The spectrograms show background geomagnetic variation signal and Pc1 pulsation signals. All components exhibit a red spectrum in which the power decreases with increasing frequency. The frequency at which the transition between different colours provides a measure of the background signal strength: a colour transition moving to higher frequencies corresponds to an increase in signal strength. The presence and period range of the presence of the pulsation signals is more reliably discerned in the spectrograms than the MTM spectra. In the spectra, the pulsation response can be masked by other signals and noise that may at times have large magnitude than the pulsations.

Pc1 pulsations occur at all stations but are not synchronous. For example, on the 09JUL17 UT, the pulsation event at RABB starts approximately 1 hour later than at FCHU and GILL suggesting that its timing depends to a large extent on local time. Figure 13b shows a time interval just prior to the start of the pulsations at RABB explaining the absence of pulsations in the plotted time series at that site. The pulsations are visible for GILL in the spectrograms even though they cannot be discerned in the MTM spectra. The period of the pulsations varies between sites and events (Table 2). On 08JUL17, the pulsations occurring at FCHU appear in two closely-spaced but distinct frequency bands. For 13:00–

22:00 UT they have a frequency range of 0.3 to 0.35 Hz (period range of 3.0–3.5 s) and for 16:00–23:00 UT have a frequency range of 0.4–0.5 Hz (period range of 2.0–2.5 s). It is possible that the two frequency ranges correspond to eastward and westward electrojets.

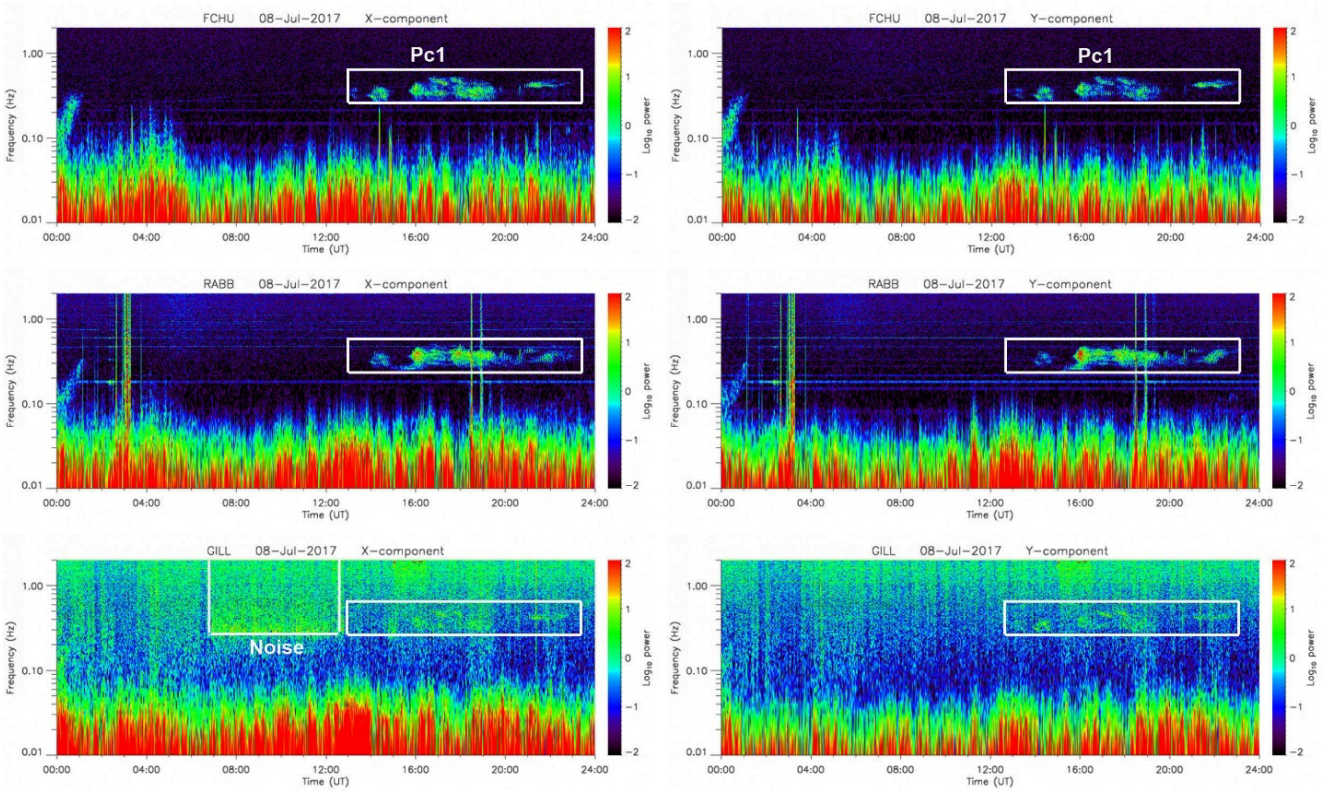

Figure 17. Comparison of short period CARISMA spectrograms at GILL, FCHU and RABB for 08JUL17. Left panels show B_x component and right panels show B_y component. A pulse of Pc1 signals is marked. The box is synchronous for all panels. Intense electromagnetic noise is visible only on the B_x component at GILL over the 5-hour period from 07:00-12:00.

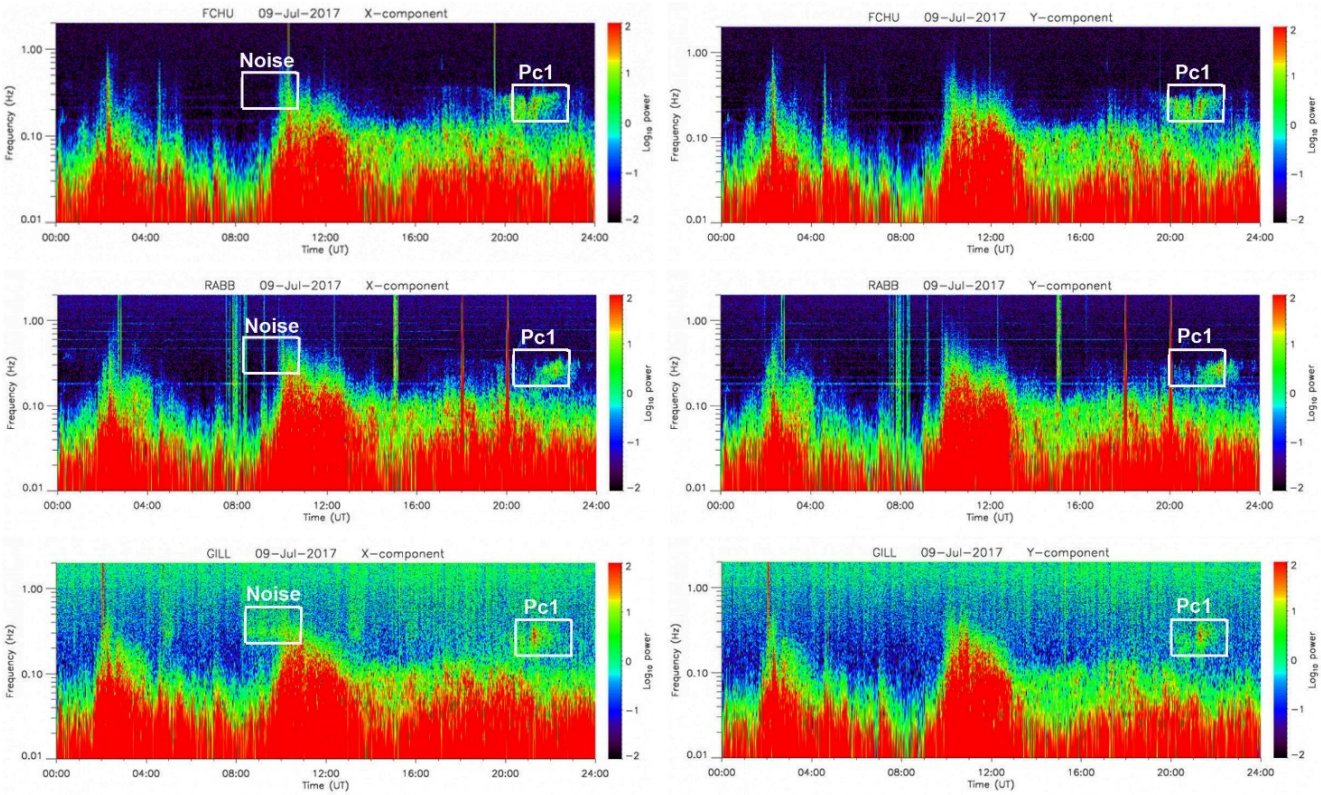

Figure 18. Comparison of short period CARISMA spectrograms at GILL, FCHU and RABB for 09JUL17. Left panels show B_x component and right panels show B_y component. A pulse of Pc1 signals is marked. The box is aligned for all panels showing the earlier start of the pulsations at FCHU and GILL.

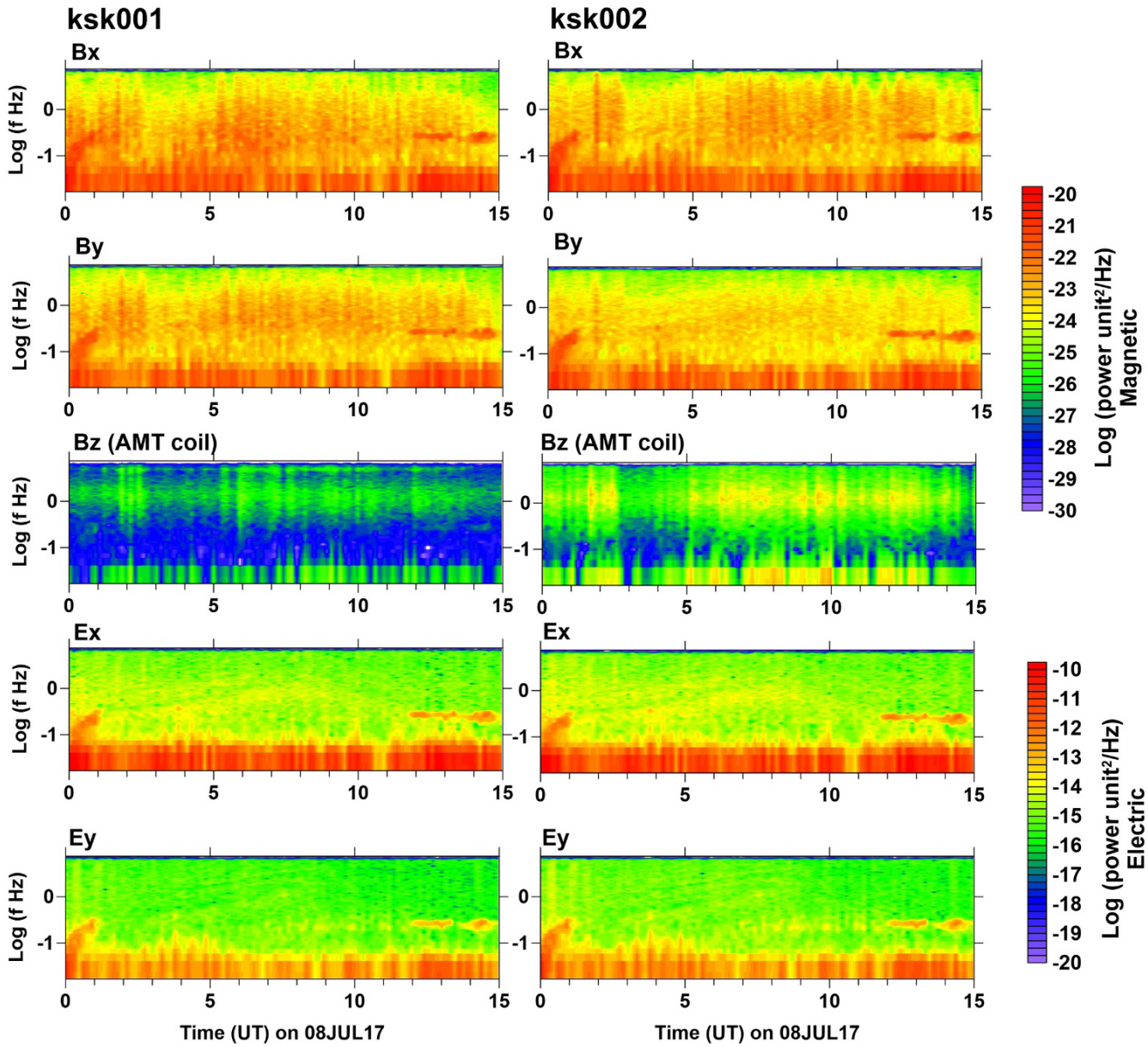

Figure 19. Comparison of KSK spectrograms at ksk01 and ksk02 for 08JUL17. The results are for uncalibrated time series. The B_z recordings used an AMT coil so have low sensitivity at frequencies less than 1 Hz.

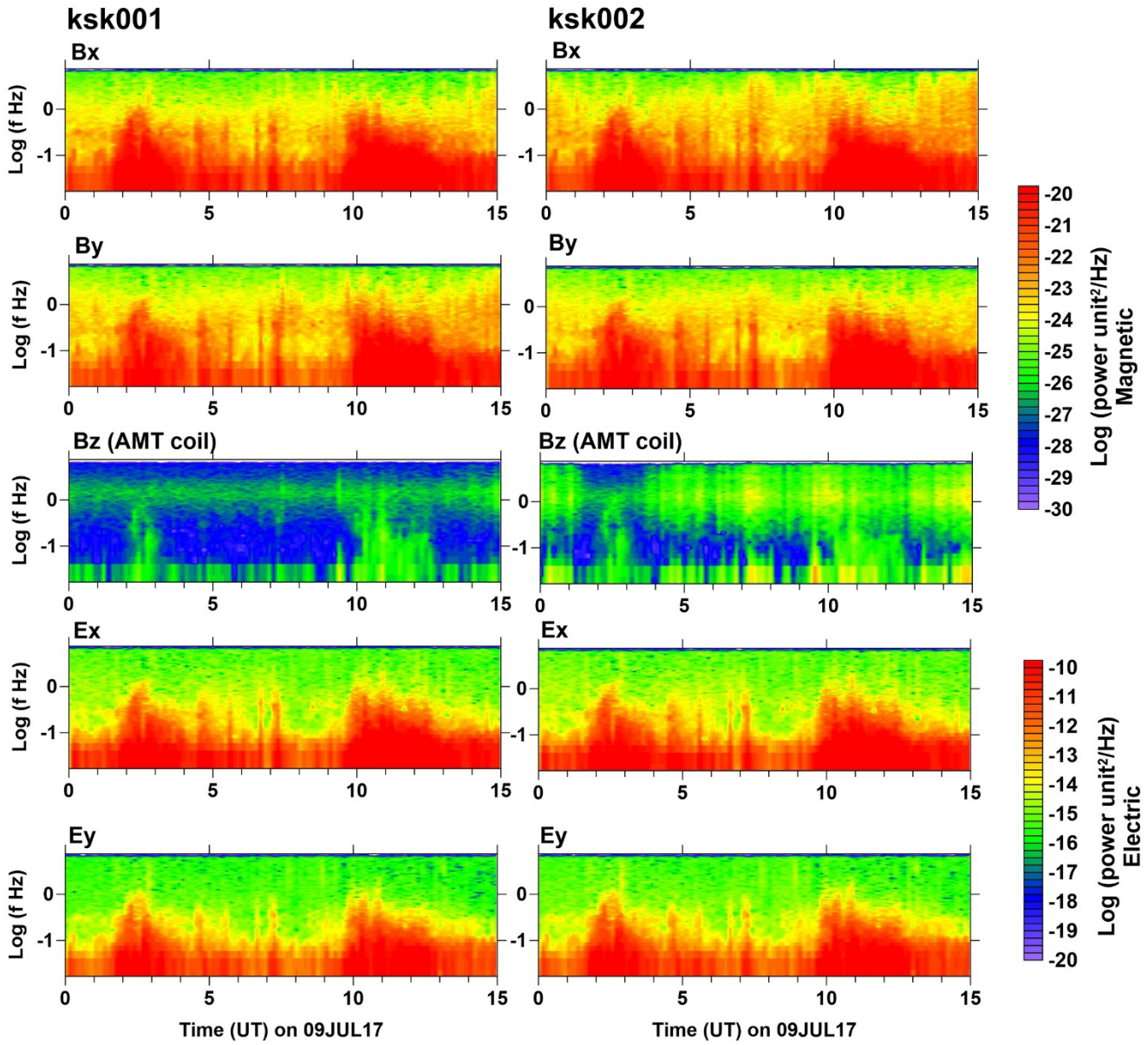

Figure 20. Comparison of KSK spectrograms at ksk01 and ksk02 for 09JUL17. The results are for uncalibrated time series. The B_z recordings used an AMT coil so have low sensitivity at frequencies less than 1 Hz.

Table 2. Observed frequency of pulsation signals on 08JUL17 and 09JUL17

Site/Response	FCHU	RABB	GILL	ksk01, ksk02
Spectrogram 08JUL17	1300–2000: 0.3–0.4 Hz 1630–2300: 0.4–0.5 Hz	1400–2300 0.25–0.45 Hz	1430–1930 0.25–0.4 Hz 1645–2300 0.4–0.5 Hz	1200–>1500: 0.2–0.35 Hz
Spectrogram 09JUL17	2000–2230 0.14–0.3 Hz	2130–2330 0.14–0.3 Hz	2030–2230 0.14–0.3 Hz	Occurred after MT recording
MTM spectrum 08JUL17	0.2–0.3 Hz, 0.3–0.4 Hz	0.2–0.4 Hz	Not visible	0.2–0.3 Hz
MTM Spectrum 09JUL17	Not visible	Not visible	Not visible	Occurred after MT recording

4.4 Spectra of higher frequency (>1 Hz) geomagnetic signals

Spectra of higher frequency geomagnetic signals were examined using the KSK MT data. Figures 21 and 22 show representative spectra from AMT recordings at ksk01 and MT recordings at ksk18 respectively. The spectra have the expected red frequency-dependence (Constable, 2016) with several additional responses superimposed. The AMT spectra show the low signals levels in the AMT deadband between about 2000 and 1000 Hz. The magnetic field responses have a relatively small slope

between 1000 Hz and 1 Hz (relative to the trend of the red spectrum observed at lower frequencies) yielding moderately low signals levels in the MT deadband around 1 Hz. There are localized peaks visible in the spectrum at 8 Hz and 14 Hz corresponding to the fundamental mode and second harmonic Schumann resonances (Ghosh et al., 2019). These signals are caused by resonances of electromagnetic signals produced by lightning in the wave-guide formed by the Earth's resistive atmosphere (Constable 2016, Ghosh et al., 2019). They are observed throughout the KSK survey. MT spectra for ksk18 also show a peak associated with Pc1 pulsations. Similar responses are observed for most days of the KSK recordings.

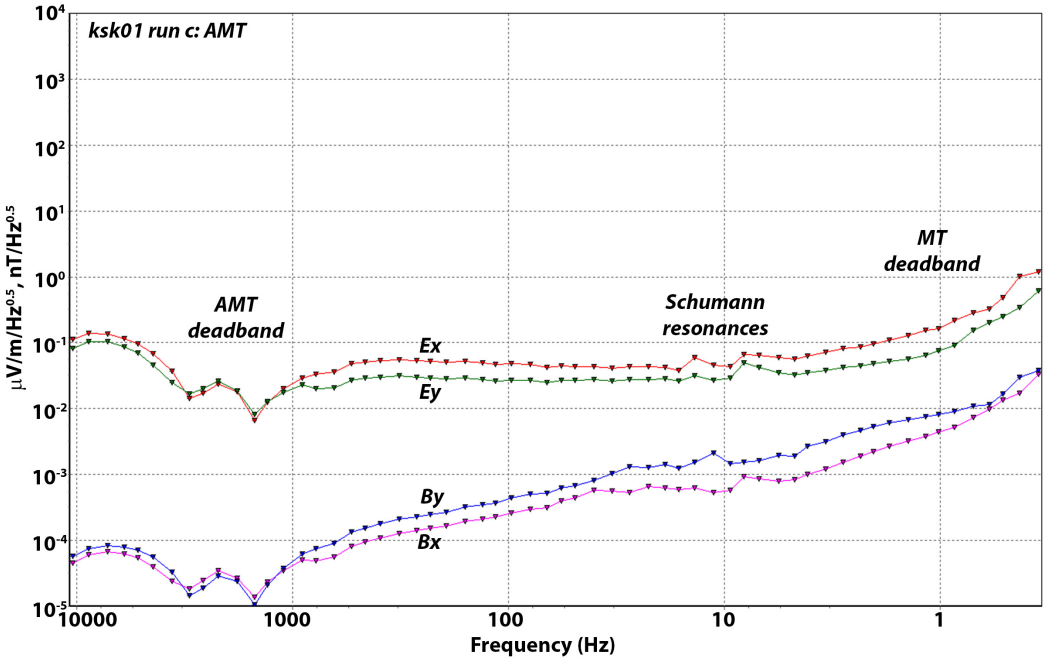

Figure 21. Spectra of horizontal electric and magnetic field components for the ksk01 AMT c run (starting 09JUL17).

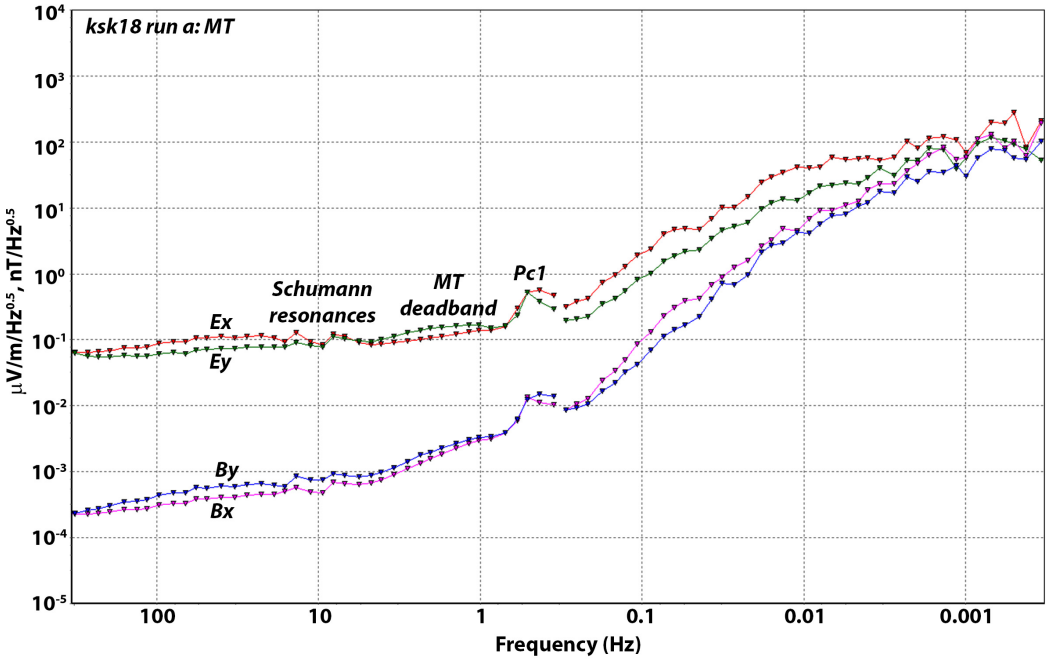

Figure 22. Spectra of horizontal electric and magnetic field components for the ksk18 MT a run (starting 13JUL17).

4.5 Discrimination of electrojet signals

The magnetic field recorded during the KSK survey was examined to determine whether there was a simple approach available for discriminating auroral electrojet signals in the data set. Figure 23 and 24 show time series and histograms for four-hour windows for GILL B_x and B_z data for a relatively disturbed day (09JUL17) and a relatively quiet day (13JUL17), chosen based on the auroral indices (Figure 9). The results for 09JUL17 show strong signals at the expected time of the electrojets but these signals may also be associated with, or enhanced by, the magnetic storm at this time. The large, long-period excursions show the same inverse correlation between B_x and B_z observed at shorter periods in the time series suggesting they are consistent with being produced by internal electromagnetic induction, and may therefore be related in part to magnetospheric (cf. ionospheric) signals. The histograms of the vertical magnetic field B_z data have heavy-tailed distributions with relatively large negative skew during the westward electrojet and relatively large positive skew during the eastward electrojet, consistent with the approach of Jones & Spratt (2002) in identifying auroral signals. However, it is difficult to definitely identify auroral events, or discriminate them from other geomagnetic events, using the standard deviation, skew, or kurtosis as these parameters are quite variable and the horizontal magnetic field components show similar levels of variation.

The results for the 13JUL17 show a single large long-period event, occurring later than the typical westward electrojet time and no evidence of an eastward electrojet signal. In contrast to the inverse correlation of B_x and B_z observed on the 09JUL17, this event exhibits a positive correlation between B_x and B_z so can be more readily identified as an electrojet signal. The difference in the sign of the correlation of B_x and B_z on the two days suggests a change in the position of electrojet relative to the latitude of GILL. The 13JUL17 event exhibits a strong negative skew in the corresponding histogram. However, the histograms cannot be used in isolation to definitively identify electrojet events, as some histograms from other windows from the same day also exhibit significant skew even though they are not associated with electrojet signals.

The results for the 09JUL17 and 13 JUL17 suggest that it is not possible to develop a fully automated scheme for processing the KSK MT data with the Phoenix software that is guaranteed to optimally reduce the effects of auroral signals. The timing of the electrojet events is variable, the sign of the relationship of B_x and B_z excursions is variable, and heavy-tailed statistical distributions of the data are not restricted to the times of the electrojet signals. Although more specialized analysis software could be written to address these aspects (e.g., Jones & Spratt, 2002) the intent in the current project is to make use of available Phoenix processing codes. The results above point to the necessity of using robust processing methods in this work. They also suggest that a quick approach to improving the long-period impedance responses may be to apply robust processing to day-time data outside the normal time-ranges e.g., from the time-range of 1100–2300 UT (or 06:00–18:00 CST).

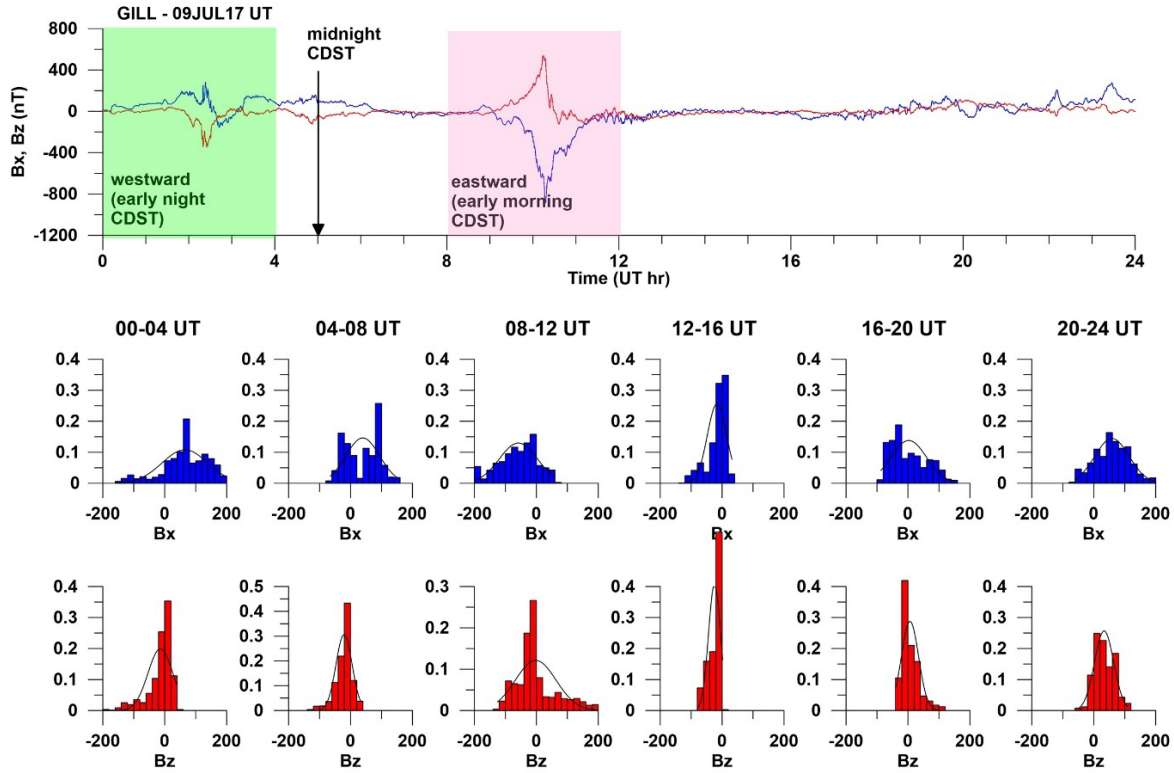

Figure 23. GILL B_x and B_y time series and histograms for a day with large auroral indices (09JUL17). Coloured areas on the time series indicate typical time for westward (green) and eastward (pink) electrojets.

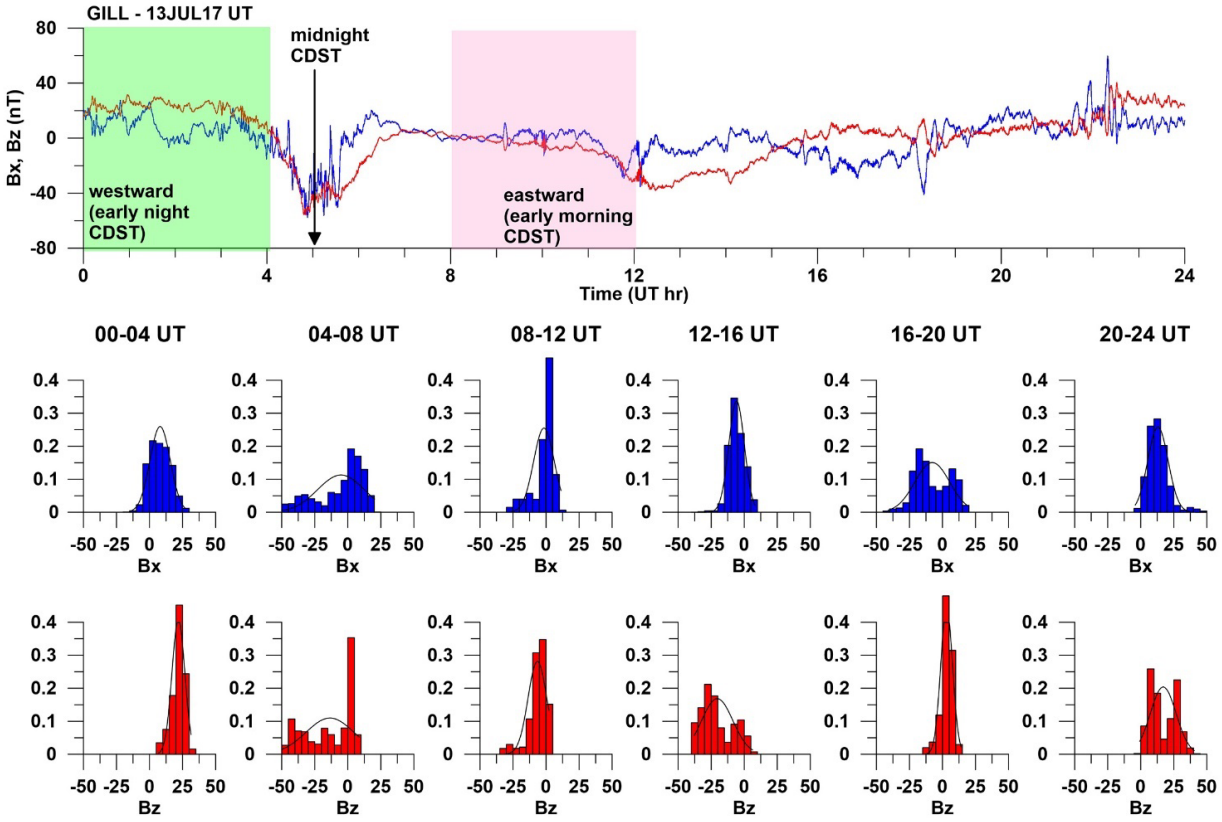

Figure 24. GILL B_x and B_y time series and histograms for a day with small auroral indices (13JUL17). Coloured areas on the time series indicate typical time for westward (green) and eastward (pink) electrojets.

5. Artificial electromagnetic noise

In this section, time series, spectra, and spectrograms are used to identify types of artificial (anthropogenic) noise present in the Gillam and KSK data set and the characteristics of the different noise. The Gillam noise is examined because of the possibility that the same sources of noise may affect the KSK MT data set.

5.1 Electromagnetic noise at Gillam

The spectra and spectrograms for GILL show the higher frequency response at that site is much noisier than at FCHU or RABB. The FCHU and RABB spectrograms do exhibit some noise including a number of horizontal lines on the spectrograms in Figure 17, 18 corresponding to line peaks on the power spectra in Figure 14. These noise sources are constant over time and therefore appear to be of instrumental origin. In contrast, the higher frequency part of the MTM spectrum for GILL (Figure 15) indicates the presence of broad-band noise with a central peak centred on a frequency of 0.21 Hz (period of 4.8 s). Examination of the spectrogram for 08JUL17 shows there are actually two sources of noise present at GILL.

1. A time-varying broad-band noise present on all three magnetic components.
2. Narrow band noise centred on 0.21 Hz (4.8 s period) that is present in the B_x and B_z components and at lower magnitude in the B_y component.

Figure 25 illustrates time series examples of the two types of noise.

The noise at GILL is attributed to hydroelectric facilities and infrastructure in the area. Electromagnetic noise has also been noted in previous surveys conducted in the Gillam area, e.g., as reported in Goldak Airborne Surveys (2005) and in Tournerie & Coulson (2010).

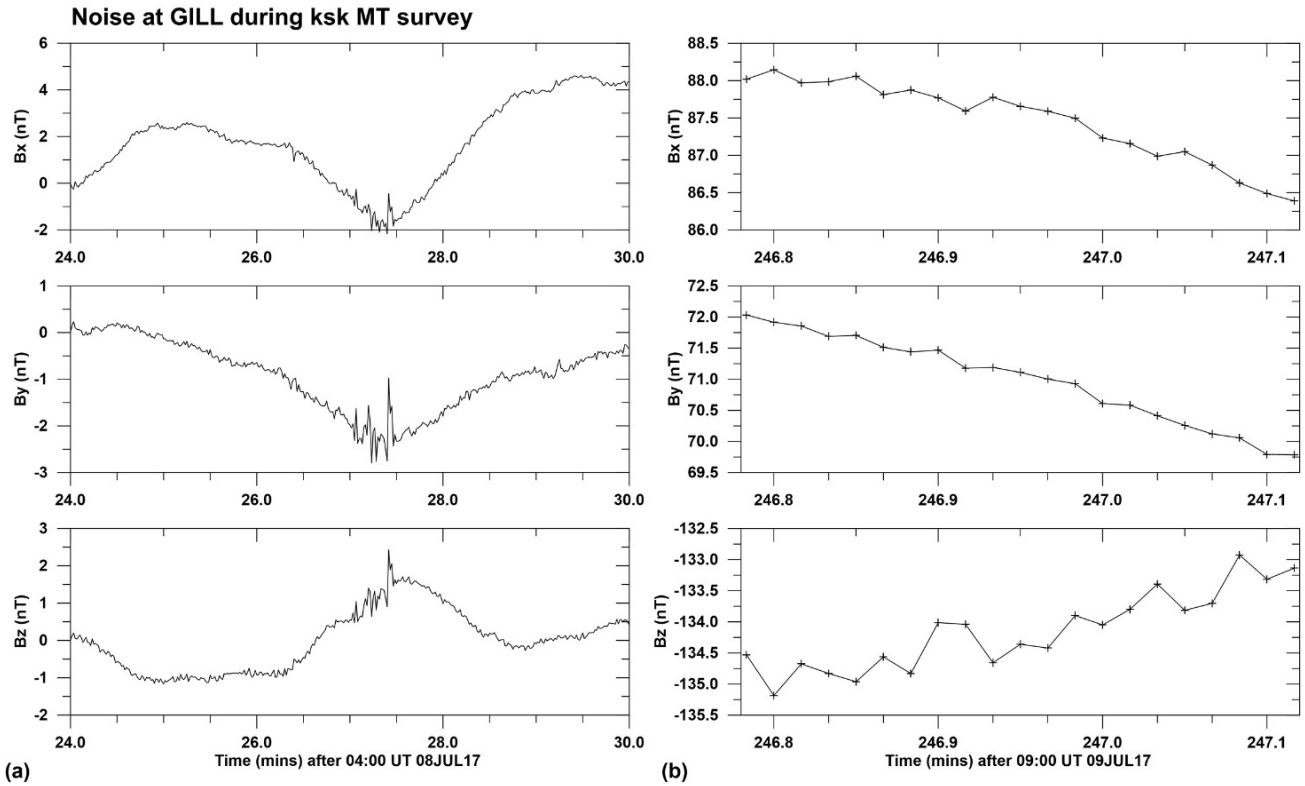

Figure 25. Types of noise recorded at GILL. (a) Broadband noise containing spike like features. (b) Narrow band noise centred on T=4.8 s.

5.1.1 Broad-band noise Examination of the B_x and B_y spectrograms (Figure 17, 18) show that that the time-varying broad-band noise is manifest as a series of vertical (i.e., broad-band) stripes of variable intensity with a curtain-like appearance. The absence of a corresponding response at RABB and GILL confirms that the response is local electromagnetic noise rather than geomagnetic signal. There are times when the noise is particularly strong such as between 01:00 to 04:00 UT and at 22:00 UT on 08JUL17 and 04:30 and 15:30 on 09JUL17.

Examination of the time series for one of the noise events (Figure 25) show that it consists of an irregular burst of magnetic field variations lasting several tens of seconds. The spiky nature of the variations produces the broad frequency content. The noise will be partially aliased in the 1 Hz sampled data as the spectrograms show the response contains frequencies as high as 2 s (periods as short as 0.5 s) i.e., signals with frequencies greater than the Nyquist frequency of 0.5 Hz. The noise is highly correlated in the B_x, B_y, and B_z components and has a similar amplitude of a few nT on each component.

The noise causes the flattening of the power spectra on 08JUL17 at $4 \cdot 10^{-3}$ nT^2/Hz for B_x, $3 \cdot 10^{-3}$ nT^2/Hz for B_y, and 10^{-2} nT^2/Hz for B_z (Figure 13). For these data, the noise can be discerned as extending from frequencies as low as 0.045 Hz (periods of 22 s) to at least the Nyquist frequency of 0.5 Hz. However, this visible range depends on background signal levels, so the noise may also include power at longer periods. As shown in the spectrograms, the noise is present at a similar level on 09JUL17 as on the previous day but it is almost completely masked in the power spectra by the higher geomagnetic signal levels.

5.1.2 Narrow-band noise Inspection of the spectrogram for 08JUL17 (Figure 17) shows the narrow-band noise was present over the period 07:00 and 12:00 UT. The narrow band noise at GILL can be seen at the lower frequency half of a box labelled "noise" in the spectrogram. This event was the longest interval of this noise during the KSK survey. It occurred during a period of intense broadband noise and also coincided with part of the first night of MT recording. Inspection of the spectrogram for 09JUL17 (Figure 18) shows a shorter period of similar noise from 08:00 to 11:00 UT. The absence of any corresponding responses at FCHU and RABB shows that this is local electromagnetic noise.

The time series plot of the narrow-band noise (Figure 25b) shows that the noise is strongest in the B_z component (~3 nT) but is also present in the B_x component (~1 nT) and is present at very low magnitude (<0.2 nT) in the B_y component. The consistency of the polarization of the signal was examined by plotting the difference of adjacent points in B_x time series versus the difference between the adjacent B_z points (Figure 26). The differencing was done to remove the longer period trends in the data. The result reveals strongly polarized variations with some natural signals superimposed. The typical magnitude of the B_z component variations in the differenced data is 2.5 nT and the magnitude of the B_x component variations is 0.7 nT. A linear trend fitted to the data has an r^2 coefficient of 0.81 for the 61 points plotted, and indicates a ratio of B_z to B_x variations of 3.36 corresponding to a magnetic field inclination angle of atan(3.36)=73º.

The power spectra (Figure 14) show that the narrow band signal is centred on 4.8 s period. It is strongest in the B_z component where the peak is ~10^{-1} nT^2/Hz. In the B_x component the peak is $2 \cdot 10^{-2}$ nT^2/Hz and in the B_y component it is ~$3 \cdot 10^{-3}$ nT^2/Hz.

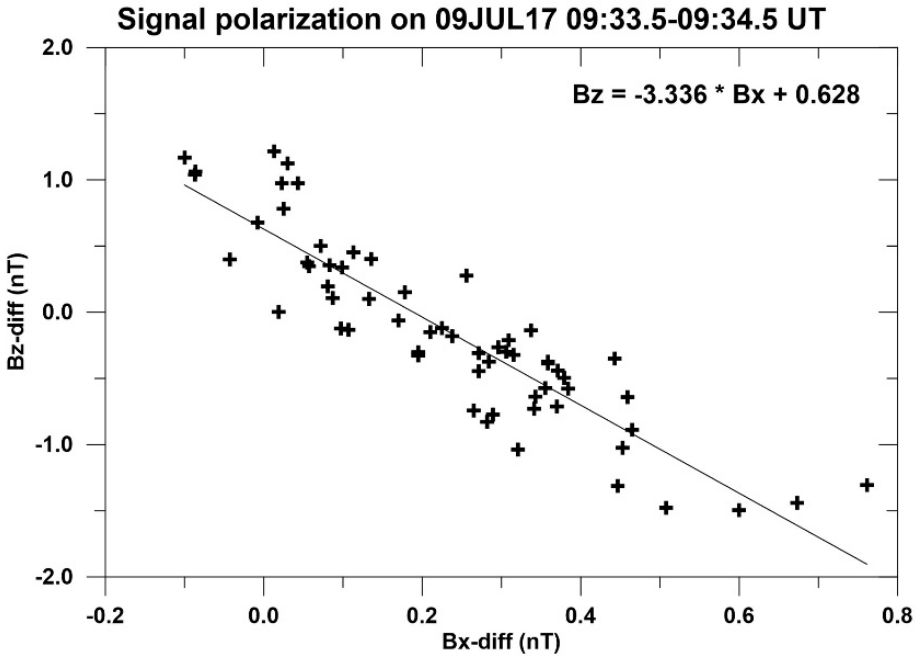

Figure 26. Examination of the polarization of the 0.21 Hz noise signal in the B_x-B_z magnetic field components.

5.2 Electromagnetic noise in the Kaskattama survey area

Inspection of time-series, spectra, and spectrograms for data collected at sites ksk01 and ksk02 show the broadband noise that was observed at GILL was also present in the Kaskattama area but the narrow band noise observed at GILL is not present. In addition, the KSK magnetic field data contain other forms of noise.

5.2.1. Broadband noise The KSK spectra and spectrograms (Figures 15, 19, and 20) show similar broad band noise as the GILL data (Figure 14, 17, and 18). As at the CARISMA sites, the broad-band noise at the KSK sites is most evident on 08JUL17 when the natural signal levels were lower. In the uncalibrated time series, the level of the noise is about 10^{-22} power units in B_x, $2{\cdot}19^{-23}$ to 10^{-22} power units in B_y, and 10^{-14} power units in E_x and E_y. On 08JUL17, the spectra for these channels are dominated by the noise at frequencies exceeding $3{\cdot}10^{-2}$ Hz (or periods less than about 30 s). The level of the white noise response on the B_z channels is 10^{-25} power units for ksk01 and $3{\cdot}10^{-24}$ power units for ksk02. These levels are much smaller than the level of the broad-band noise on the horizontal magnetic field components, suggesting that the noise is absent from the vertical component in the area of the KSK survey.

Figure 27 shows time series for a 1-minute segment at ksk01 and ksk02 on 08JUL17. Comparison of the response with Figure 19 shows that the semi-periodic signals (with a frequency of 0.28 Hz or period of 3.6 s) are Pc1 signals. They can be seen on all four horizontal electric and magnetic field components at both sites although they are harder to discern in the E_y time series because of stronger long-period geomagnetic signals. The time series is for a period in which the spectrogram showed broad-band noise (the vertical striping in Figure 19). The corresponding noise bursts in the time series are shaded in green in Figure 27. Each burst last several seconds. As also shown by the spectra in Figure 15, the broadband noise clearly affects all four horizontal magnetic and electric field components at both KSK sites.

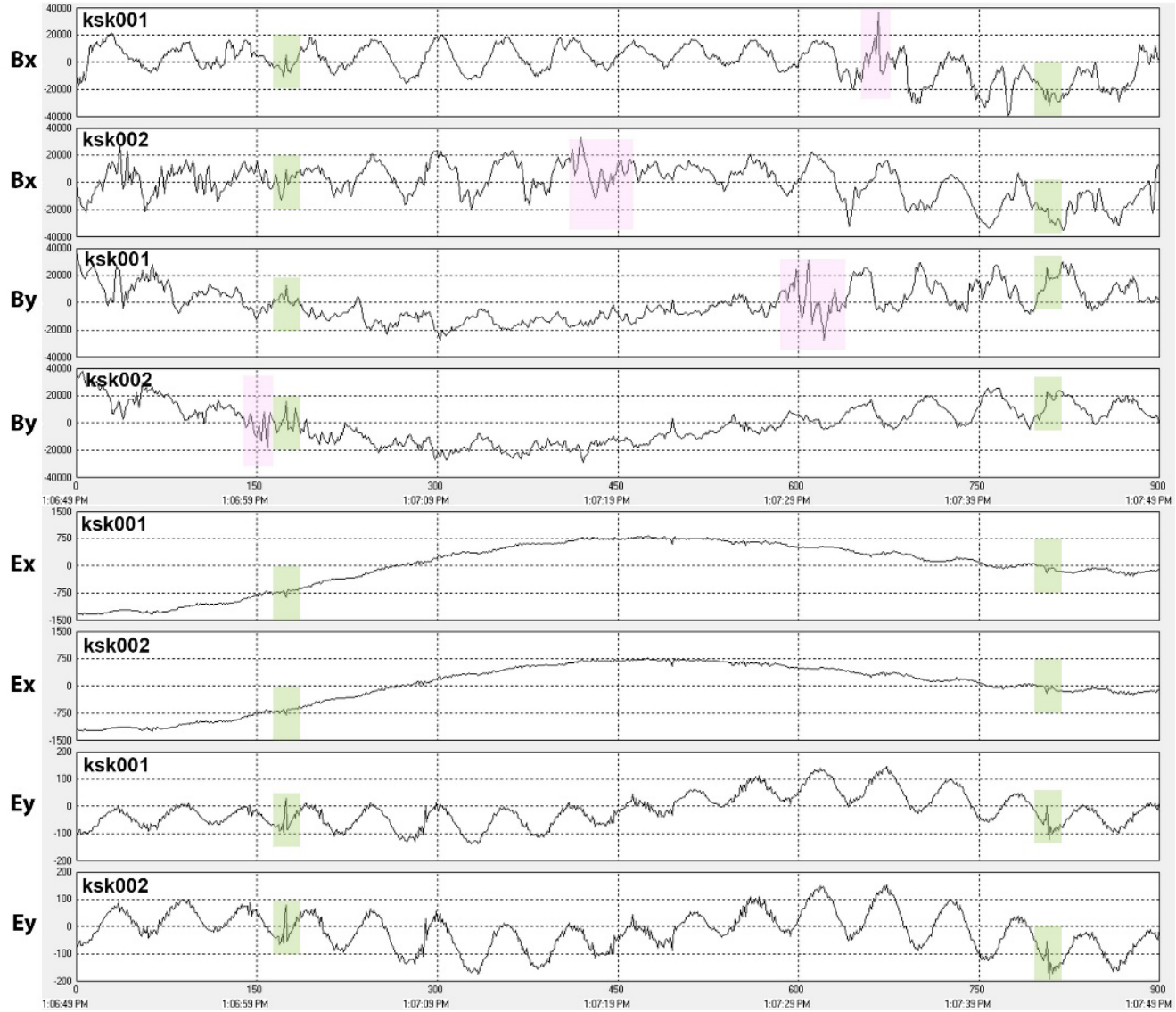

Figure 27. Comparison of one-minute long time series from ksk01 (upper plots) and ksk02 (lower plots) starting at 08JUL17, 13:06:49 UT during a period of moderate noise at GILL (Figure 18). The figure shows uncalibrated time series plotted using the Phoenix Geophysics TSVIEWER program. Green shading shows times of synchronous noise on all four components at both sites and pink shading shows times of noise on individual magnetic field components at individual sites. The semi-periodic signals are Pc1 pulsations.

5.2.2. Individual-component magnetic field noise Inspection of Figure 27 shows that although the electric field components are very similar at the two sites, there are differences in the magnetic field components. There are events at ksk01 such as the B_x event at ksk01 at 13:07:33 or the B_y event at 13:07:29 that are not present at ksk002. Likewise, there are smaller events at ksk02 such as the B_x event at 13:06:31 and the B_y event at 13:06:59 UT that are not present at ksk01. There is no correlation of this noise between different components or different sites and there is no corresponding noise in the electric field components. Inspection of the vertical magnetic field time series shows no corresponding effects. The noise appears to be relatively broad-band so has a similar effect on the spectra as the broadband noise described in the previous section.

The absence of any correlation of the noise between magnetic field components and different sites, and the absence of any corresponding noise on electric field channels, indicates that the noise must be due to very local effects that occur independently at the location of each sensor coil. Its occurrence at different times on different field components rules out an instrumental electromagnetic noise

associated with the Phoenix MT instrument recording boxes. The only feasible source of instrumental noise that could explain the observations is a source associated with the individual MT coil amplifiers.

An alternative explanation for the noise is that is due to local ground motions, such as differential frost heave causing coil movement in the peat-based soils at the sites (e.g., Peterson and Krantz, 2003. The larger amplitude of the events at ksk01 may be explained by the proximity of this site to Bouchard Lake and increased soil moisture content. The noise is particularly evident on 08JUL17 because of the low geomagnetic signal levels that day. It is difficult to investigate the noise in greater detail because of the higher signal levels on subsequent days.

5.2.3 High-frequency vertical magnetic field noise The vertical magnetic field B_z spectra for the KSK sites reveal the presence of an additional form of noise centred on the frequency range from ~200 Hz to ~50 Hz. The noise is clearly visible in the **TS3** time series. Figure 28 shows examples of this noise in spectra and Figure 29 shows examples in terms of time-series. Closer inspection of the noise using higher resolution spectra (not shown) suggests it consists of a series of spectral peaks at 55 Hz and harmonic frequencies with broadening of the peaks in computed spectra caused by non-stationarity of the signal.

The noise is associated with the AMTC-30 coils, which were used for the vertical magnetic field recordings, but not the MTC-50 coils used for the horizontal magnetic field recordings. A check reveals it is also present in recordings made with these AMTC-30 coils in a previous survey at the Aquistore CO_2 sequestration site in southern Saskatchewan in 2015 (McLeod et al., 2018) and during a subsequent survey on Southampton Island in 2018 (Craven et al., 2018). In the Southampton Island AMT-based survey, the noise is evident in the Phoenix Geophysics Ltd. **EMT**-band responses which are derived from the AMTC-30 coils but not in the **HMT**-band responses which are derived from the MTC-50 coils.

The noise is also sometimes observed in the horizontal magnetic field responses when they are recorded with AMTC coils, although it is generally much larger in the vertical magnetic field recordings. The noise level varies between coils, e.g., AMTC-1170 exhibits an almost zero level of noise whereas AMTC-1328 exhibits a relatively noisy response. Examination of calibration files showed no evidence of any issues in the calibration responses. The noise for individual coils does not have a constant level.

The coil noise is interpreted to result from an interaction of the AMTC-30 coils with local installation and/or geomagnetic conditions. The vertical magnetic field coils are typically deployed with part of the coil above grade and buried under a thinner soil cover than the horizontal coils. The response may be due to coil resonances associated with mechanical vibration of the AMTC coils, or to an unexpected electrical resonance response of the coils to higher frequency electromagnetic signals.

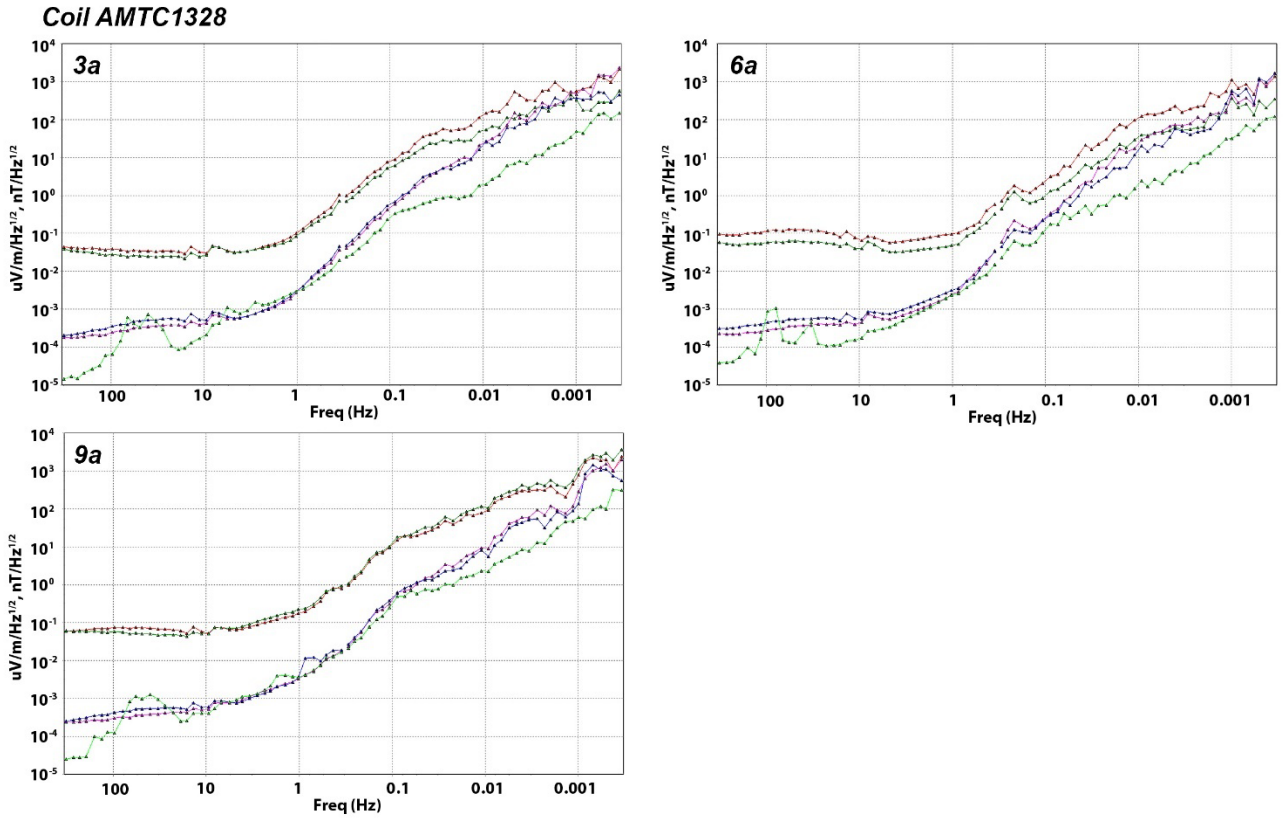

Figure 28. Spectra for sites at which AMTC-30 coil 1328 was used for vertical magnetic field recordings. Results are for the first day of recording at ksk03, ksk06, and ksk09. Note the peaks in the vertical magnetic field response (green symbols) between 100 and 10 Hz. This coil exhibited relatively strong noise characteristics.

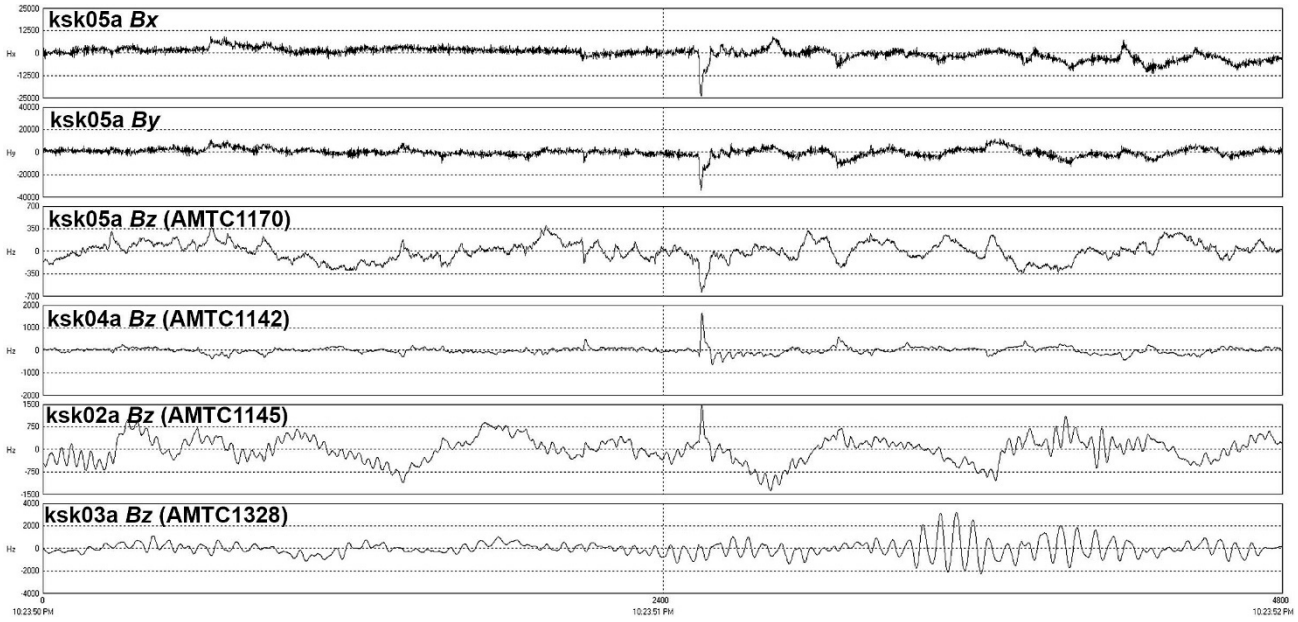

Figure 29. TS3 time series for 2 s of data on 08JUL17. The upper two panels show horizontal magnetic field responses recorded by MTC-50 coils and the lower four panels show vertical magnetic field responses recorded by AMTC-30 coils. Inspection of corresponding spectra shows that AMTC-1170 exhibits an almost zero level of noise whereas AMTC-1328 exhibits a relatively noisy response (as shown in Figure 28).

6. Effects of noise and auroral signals on MT responses

In this section the effects of the artificial noise and the auroral signals on the MT responses are investigated. Local magnetic field noise at an MT site will bias the magnitude of the local-B processed responses downwards, and local electric field noise at a site will bias the magnitude of the local-E processed responses upwards. Magnetic field noise that is correlated between the main site and the remote site will bias the magnitude of remote-B processed responses downwards, and correlated electric field noise will bias the magnitude of the remote-E processed responses upwards. The effect of auroral signals may be more irregular but it is expected to be more prominent at longer periods (lower frequencies).

6.1 Effects of noise and auroral signals on robust remote-reference responses

The effect of noise and auroral signals on the MT responses calculated using default processing parameters (see Section 2.2) is examined next. Results for the relatively quiet day of 13JUL17 for site ksk17 were calculated using the B and E fields from ksk18 as the remote reference. Figure 30 shows the spectra of the time series used for the recordings, and figures 31 and 32 show the apparent resistivity/phase and tipper responses.

The spectra for all components have a red form with a relatively narrow band peak at ~0.5 Hz (~2 s) that is likely due to geomagnetic pulsations. There is strong broad-band noise at 200-20 Hz (0.05–0.5 s) in B_z noise associated with the AMTC-30 coils. There is also very strong narrow band noise centred on 1 Hz (1 s) in B_z with possible corresponding weak response in B_x and B_y but definitely no corresponding noise in R_x and R_y. Over most of the frequency range (0.001-10 Hz) (or period range 0.1 – 1000 s) the B_x response is significantly larger than R_x.

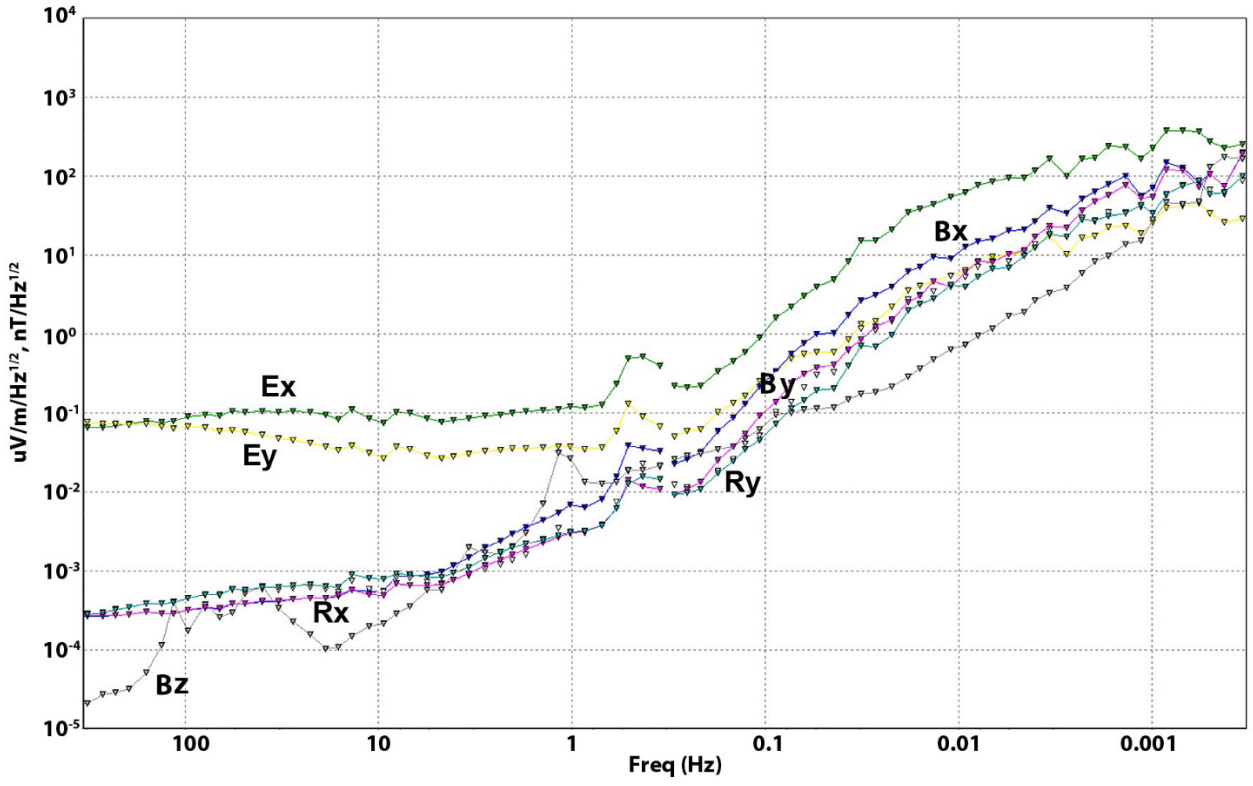

Figure 30. Spectra for ksk17 for deployment on 13JUL17. Responses computed using the full time series (~23 hours) and default infield robust processing parameters (see Section 2.2). Colour coding is E_x=green, E_y=yellow, B_x=blue, B_y=white, R_x=magenta, R_y=teal, B_z=grey.

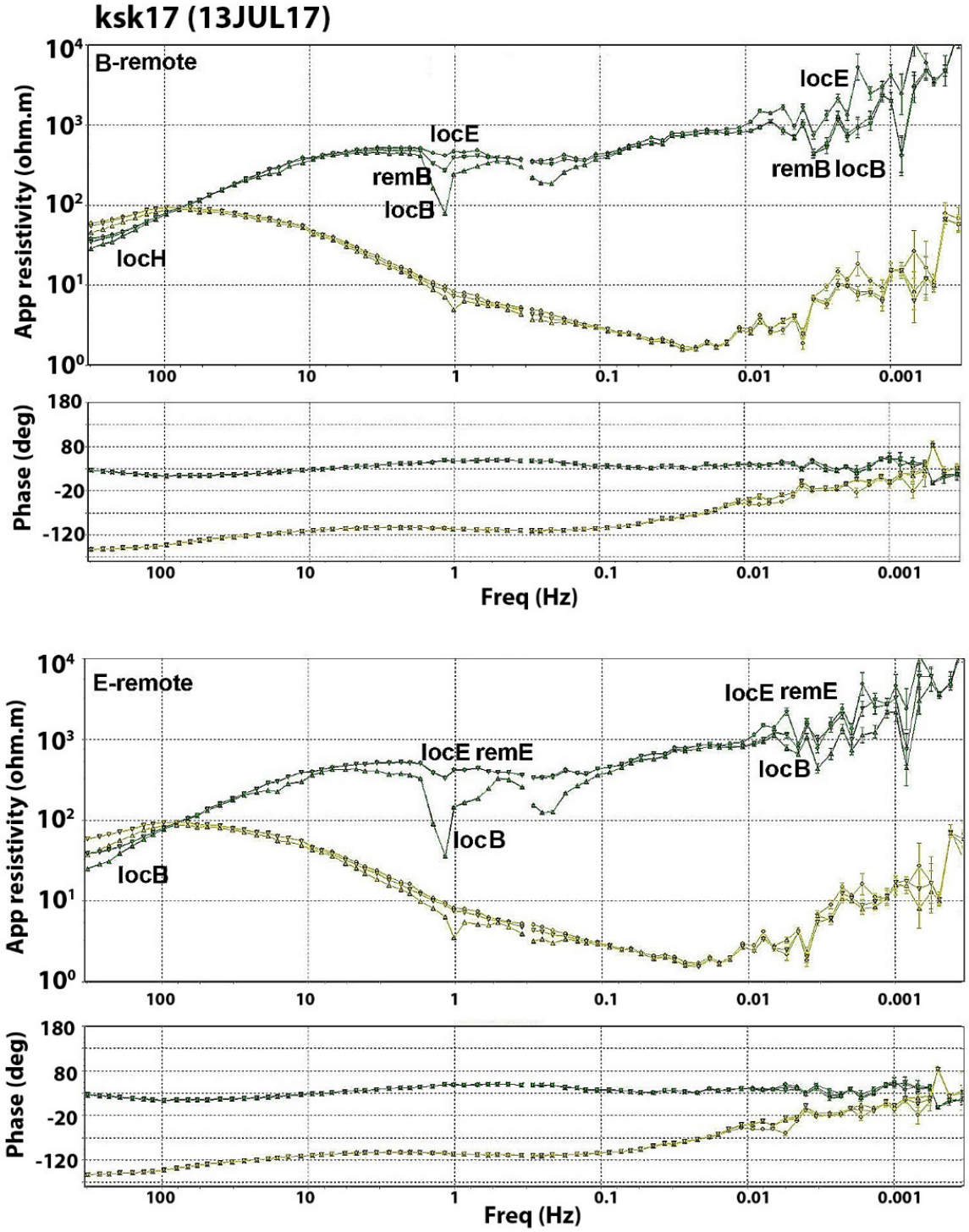

Figure 31. Remote-B and remote-E apparent resistivity and phase responses for ksk17 for deployment on 13JUL17. Responses computed using the full time series (23 hours) and default infield robust processing parameters (see Section 2.2). The colour coding is *xy*-component=green, *yx*-component=yellow.

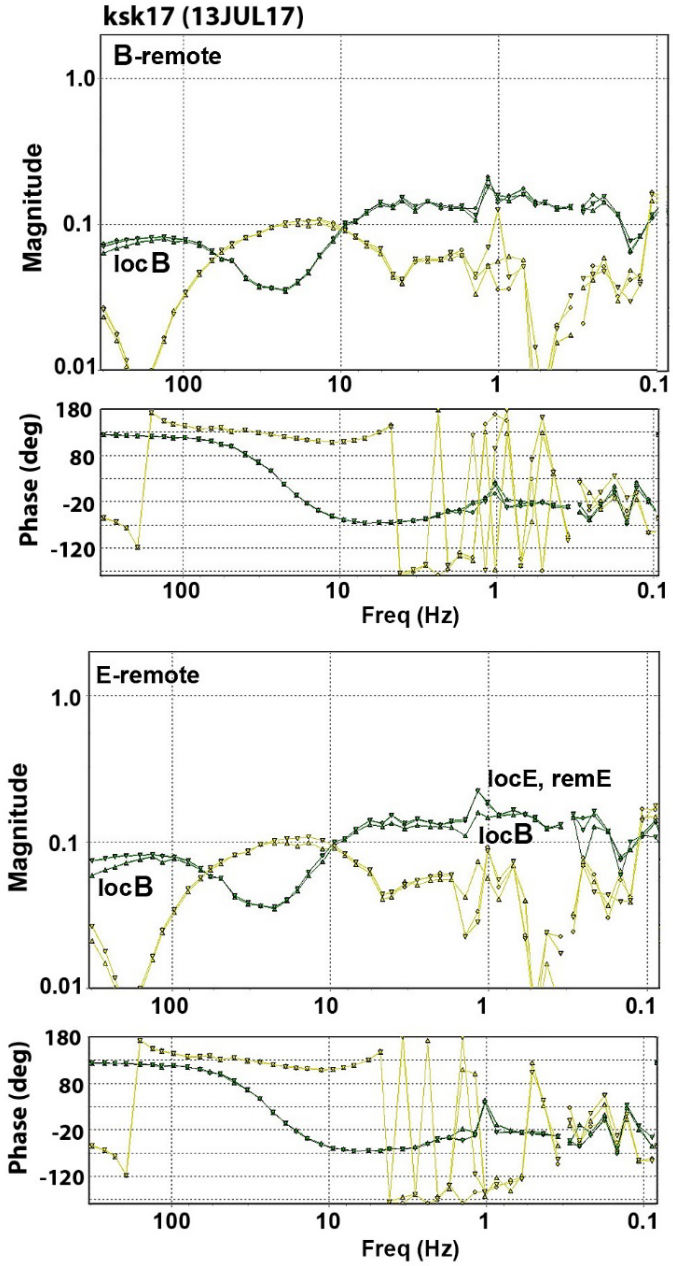

Figure 32. Remote-B and remote-E tipper responses for ksk17 for deployment on 13JUL17. Responses computed using the full time series (23 hours) and default infield robust processing parameters (see Section 2.2). The colour coding is *xy*-component=green, *yx*-component=yellow. The strong change in the phase of the *yx*-component response between 1 and 10 Hz is due to the phase wrapping through 180º.

The impedance phase and tipper phase response is similar for all four remote-B, remote-E, local-B, and local-E responses except at frequencies of <0.003 Hz (periods of >300 s). In the lower frequency (longer period) range there are irregular variations between the phase responses at adjacent frequencies, and there is both irregular variation and minor bias in the apparent resistivity and tipper magnitude responses. In contrast to the irregular low frequency responses, at intermediate frequencies there are some consistent and significant differences in the apparent resistivity and magnitude that can be attributed to the presence of correlated and uncorrelated noise. The main apparent resistivity and tipper magnitude results are as follows:

1. A downwards bias in local-B apparent resistivity and tipper magnitude responses at very high frequencies of >300 Hz (periods of <0.03 s) is not seen in the remote-B, remote-E, or local-E

responses indicating that it is due to uncorrelated noise on the local magnetic field components that is effectively removed in the other estimates.

2. There is downwards bias in local-B *xy*-apparent resistivity and tipper magnitude responses at intermediate frequencies of 0.05-10 Hz (periods of 0.1–20 s) and a weaker bias of the *yx*-apparent resistivity response. These effects are partially removed in the remote-B response, but they are fully removed in the local-E and remote-E responses indicating that the bias is due to both uncorrelated and correlated noise in the magnetic field components. The uncorrelated component is interpreted to be associated with the individual component magnetic field noise (Section 5.2) and the correlated component is interpreted to be due to the broad-band noise originating near GILL (Section 5.1).
3. There is no additional perturbation of responses at 0.5 Hz (~2 s) at the frequency of interpreted pulsations indicating that pulsations do not have a deleterious effect on the MT responses. In fact, the apparent resistivity responses suggest a reduction in the bias in the pulsation period range, relative to stronger bias observed in adjacent period ranges. Such an effect is explained by the higher signal to noise levels caused by the pulsations.
4. There is increased irregularity and significant deviation in all of the responses at lower frequencies (<0.01 Hz) (longer periods, >100 s). The remote-E and remote-B responses are superior to either local-E or local-B responses but the remote responses also show irregularities. The bias of the apparent resistivity can be explained by either correlated noise on corresponding magnetic components, correlated noise on corresponding electric components, or a combination of these effects. Close inspection of the remote-B apparent resistivity responses in Figure 31 shows that there is a significant downturn in the magnitude of the *xy*-component at frequencies between 0.001 and 0.01 Hz (periods between 100 and 100 s) that is not observed in the remote-E response or is associated with a phase-change. This observations suggests the long-period bias may be due to spatially correlated non-uniform magnetic field signals.

Examination of corresponding responses for ksk06 computed for 09JUL17 (not shown), on which stronger signal levels and higher auroral indices were observed, yields similar patterns to those shown here. For that day, the effects of the high frequency uncorrelated noise on the responses was similar to on the quieter day. However, the bias effects at intermediate periods are much less than for the 13JUL17, as expected, because of the higher signal to noise ratio. Also, low frequency bias effects for 09JUL17 are stronger than those on the quieter day.

Overall, the results suggest the use of remote-E estimates provide a response that is less biased by correlated artificial magnetic field noise than the remote-B response. The observations also suggest there is a stronger effect of non-uniform magnetic field auroral signals on the MT responses relative to the effect of non-uniform electric field auroral signals. This result may be explained by the fact that short-wavelength field components bias impedance magnitude downwards (e.g., Mareschal, 1986; Jones & Spratt, 2002). As the electric field is proportional to the impedance, shorter wavelengths will make a disproportionately smaller contribution to the total electric field than to the total magnetic field. Short wavelength sources can also cause upwards bias in the impedance phase (Mareschal, 1986; Jones & Spratt, 2002) but this effect is not discerned in the data set.

6.2 Daytime versus nighttime responses

Figure 33 and 34 compare spectra and apparent resistivity/phase responses for ksk06 for four-hour windows. The spectra show high-frequency B_z noise throughout the recording and pulsation signals in the afternoon window. The afternoon and early-morning windows 20:00–00:00 UT (15:00–19:00 CDST) and 08:00–12:00 UT (03:00–07:00) produce the best unedited MT responses at low frequencies (long periods) with reasonably smooth responses at frequencies as short as 0.003 Hz (periods as long as 300 s). In contrast, the early- and late-night responses 00:00–04:00 UT (19:00–23:00 CDST) and 04:00–08:00 (23:00–03:00 CDST) are noisy at frequencies less than 0.02 Hz (periods longer than about 50 s).

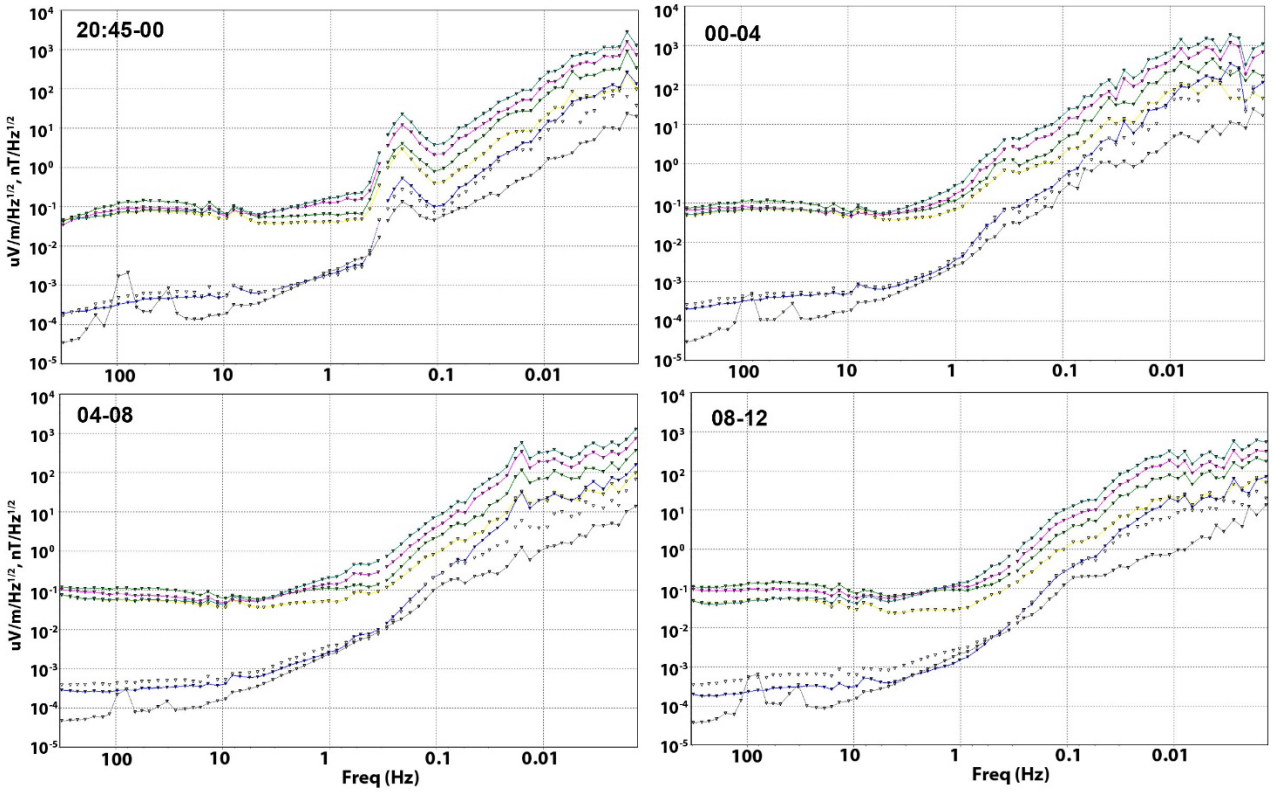

Figure 33. Spectra for ksk06 for 4 hour windows from 20:00 UT 09JUL17–12:00 UT 10JUL17.

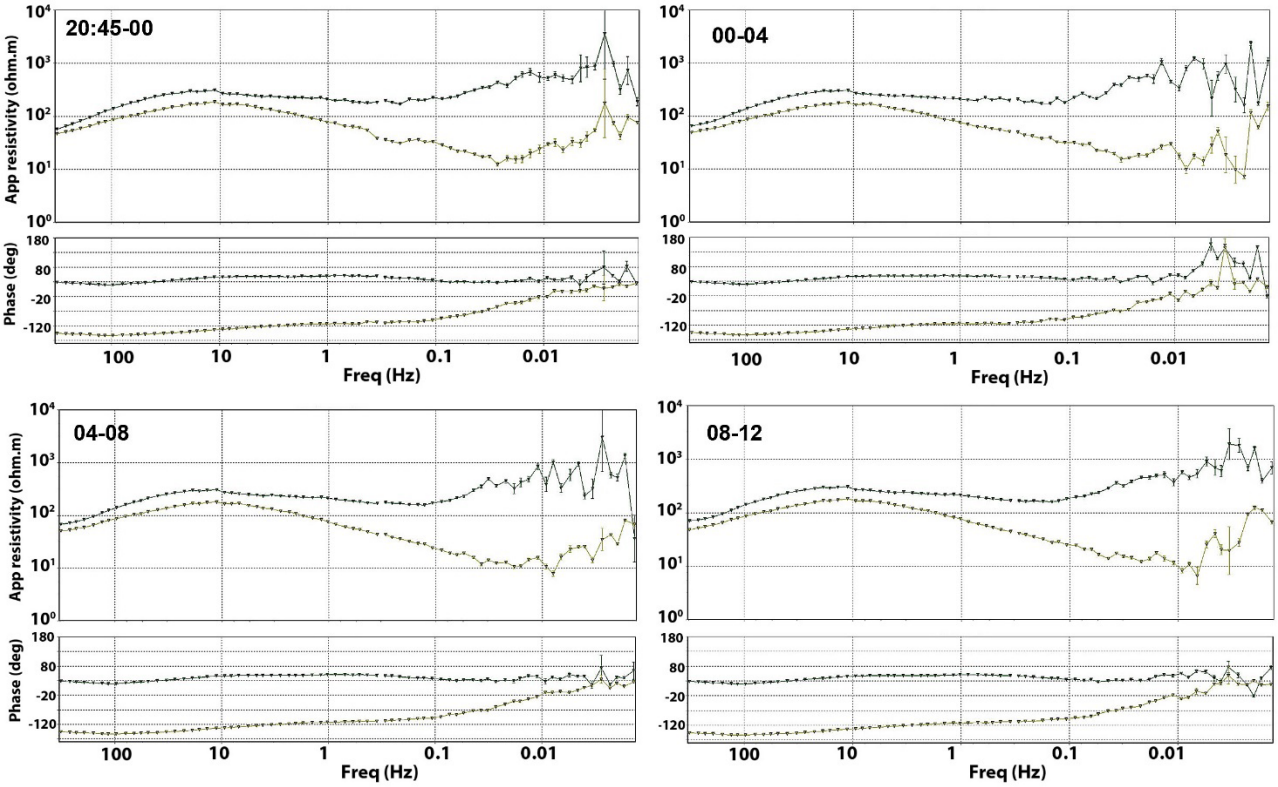

Figure 34. Unedited apparent resistivity and phase responses for ksk06 for 4 hour windows from 20:00 UT 09JUL17–12:00 UT 10JUL17. Results are for remote-E calculations with ksk07 as the remote reference.

Figures 35 and 36 show the corresponding results from a quieter period for ksk17. The spectra show the high frequency B_z noise throughout the recording, magnetic field noise at ~1 Hz frequency (1 s period), and pulsation signals in the early-morning window. The afternoon and early-morning windows 20:00–00:00 UT (15:00–19:00 CDST) and 08:00–12:00 UT (03:00–07:00) produce the best unedited MT responses at low frequencies in the range 0.03-0.003 Hz (30–300 s), but are significantly affected by the intermediate frequency range noise. In contrast, the early- and late-night responses, 00:00–04:00 UT (19:00–23:00 CDST) and 04:00-08:00 UT (23:00-03:00 CDST), provide good responses at intermediate frequencies but are relatively noisy at frequencies less than 0.02 Hz (periods longer than 50 s).

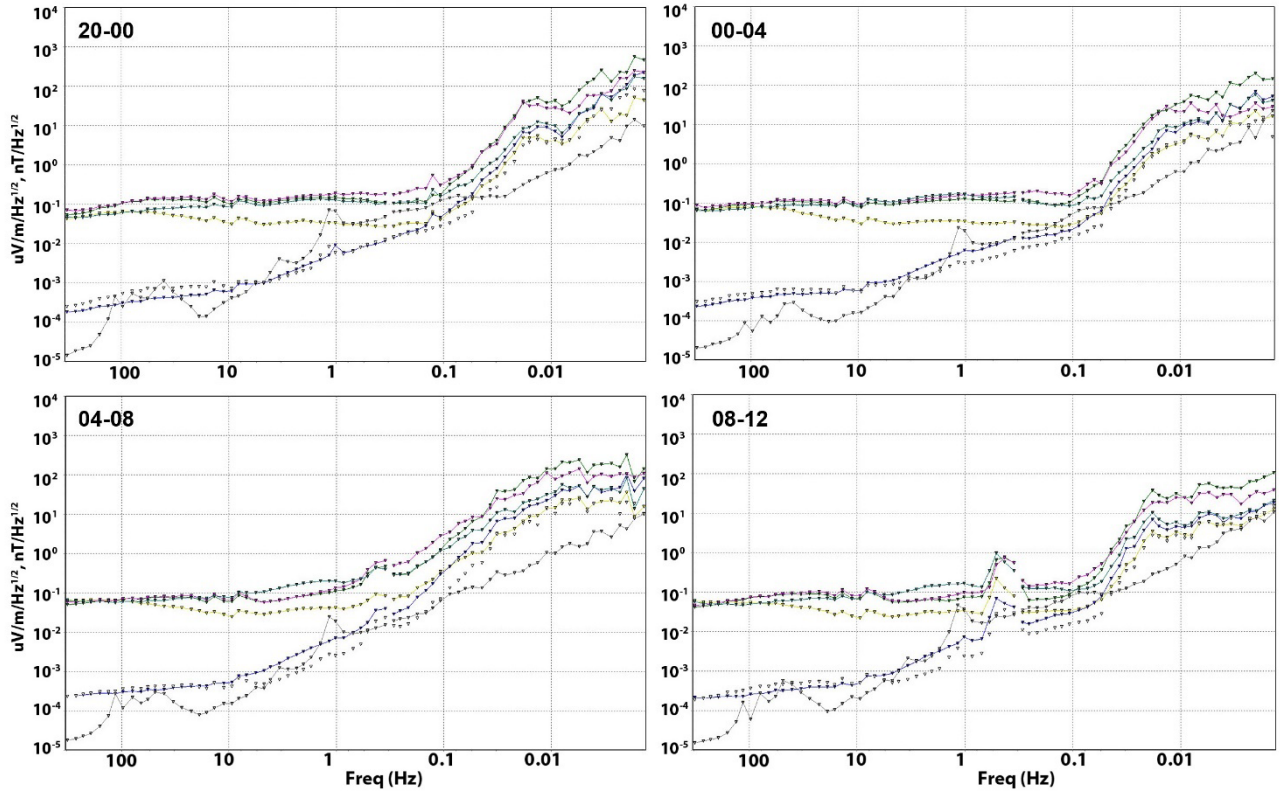

Figure 35. Spectra for ksk17 for 4 hour windows from 20:00 UT 13JUL17–12:00 UT 14JUL17.

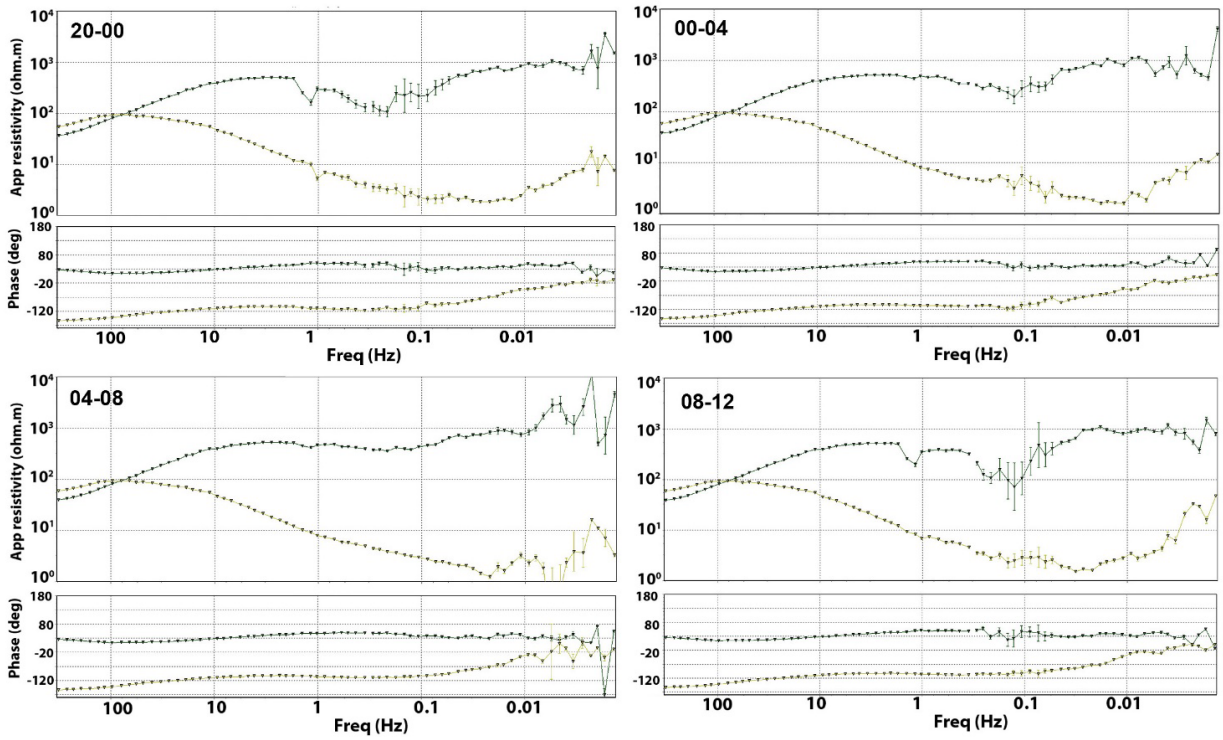

Figure 36. Unedited apparent resistivity and phase responses for ksk17 for 4-hour windows from 20:00 UT 13JUL17–12:00 UT 14JUL17. Results are for remote-E calculations with ksk18 as the remote reference.

6.3 Effect of robust processing parameters

Next, the effect of varying robust parameters will be examined using data from 09JUL17 recordings at ksk06 and 13JUL17 recordings from ksk13 as representative times and sites. Firstly, Figures 37 and 38 show the effects of varying the weighting of the 20 time-series intervals used in the stack. The methods used include no weighting, weighting by rho variance, and weighting by ordinary coherence between E and B channels. There is little difference in the three responses for the methods for either the more active or quite day. Figure 38 shows that either rho variance or correlation weighting produces a slightly better response than no weighting in terms of removing the effects of noise at intermediate frequency (see the rho_{xy} response at frequencies just above 1 Hz). However, the results reveal very little difference in the response at periods affected by the auroral signals.

Figures 39 and 40 compare the main two-component coherence weighting methods available in the Phoenix software. The methods are based on either multiple coherence or partial coherence calculations and either the local magnetic field and the remote reference or the local electric field and the local magnetic field. There is very little difference in the four responses for either the more active or quiet day. Overall, the default method, based on the multiple coherence between the local magnetic field and remote reference components provides a slightly superior response at low frequencies. The only other point of note is that Method 1 yields some downward bias of low-frequency rho_{xy} amplitude responses for the quieter day (Figure 40).

For the final comparison, tests were done using a range of values for the rho variance and coherence cut-off along with the maximum fractions of estimates to reject (Figures 41, 42). Results were examined for tighter parameters (higher minimum cut-off and larger maximum rejection fraction) intended to require exclusion of more estimates and for more liberal parameters (lower minimum cut-off and small maximum rejection fraction) intended to require inclusion of a larger fraction of estimates. The four sets of results produced almost identical estimates for the more active period (ksk06 on 09–10JUL17). For the quieter period (ksk17 on 13–14JUL17) the best results at intermediate frequencies

were obtained for the more liberal rho variance weighting and the noisiest results at low frequencies were obtained for the tight coherence weighting.

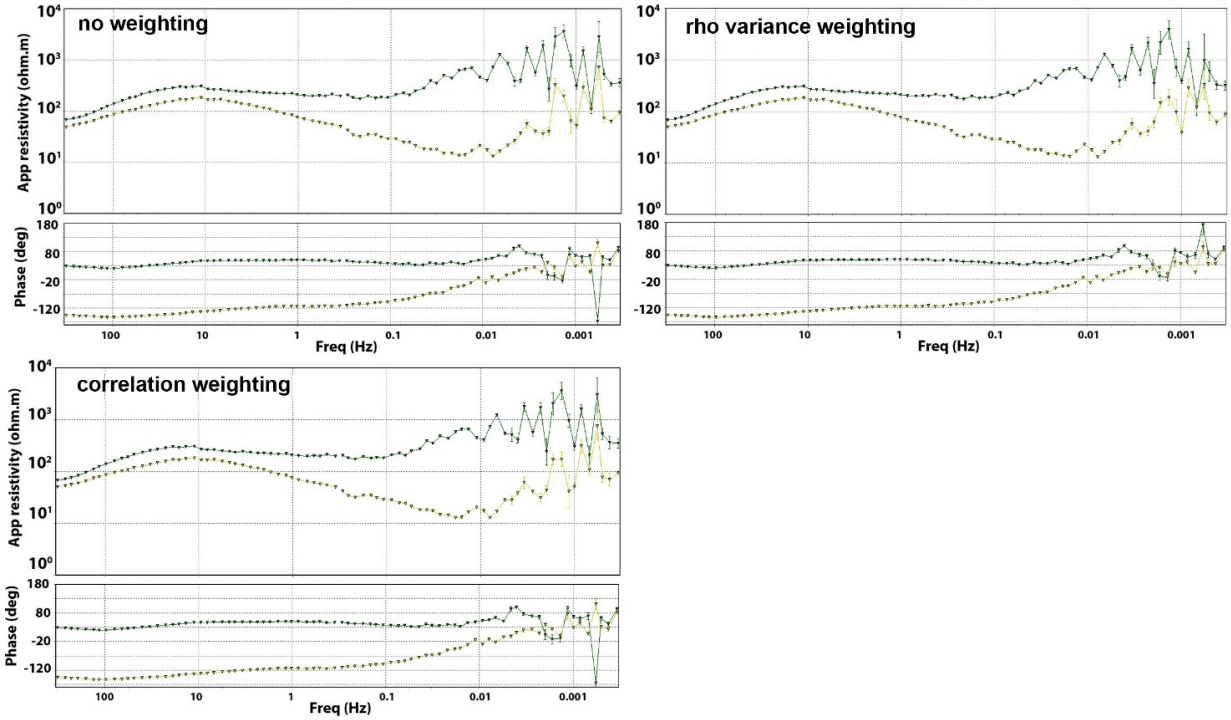

Figure 37. Examination of the effects of different methods of weighting for the estimates from individual time series segments for ksk06 on 09–10JUL17. Results are for the unedited remote-E response with ksk07 as the remote-reference. The other robust processing parameters were set to default values.

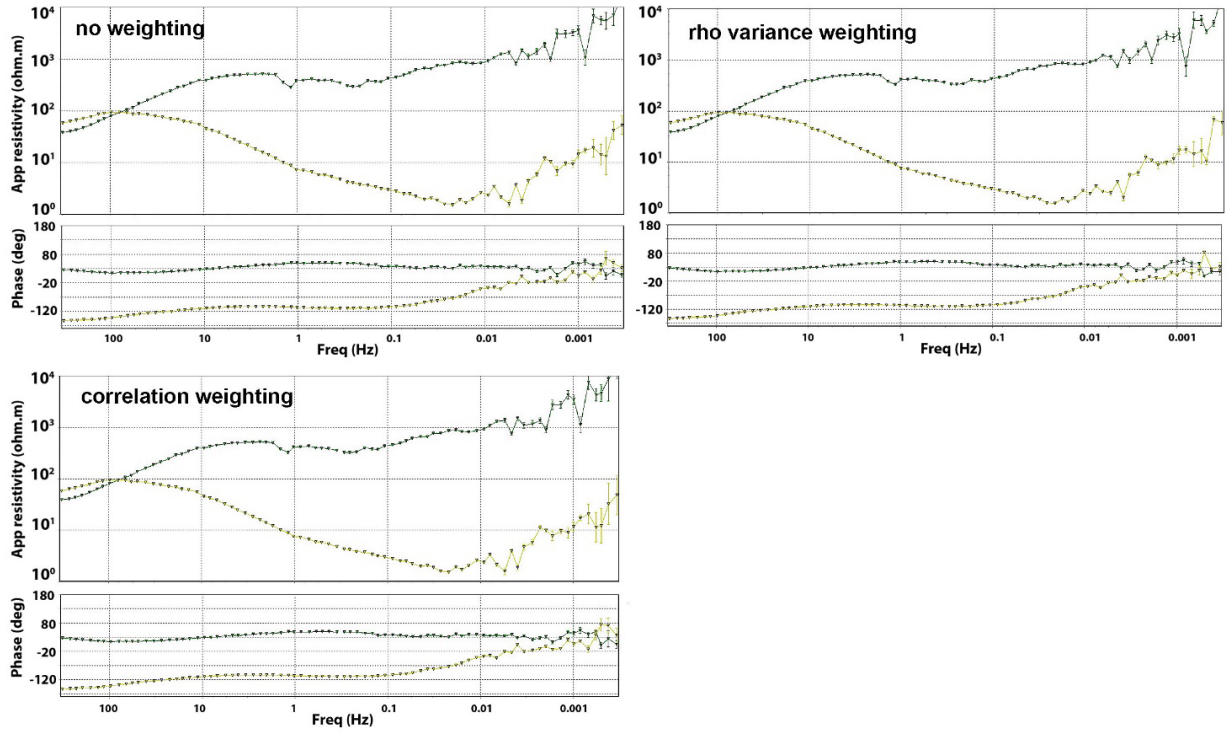

Figure 38. Examination of the effects of different methods of weighting for the estimates from individual time series segments for ksk17 on 13–14JUL17. Results are for the unedited remote-E response with ksk18 as the remote-reference. The other robust processing parameters were set to default values. Note the slightly larger deflection of the rho$_{xy}$ response at periods just less than 1 s for the case with no weighting.

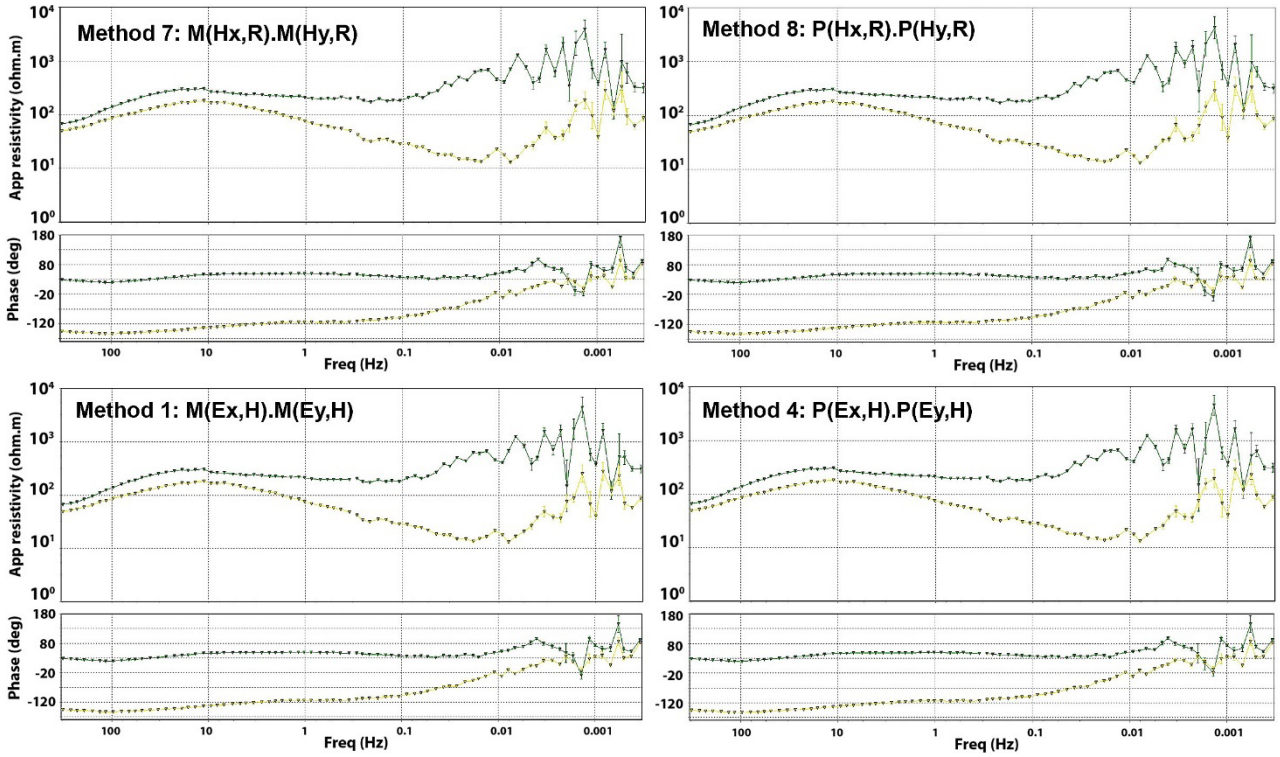

Figure 39. Examination of the effects of different methods of coherence weighting for ksk06 on 09–10JUL17. Results are for the unedited remote-E response with ksk07 as the remote-reference. The other robust processing parameters were set to default values. Compare deflection of rho$_{xy}$ response at periods of 100–1000 s.

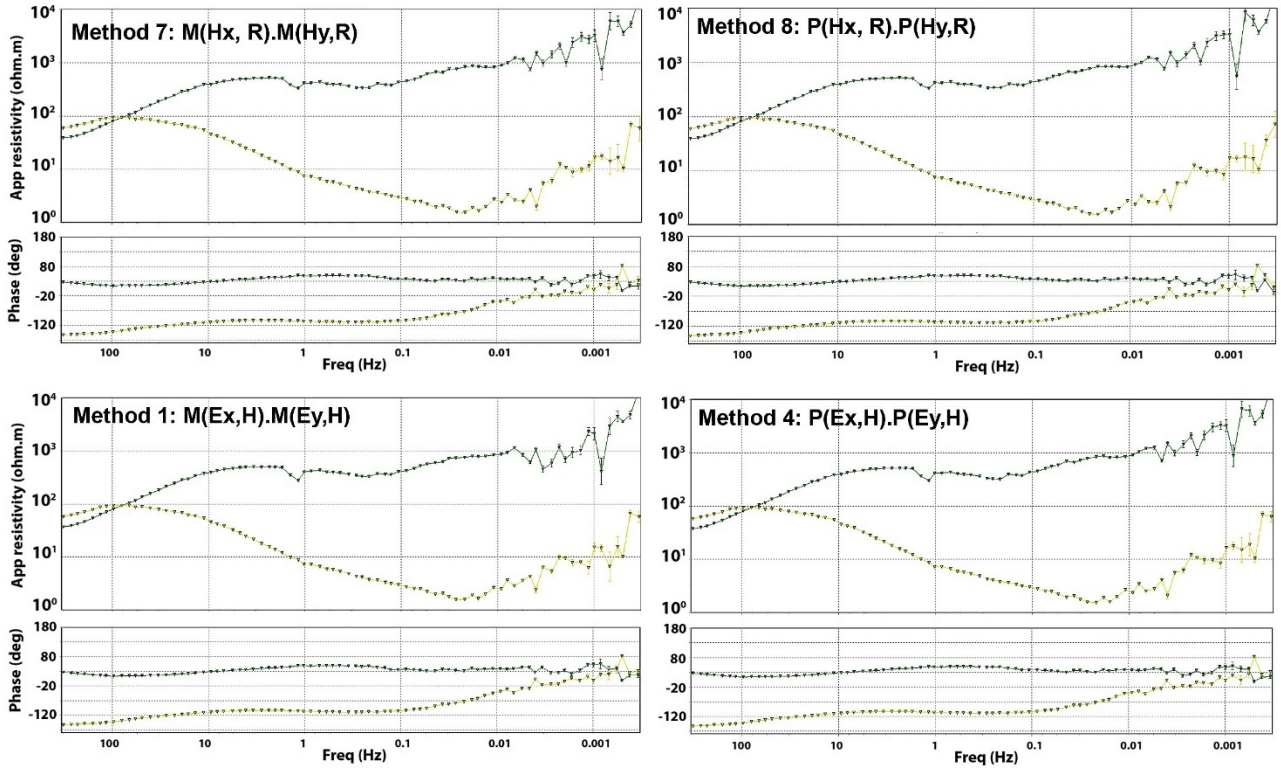

Figure 40. Examination of the effects of different methods of coherence weighting for the estimates for ksk17 on 13–14JUL17. Results are for the unedited remote-E response with ksk18 as the remote-reference. The other robust processing parameters were set to default values. Note the different deflection of the rho$_{xy}$ response at periods just greater than 1000 s.

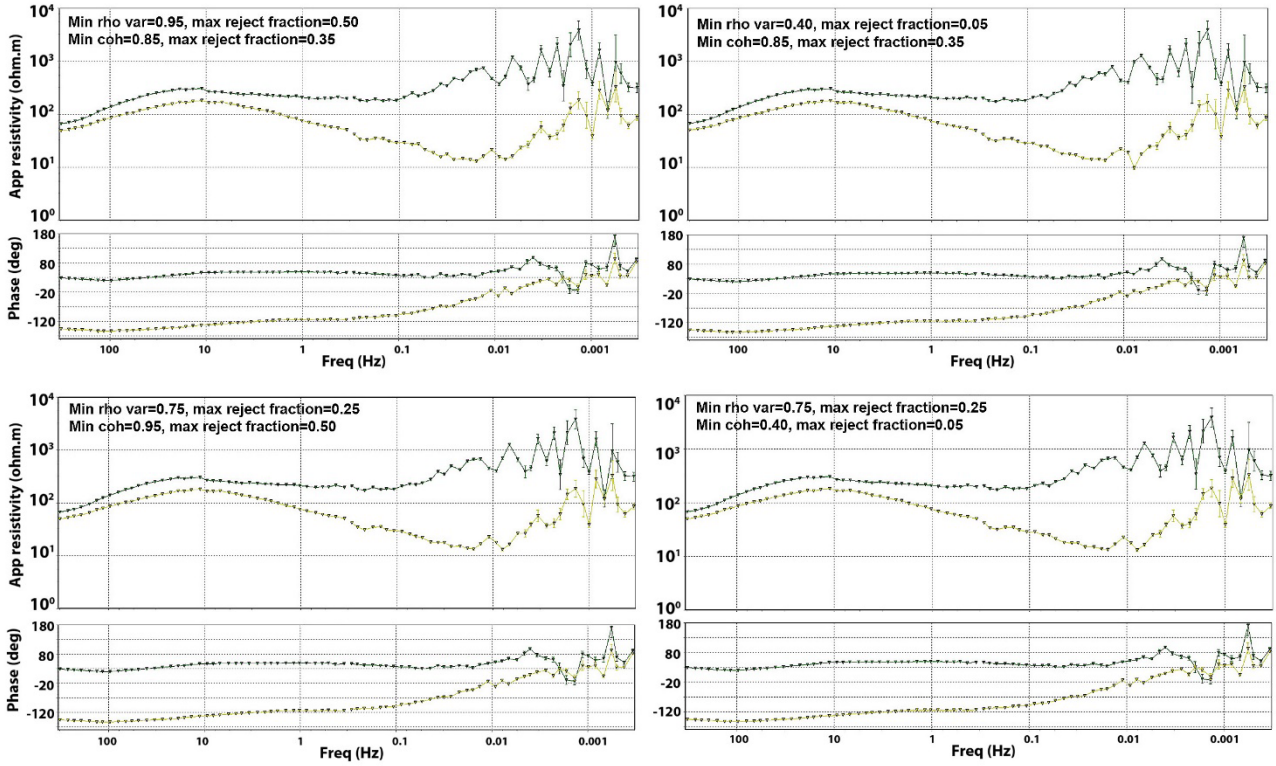

Figure 41. Examination of the effects of different rho variance and coherence parameters for ksk06 on 09–10JUL17. Results are for the unedited remote-E response with ksk07 as the remote-reference. The other robust processing parameters were set to default values.

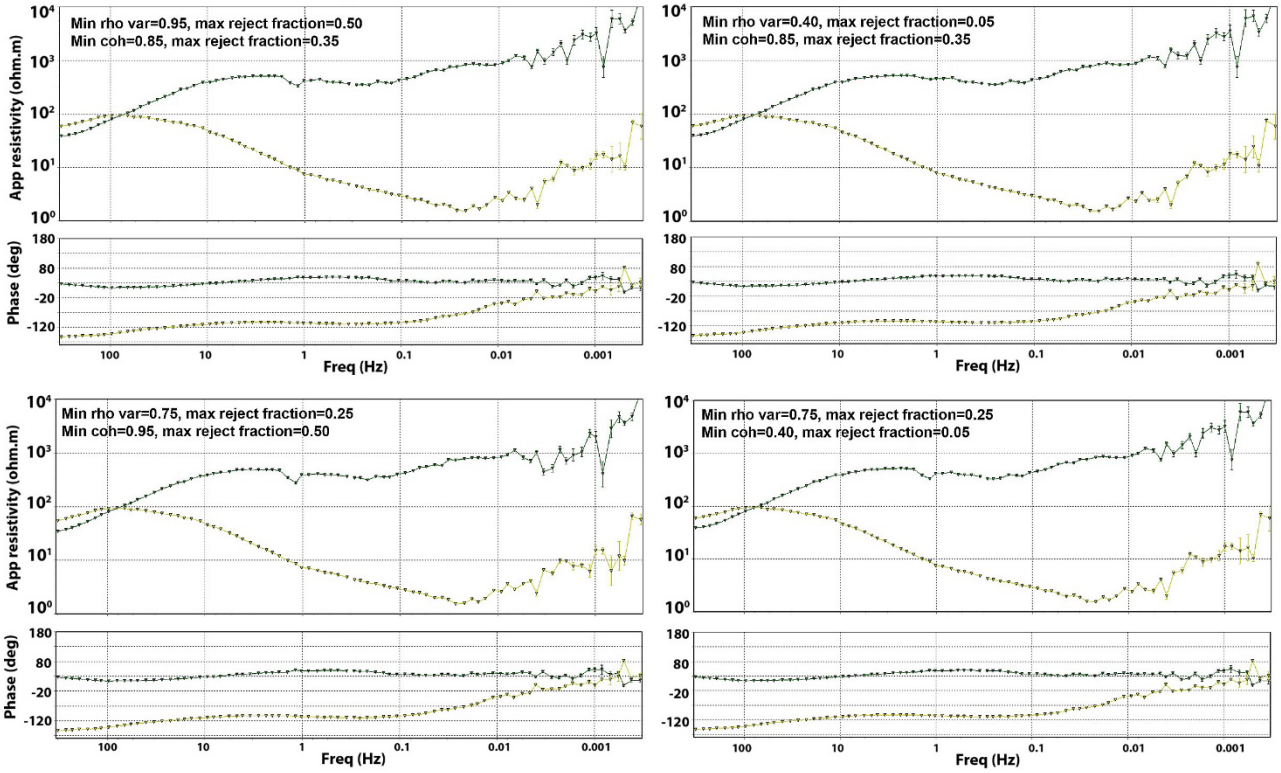

Figure 42. Examination of the effects of different rho variance and coherence parameters for ksk17 on 13–14JUL17. Results are for the unedited remote-E response with ksk18 as the remote-reference. The other robust processing parameters were set to default values. Note the smaller deflection of the rho$_{xy}$ response at periods of just less than 1 s for the case with more liberal rho variance weighting.

6.4 Summary of data processing results

The testing of the data processing parameters showed that overall the choice of the type of remote reference and the time duration of the analysis had the greatest impact on the results. For the subset of the KSK data set that as examined, the remote-E estimate is the most reliable because of the smaller effect of inter-site correlated noise compared with the effect in remote-B estimate. For responses from the mid-frequency range (~1 Hz), estimates from nighttime records provide superior responses that are less affected by broad-band noise effects. In contrast, for low frequency results (<0.02 Hz) (periods >50 s), estimates from the daytime records provide superior responses that are less affected by non-uniform auroral signals. In subsequent processing of the KSK MT data set, the choice of recording duration can be addressed through the crosspower editing phase.

The choice of robust processing parameters had a much smaller effect on the MT responses for the KSK data set. In general, the optimal method for the records tested appear to be to use rho variance weighting in the stacking, coherence weighting based on multiple coherence between the local magnetic field and remote reference, and the default coherence cut-offs with fairly liberal rho-variance cut-offs. With the exception of the last aspect, these parameters are very close to the default values in the Phoenix software. Given the similarity of responses for the different processing parameters, it appears reasonable to simply use the default values in subsequent processing.

7. Final data reprocessing

The KSK MT data set was fully reprocessed (starting from the recorded ts files) based on the information obtained above. The primary approaches used in the re-processing were:

1. Use of remote-E estimates wherever possible, choosing the closest reference site providing a full overlap, and
2. Careful truncation time-series included in the processing to cut out noise associated with site disturbances including electrode re-installation, site pack-up, helicopter noise, and animal disturbances.
3. Careful editing of responses in the **MTEDITOR** from the shortest period to at least 1000 s period.

Spectra associated with each remote-reference data set were checked for unexpected forms of noise. Table 3 lists the main parameters of the reprocessing for each of the sites. For site ksk01 the MT part of the response was processed using remote-E processing and the AMT part of the response using local-E processing. For site ksk08 the response was processed using local-B processing. The remote-E (and mixed) output edi files were named **ksk*nn*e.edi** and the local processed file **ksk*nn*l.edi**. An electronic appendix containing the individual edi files is available as part of this report (Appendix 1).

For the remote-E responses, the **MTEDITOR** editing was generally straightforward from the highest frequency down to 0.1 Hz (periods less than 10 s). At most sites the editing required removing daytime responses at the highest frequencies (>300 s) (periods of <0.003 s) and in the MT deadband (~1 Hz frqeuency or 1 s period). The editing was typically more difficult at lower frequencies (longer periods) with reliable results obtained to frequencies periods ranging from about 0.03 Hz (period of 30 s) at some strongly anisotropic sites (e.g., ksk07, ksk08) to <0.003 Hz (periods of at least 300 s) at the highest quality sites (e.g., ksk15, ksk19). Overall, the reprocessing typically added one-half to one decade of useful responses compared with the earlier in-field and remote-B processing.

Figure 41 compares the reprocessed remote-E response with the previously calculated remote-B response (from N. Clark) for sites ksk06 and ksk17. The improvements are fairly subtle. For ksk06, good quality apparent resistivity responses are extended by the reprocessing from 100 s to 300 s and reasonable phase responses from 200 to 400 s. The error estimates are larger on the reprocessed data, probably reflecting the more critical editing of the reprocessed data set, but provide an improved estimate of the actual uncertainty in the data. For ksk17, a geomagnetically quieter day, the reprocessing has extended good quality phase responses from 300 s to 1000 s. The effects of the reprocessing were

examined in terms of pseudosection responses but these responses did not show the improvement very clearly.

Table 3. Details of the reprocessing of the KSK MT data sets

Site	Recording start dates (July 2017)	Configuration	Remote site	Comments
ksk01	07,08,09	MT – Rem E AMT – Local E	ksk02	AMT processing used dummy duplicate site to yield pseudo rem-E
ksk02	07,08,09	Rem E	ksk01, ksk06	
ksk03	08	Rem E	ksk04	
ksk04	08	Rem E	ksk03	
ksk05	08	Rem E	ksk02	
ksk06	09	Rem E	ksk07	
ksk07	09	Rem E	ksk06	
ksk08	09	Local B	-	H-samp setting was different from other simultaneously recording sites.
ksk09	10,11	Rem E	ksk10,ksk11	
ksk10	10	Rem E	ksk09	
ksk11	11	Rem E	ksk12	
ksk12	11	Rem E	ksk11	
ksk13	11	Rem E	ksk12	
ksk14	12	Rem E	ksk15	
ksk15	12	Rem E	ksk14	
ksk16	12	Rem E	ksk14	
ksk17	13	Rem E	ksk18	
ksk18	13	Rem E	ksk17	
ksk19	13	Rem E	ksk17	B_x, B_y imported from ksk018. No B_z.
ksk20	14	Rem E	ksk21	
ksk21	14	Rem E	ksk20	
ksk22	14	Rem E	ksk20	Processing shortened due to coil unburial by animal.

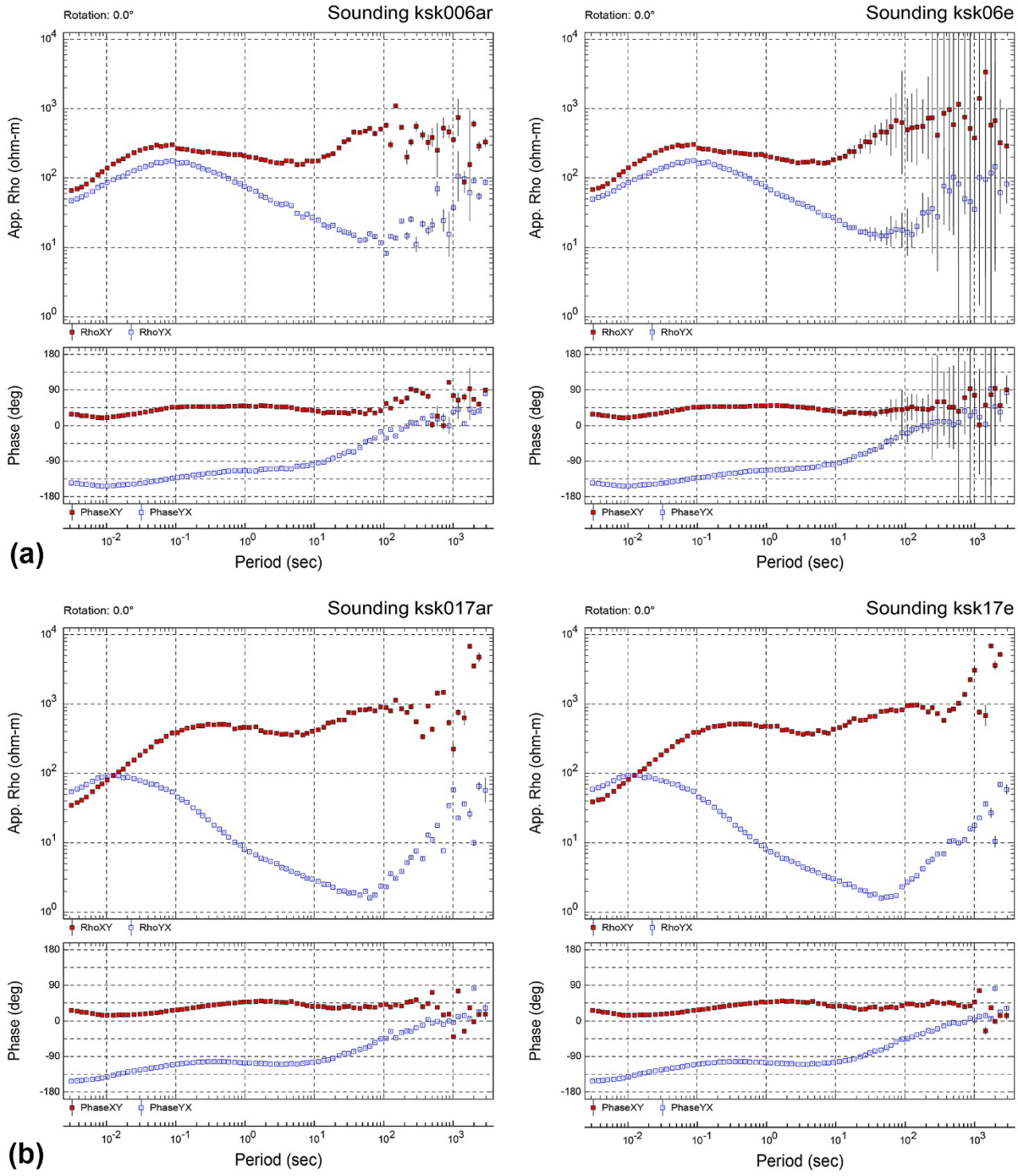

Figure 43. Comparison of initial MT responses based on remote-B processing (left) and final MT responses based on remote-E processing (right) for (a) ksk06 and (b) ksk17.

8. Conclusions

The 2017 Kaskattama Highland MT dataset was collected during a quiet geomagnetic period (mostly with Kp indices of <4) during which time only one minor storm occurred. The high geomagnetic latitude of the survey, 65º N, resulted in the data containing strong Pc1 pulsation and auroral signals. The survey area is within 250 km of hydroelectric facilities in the Gillam area and strong sources of artificial electromagnetic noise. As a result of these factors, initial computation of MT responses using

standard processing steps, such as a magnetic field remote-reference, yielded MT responses of only moderate quality. Very poor long-period responses (for periods >30–100 s) can be attributed to auroral electrojet signals. These effects are most pronounced at times of low magnetospheric signal levels.

The relatively complicated mix of signal and noise in the KSK MT dataset was examined using the MT data and geomagnetic recordings from CARISMA stations at Gillam, Churchill, and Rabbit Lake. Methods used for separating the signal and noise in space, time, and frequency included examination of time-series, spectra, and spectrograms; examination of MT responses for different remote-references including magnetic and electric field recordings; examination of MT responses as a function of recording time; and examination of MT responses for different robust processing parameters.

There were a number of types of noise identified in the KSK and CARISMA recordings. Two main forms of electromagnetic noise were observed at Gillam and are interpreted to be related to hydroelectric infrastructure in the Gillam area

1. A time-varying broad-band noise present on all three magnetic components at the Gillam CARISMA station.
2. Narrow band noise centred on 4.8 s period and present most strongly on the B_x and B_z components at the Gillam CARISMA station.

The first form of noise was also recorded in the KSK horizontal magnetic field data at locations, 240 km away from Gillam. It contributes to significant bias of MT and tipper responses at periods of 0.1–20 s calculated using local fields only, and to weaker bias of corresponding responses calculated using a magnetic-field remote reference from the KSK area. The use of remote reference electric fields removes this bias.

There were several addition forms of noise recognized in the KSK MT data. Spike-like events occurring sporadically in individual magnetic field recordings caused spatially-localized broad-band noise. This effects of this noise on MT responses was effectively removed using either magnetic or electric-field remote-reference processing. Pc1 pulsations did not appear to cause significant bias in any of the MT responses and the higher signal levels during their occurrence improved the signal to noise ratio.

Finally, it was confirmed that the noisy MT responses at long-periods were caused by auroral electrojet signals. These signals are highly spatially heterogeneous in both geomagnetic longitude and latitude at scales are small as several hundred kilometres. The effect of the auroral signals was most effectively reduced by computation of MT responses with remote-reference electric fields. Additional improvement of the long-period response was possible with consideration of day-time recordings only, but the day-time was more problematic for other forms of electromagnetic noise. Changing the parameters of robust spectral calculations in the Phoenix **SSMT** processing software had minimal effect on the responses.

The complete set of MT responses for the KSK survey was recomputed using the full length of recordings available at each site and using remote-reference electric fields. This reprocessing removed local bias at intermediate periods caused by the spatially-corrected magnetic field noise and added about one-half a decade of improved responses at the longest periods.

Acknowledgements

The KSK MT data collection was facilitated by Custom Helicopter personnel, who provided safe transport to the field sites; B. Giroux from Institut Nationale de la Recherche Scientifique (INRS), who loaned us an INRS set of MTU's; N. Brandson of the Manitoba Geological Survey, who provided reliable logistical support, and G. Buller of Natural Resources Canada, who provided GIS support. We are grateful to CARISMA for permission to use data and figures from that program. The authors also thank SeyedMasoud Ansari for his helpful review of this report.

References

Boteler, D.H. and Pirjola, R.J., 1998. The complex-image method for calculating the magnetic and electric fields produced at the surface of the Earth by the auroral electrojet; Geophysical Journal International, v. 132, p. 31-40.

Campbell, W.H., 1976. An analysis of the spectra of geomagnetic variations having periods from 5 min to 4 hours; Journal of Geophysical Research, v. 81, p.1369-1390.

Campbell, W.H., 2003. Introduction to Geomagnetic Fields. Cambridge University Press, 290 p.

Chave, A.D. 2012. Estimation of the magnetotelluric response function; Chapter 5 *in* The magnetotelluric method: Theory and practice, (Eds.) Chave A.D., and Jones, A.G., Cambridge University Press, p. 165-218.

Chave, A.D. and Thomson, D.J., 1989. Some comments on magnetotelluric response function estimation; Journal of Geophysical Research, v. 94, p. 14215-14225.

Chave, A.D. and Thomson, D.J., 2003. A bounded influence regression estimator based on the statistics of the hat matrix; Journal of the Royal Statistical Society: Series C (Applied Statistics), v. 52, p. 307-322.

Chave, A.D. and Thomson, D.J., 2004. Bounded influence magnetotelluric response function estimation; Geophysical Journal International, v. 157, p. 988-1006.

Chave, A.D., D.J. Thomson and M.E. Ander, 1987. On the robust estimation of power spectra, coherencies, and transfer functions; Journal of Geophysical Research, v. 92, p. 633-648.

Clark, N., 2017. Magnetotelluric Survey of the Kaskattama Highland, Northeastern Manitoba; Technical Report submitted to the Geological Survey of Canada, GEM2 Hudson Ungava project, 38 p.

Constable, C., 2016. Earth's electromagnetic environment; Surveys in Geophysics, v. 37, p. 27–45.

Craven, J.A., Ferguson, I.J., Nicolas, M.P.B., Zaprozan, T., Hodder, T., Roberts, B.R., and Clark, N., 2017. Report of activities for the ground geophysical survey across the Kaskattama highlands, Manitoba: GEM-2 HudsonUngava Project; Geological Survey of Canada, Open File 8321, 30 p.

Craven, J.A., Ferguson, I.J. and Roberts, B.J., 2018. Ground geophysics in the Hudson Bay area, Nunavut: GEM-2 Kaskattama highlands and Southampton Island Project; *in* Report of Activities 2018. Geological Survey of Canada, Open File 8487, 10 p.

Davis, T.N. and Sugiura, M., 1966. Auroral electrojet activity index AE and its universal time variations; Journal of Geophysical Research, v. 71, p. 785-801.

Egbert, G.D., 2002. Processing and interpretation of electromagnetic induction array data. Surveys in Geophysics, v. 23, p. 207-249.

Egbert, G.D. and J.R. Booker, 1986. Robust estimation of geomagnetic transfer functions; Geophysical Journal of the Royal Astronomical Society, v. 87, p. 173-194.

Egbert, G.D. and Booker, J.R., 1989. Multivariate analysis of geomagnetic array data. 1. The response space; Journal of Geophysical Research, v. 94, p. 14227–14247.

Egbert, G.D. and Livelybrooks, D.W. 1996. Single station magnetotelluric impedance estimation: coherence weighting and the regression M-estimate; Geophysics, v. 61, p. 964-970.

Escalas, M., Queralt, P., Ledo, J. and Marcuello, A., 2013. Polarisation analysis of magnetotelluric time series using a wavelet-based scheme: a method for detection and characterisation of cultural noise sources; Physics of the Earth and Planetary Interiors, v. 218, p. 31-50.

Ferguson, I.J., 2012. Instrumentation and Field Procedure; Chapter 9 *in* The Magnetotelluric Method: Theory and Practice; (Eds.) Chave, A.D., and Jones, A.G., Cambridge University Press, p. 421-479.

Ferguson, I.J., Craven, J.A, Kurtz, R.D., Boerner, D.E. Bailey, R.C., Wu, X., Orellana, M.R., Spratt, J., Wennberg, G. and Norton, M. 2005. Geoelectric responses of Archean lithosphere in the western Superior Province, central Canada; Physics of the Earth and Planetary Interiors, v. 150, p. 123–143.

Gamble, T.D., Goubau, W.M. and Clarke, J., 1979a. Magnetotellurics with a remote magnetic reference. Geophysics, v. 44, p. 53-68.

Gamble, T.D., Goubau, W.M. and Clarke, J., 1979b. Error analysis for remote reference magnetotellurics; Geophysics, 44, 959-968.

Garcia, X., Chave, A.D. and Jones, A.G., 1997. Robust processing of magnetotelluric data from the auroral zone; Journal of Geomagnetism and Geoelectricity, v. 49, p. 1451–1468.

Ghosh, A., Biswas, D., Hazra, P., Guha, G. and De, S.S., 2019. Studies on Schumann resonance phenomena and some recent advancements; Geomagnetism and Aeronomy, v. 59, p. 980-994.

Goldak Airborne Surveys, 2005. Technical report on a fixed wing aeromagnetic survey, Permit 125b and Permit 136b Blocks, Northeastern Manitoba; For Foran Mining Corporation by Goldak Airborne Surveys. 22 p.

Hughes, T.J. and Rostoker, G., 1977. Current flow in the magnetosphere and ionosphere during periods of moderate activity; Journal of Geophysical Research, v. 82, 2271-2282.

Jones, A.G., 1980. Geomagnetic induction studies in Scandinavia – I. Determination of the inductive response function from the magnetometer data; Journal of Geophysics, v. 48, p. 181–194.

Jones, A.G., Chave, A.D., Egbert, G., Auld, D. and Bahr, K., 1989 A comparison of techniques for magnetotelluric response function estimation; Journal of Geophysical Research, v. 94, p. 14,201–14,213.

Jones, A.G., Olafsdottir, B. and Tiikkainen, J., 1983. Geomagnetic induction studies in Scandinavia. III Magnetotelluric observations; Journal of Geophysics Zeitschrift Geophysik, 54, 35-50.

Jones, A.G. and Spratt, J., 2002. A simple method for deriving the uniform MT responses in auroral zones; Earth Planets and Space, v. 54, p. 443–450.

Junge, A., 1996. Characterization of and correction for cultural noise; Surveys in Geophysics, v. 17, p. 361-391.

Kamide, Y., 1982. The relationship between field-aligned currents and the auroral electrojets: A review; Space Science Reviews, v. 31, p. 127–243.

Larsen, J.C., 1989. Transfer functions: smooth robust estimates by least-squares and remote reference methods; Geophysical Journal, v. 99, p. 645-663.

Larsen, J.C., Mackie, R.L., Manzella, A., Fiordelisi, A. and Rieven, S., 1996. Robust smooth magnetotelluric transfer functions; Geophysical Journal International, v. 124, p. 801-819.

Lavoie, D., Armstrong. D., Nicolas, M.P.B., Zhang, S., Pinet, N., Reyes, J., Beauchemin, M., Decker, V., Castagner, A., Desrochers, A., and Galloway, J.M., 2016. Report of Activities for the GEM-2 Hudson Bay Basin project: stratigraphy, source rock, and RADARSAT research, Nunavut, Manitoba, and Ontario GEM—2 Hudson-Ungava project. Geological Survey of Canada, Open File 8126, 195 p.

Lavoie, D., Nicolas, M.P.B., Armstrong, D., Ardakani, O.H., Jiang, C., Reyes, J., Dhillon, R.S., Savard, M.M., Pinet, N., Brake, V.I., Duchesne, M.J., Beauchemin, M., and Tolszczuk-Leclerc, S. 2017. Report of activities for the 2017 GEM-2 Hudson Bay–Ungava project: stratigraphy, source rock, and RADARSAT-Research, Nunavut, Manitoba, and Ontario, Open File 8319, Geological Survey of Canada, 24 p.

Lezaeta, P., Chave, A., Jones, A.G. and Evans, R., 2007. Source field effects in the auroral zone: Evidence from the Slave craton (NW Canada); Physics of the Earth and Planetary Interiors, v. 164, p. 21-35.

McLeod, J., Ferguson, I.J., Craven, J.A., Roberts, B., & Giroux, B., 2018. Pre-injection magnetotelluric surveys at the Aquistore CO_2 sequestration site, Estevan, Saskatchewan, Canada; International Journal of Greenhouse Gas Control, v. 74, p. 99–118.

McPherron, R.L., 2005. Magnetic pulsations: their sources and relation to solar wind and geomagnetic activity; Surveys in Geophysics, v. 26, p. 545–592.

Mann, I.R., Milling, D.K., Rae, I.J., Ozeke, L.G., Kale, A., Kale, Z.C., Murphy, K.R., Parent, A., Usanova, M., Pahud, D.M. and Lee, E.A., 2008. The upgraded CARISMA magnetometer array in the THEMIS era; Space Science Reviews, v. 141, p. 413–451.

Mareschal, M., 1986. Modelling of natural sources of magnetospheric origin in the interpretation of regional induction studies: a review; Surveys in Geophysics, v. 8, p. 261–300.

Nakamura, M., Yoneda, A., Oda, M. and Tsubouchi, K., 2015. Statistical analysis of extreme auroral electrojet indices; Earth, Planets and Space, v. 67, p. 1-8.

Nicolas, M.P.B. and Armstrong, D.K. 2017. Update on Paleozoic stratigraphic correlations in the Hudson Bay Lowland, northeastern Manitoba and northern Ontario; *in* Report of Activities 2017, Manitoba Growth, Enterprise and Trade, Manitoba Geological Survey, p. 133–147.

Palmroth, M., Grandin, M., Sarris, T., Doornbos, E., Tourgaidis, S., Aikio, A., Buchert, S., Clilverd, M.A., Dandouras, I., Heelis, R. and Hoffmann, A., 2021. Lower-thermosphere–ionosphere (LTI) quantities: current status of measuring techniques and models. Annales Geophysicae, v. 39, p. 189-237.

Park, J. and Chave, A.D., 1984. On the estimation of magnetotelluric response functions using the singular value decomposition; Geophysical Journal International, v. 77, p. 683-709.

Parkinson, W.D., 1983. Introduction to Geomagnetism; Elsevier, 433 p.

Peterson, R.A. and Krantz, W.B., 2003. A mechanism for differential frost heave and its implications for patterned-ground formation; Journal of Glaciology, v. 49, p. 69-80.

Phoenix Geophysics, 2004. V5 System 2000 MTU/MTU – a user guide, ver. 1.4; Phoenix Geophysics Ltd., Toronto, Canada.

Phoenix Geophysics, 2005. Data processing user guide, ver. 3.0; Phoenix Geophysics Ltd., Toronto, Canada.

Ritter, P. and Lühr, H., 2008. Near-Earth magnetic signature of magnetospheric substorms and an improved substorm current model. Annales Geophysicae, v. 26, p. 2781-2793.

Simpson, F. and Bahr, K., 2005. Practical Magnetotellurics. Cambridge University Press, Cambridge, United Kingdom, 254 p.

Sims, W.E., Bostick, F.X. and Smith, H.W., 1971. The estimation of magnetotelluric impedance tensor elements from measured data; Geophysics, 36, p. 938-942.

Stodt, J. A., 1983, Noise analysis for conventional and remote reference magnetotellurics; Ph.D. dissertation, Univ. of Utah.

Stodt, J.A., 1986. Weighted averaging and coherence sorting for least squares magnetotelluric estimates; Paper presented at Eighth Workshop on Electromagnetic Induction in the Earth and Moon, Neuchatêl, Switzerland, Aug. 24-31, 1986.

Sutarno, D., 2005. Phase-smoothed robust estimation of magnetotelluric impedance functions based on a bounded-influence regression M-estimator; Geofisika, v. 6, p. 10-16.

Sutarno, D., 2006. Robust estimation of magnetotelluric impedance functions based on a bounded-influence regression M-estimator and the Hilbert transform; *in* Geophysical Research Abstracts, v. 8, p. 01612.

Szarka, L., 1988. Geophysical aspects of man-made electromagnetic noise in the Earth – a review; Surveys in Geophysics, v. 9, p. 237-218.

Thompson, D.J. and Chave, A.D., 1991. Jackknifed error estimates for spectra, coherences, and transfer functions; *in* Advances in Spectrum Analysis and Array Processing, v. 1, (Ed.) Haykin, S., Prentice Hall, p. 58-113.

Tournerie, B. and Coulson, S., 2010. Geophysical Survey Report: BIPOLE III DC electrodes, Resistivity Survey Keewatinoow Candidate Electrode Sites on Behalf of Manitoba Hydro (Manitoba, Canada); Quantec Geoscience Ltd., Toronto, Ontario, Canada. 245 p.

Vozoff, K., 1991. The magnetotelluric method; *in* Electromagnetic methods in applied geophysics, (ed.) Nabighian, M. N., Society of Exploration Geophysicists, p. 641 – 711.

Weckmann, U., Magunia, A. and Ritter, O., 2005. Effective noise separation for magnetotelluric single site data processing using a frequency domain selection scheme; Geophysical Journal International, v. 161, p 635-652.

Weidelt, P., Chave, A.D., 2012. The magnetotelluric response function; *in* The Magnetotelluric Method: Theory and Practice, (Eds.), Chave, A.D., Jones, A.G., Cambridge University Press, New York, p. 122-162.

Wight, D.E., 1988. SEG standard for MT and EMAP data; *in* SEG Technical Program Expanded Abstracts 1988, Society of Exploration Geophysicists, p. 249-251.

Appendix 1. SEG EDI files

This document is accompanied by electronic file of_8964_Appendix_1_edi_files.zip containing the final processed MT responses (as described in Section 7) in SEG EDI format (Wight, 1988). The spectral version of the EDI format is used.

For site ksk01 the MT part of the response was processed using remote-E processing and the AMT part of the response using local-E processing. For site ksk08 the response was processed using local-B processing. The files for remote-E processed output edi files and for the mixed ksk01 response were named **ksk*nn*e.edi** and the files for the local processed file **ksk*nn*l.edi** where ***nn*** refers to the site number.